4 3 5

VTT PUBLICATIONS

Mauri Aikio

Hyperspectral prism-grating-prism imaging spectrograph

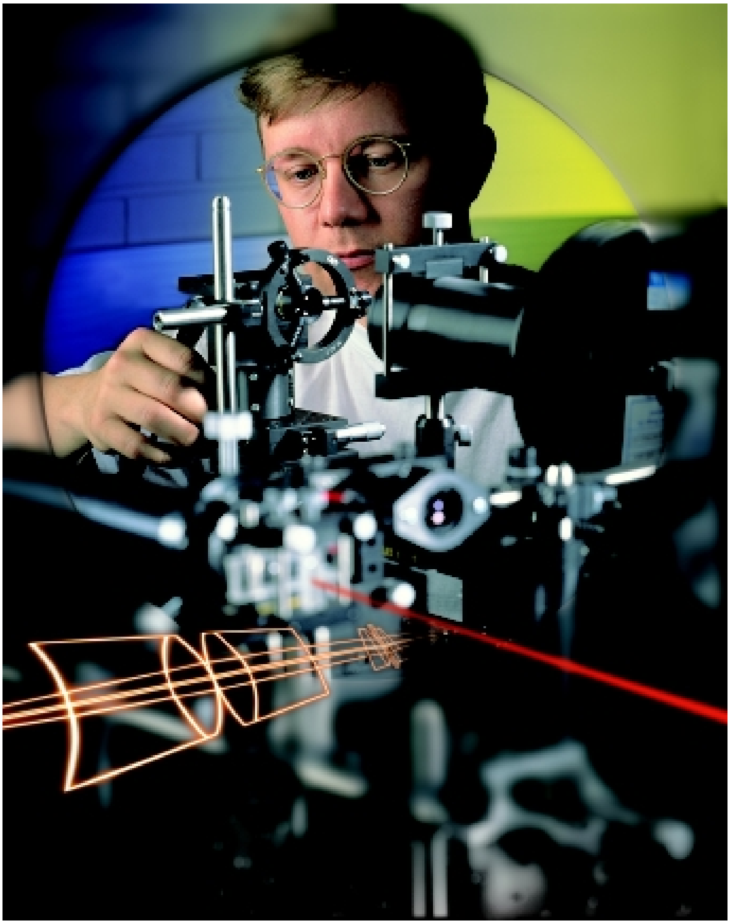

TECHNICAL RESEARCH CENTRE OF FINLAND ESPOO 2001

VTT PUBLICATIONS 435

Hyperspectral prism-grating-prism imaging spectrograph

Mauri Aikio

VTT ELECTRONICS

Dissertation for the degree of Doctor of Technology to be presented, with the permission of the Department of Electrical Engineering of the University of Oulu, for public discussion in Auditorium YB 210, Linnanmaa, on June 16th, 2001, at 12 noon.

TECHNICAL RESEARCH CENTRE OF FINLAND
ESPOO 2001

ISBN 951–38–5850–2 (soft back ed.)
ISSN 1235–0621 (soft back ed.)

ISBN 951–38–5851–0 (URL: http://www.inf.vtt.fi/pdf/)
ISSN 1455–0849 (URL: http://www.inf.vtt.fi/pdf/)

JULKAISIJA – UTGIVARE – PUBLISHER

Valtion teknillinen tutkimuskeskus (VTT), Vuorimiehentie 5, PL 2000, 02044 VTT
puh. vaihde (09) 4561, faksi (09) 456 4374

Statens tekniska forskningscentral (VTT), Bergsmansvägen 5, PB 2000, 02044 VTT
tel. växel (09) 4561, fax (09) 456 4374

Technical Research Centre of Finland (VTT), Vuorimiehentie 5, P.O.Box 2000, FIN–02044 VTT, Finland
phone internat. + 358 9 4561, fax + 358 9 456 4374

VTT Elektroniikka, Optoelektroniikka, Kaitoväylä 1, PL 1100, 90571 OULU
puh. vaihde (08) 551 2111, faksi (08) 551 2320

VTT Elektronik, Optoelektronik, Kaitoväylä 1, PB 1100, 90571 ULEÅBORG
tel. växel (08) 551 2111, fax (08) 551 2320

VTT Electronics, Optoelectronics, Kaitoväylä 1, P.O.Box 1100, FIN–90571 OULU, Finland
phone internat. + 358 8 551 2111, fax + 358 8 551 2320

Technical editing Leena Ukskoski

Otamedia Oy, Espoo 2001

Dedicated to my wife Anita, son Anssi and daughter Anniina

Aikio, Mauri. Hyperspectral prism-grating-prism imaging spectrograph. Espoo 2001, Technical Research Centre of Finland, VTT Publications 435. 114 p.+ app. 7 p.

Keywords imaging spectroscopy, prism-grating-prism components, PGP, optical design, fiber optics, hyperspectral, airborne

Abstract

A new type of a direct vision dispersing component, the prism-grating-prism (PGP), was invented by the author in 1991. This patented component allows small, low-cost hyperspectral imaging spectrographs suitable for industrial and research applications in the wavelength range from 320 nm to 2700 nm, limited by the transmission of the grating material.

The PGP spectrograph optics and the design procedure are described. The concept has been applied to many hyperspectral imaging spectrographs. The potential of the PGP construction is shown by introducing four designs in detail. 1) The prototype of a low-cost airborne hyperspectral imaging spectrograph, AISA, was the first application of the PGP concept. 2) A microscope imaging UV-VIS-NIR spectrometer system for spectral measurement of micrometer-sized objects such as wood fibers was developed. 3) A multiple-points PGP spectrograph connected to optical fibre probes was designed for industrial applications such as on-line colour and oil film thickness measurements. 4) The PGP spectrograph design for a high-speed interrogation system for large-scale fibre optic Bragg grating arrays is described.

The PGP concept and the results of the developement work were so promising, that a company was founded in 1995 to commercialize, further develope and manufacture PGP spectrograph technology. Today PGP spectrographs are used world-wide for industrial machine vision and spectral analysis, airborne remote sensing and scientific applications in the form of standard products and customized OEM components.

Preface

This thesis is based on the author's research and development work on imaging spectroscopy carried out at VTT Electronics during the period from 1991 to 1995 and again in 1999. The work was undertaken jointly in several projects with the following organizations: STFI the Swedish Pulp and Paper Research Institute, Sweden; NASA Goddard Space Flight Center, USA; University of Maryland, Department of Mechanical Engineering, USA; Tsinghua University, Department of Precision Instruments, China; Spectra-Physics VisionTech Oy; Wallac Oy; Karelsilva Oy; Kajaani Electronics Oy; and Specim Spectral Imaging Oy.

I would like to thank Prof. Rauno Anttila of University of Oulu for his guidance during my studies, Prof. Risto Myllylä of University of Oulu, who has supervised this thesis and improved it with his comments, and Prof. Harri Kopola for his encouragement and very positive attitude. I also wish to thank Dr. Jouni Tornberg and Mr. Jussi Tenhunen, who made it possible to write this thesis by standing in for me in my projects at VTT.

I wish to express my gratitude to my co-workers at VTT Electronics and at other research institutes and companies who participated in the spectrograph development projects. Particular thanks are expressed to Mr. Ahti Haapalainen for designing the mechanics of the developed instruments. I also thank Mr. Janne Aikio, Mr. Kimmo Keränen, Mr. Pekka Suopajärvi and Mr. Veli Heikkinen for helpful co-operation. Ms. Tuija Soininen is acknowledged for finalizing the drawings.

Technology Development Centre of Finland (TEKES), VTT, and the above mentioned companies are acknowledged for the support they have given to the projects this dissertation is based on. VTT, Emil Aaltosen Säätiö and Academy of Finland provided the financial support that enabled me to finish this thesis.

Oulu, May 2001

Mauri Aikio

Contents

Appendix

List of symbols and abbreviations

1D	one-dimensional
2D	two-dimensional
3D	three-dimensional
β_1	vertex angle of Prism 1 in PGP
β_2	vertex angle of Prism 2 in PGP
ε	strain = a material fractional increase in physical length when stressed = $\Delta l/l$
θ_{1B}	angle of incidence on the grating for the Bragg wavelength, λ_B, in the prism material
θ_{1C}	angle of incidence on the grating for the central wavelength,λ_C, in the prism material
θ_{2B}	diffraction angle from the grating for the Bragg wavelength, λ_B, in the prism material
θ_{2C}	diffraction angle from the grating for the central wavelength,λ_C, in the prism material
θ_B	Bragg angle in the air
θ_{out}	output angle from the PGP
$\theta(\lambda_x)_{out}$	output angle from the PGP for the wavelength λ_x
λ	wavelength
λ_B	Bragg wavelength
λ_C	central wavelength of the spectrum
λ_{cp}	the cut position, i.e. the wavelength at which the internal spectral transmittance is $\tau_i = 0.50$
λ_L	longest wavelength of the spectrum
λ_{laser}	laser wavelength

λ_{pb}	the limit of the passband, above which the internal transmittance will not fall below τ_{ipb}
λ_S	shortest wavelength of the spectrum
λ_{sb}	the limit of the stopband: the wavelength below which the internal spectral transmittance, τ_{isb}, is not exeeded
$\delta\lambda$	change in Bragg wavelength
Δ	length of the spectrum expressed in nm, λ_L–λ_S
$\Delta\lambda$	spectral bandpass or resolution
$\Delta\Phi_g$	accuracy of the angular alignment for a grating
$\Delta\Phi_p$	accuracy of the angular alignment for a prism
Δl	material increase in length
Δx	the centring accuracy of a laser spot on an alignment line
Δy	spatial resolution
τ_i	internal spectral transmittance
τ_{ipb}	the minimum value for internal spectral transmittance in the passband region
τ_{isb}	the maximum value for internal spectral transmittance in the stopband region
ν	frequency of the grating
a	assembly coefficient for the detector, which means the ratio of the required length of the spectrum and H_λ
A_0–A_5	coefficients of the optical glass for refractive index calculation
A-D	analog-digital
AIS	Airborne Imaging Spectrometer of the Jet Propulsion Laboratory
AISA	airborne hyperspectral imaging spectrograph of Specim Ltd
Ar	antireflection (coating)
AVIRIS	Airborne Visible/Infrared Imaging Spectrometer of the Jet Propulsion Laboratory

B/W	black and white
BK7	glass material of Schott
CCD	Charge Coupled Device
CHRIS	spaceborne imaging spectrometer for ESA’s PROBA satellite
CMOS	Complementary Metal Oxide Semiconductor
COIS	Coastal Ocean Imaging Spectrometer
CTIS	Computed Tomography Imaging Spectrometer
D	diameter of the aperture stop
d	grating spacing
DCG	dichromated gelatin
DE	diffraction efficiency of a grating
EOS	Earth Observing Satellite of NASA
ESA	European Space Agency
f	focal length
FBG	Fibre Bragg Grating
FK5	glass material of Schott
FOV	Field of View
FTIS	Fourier transform imaging spectrometer
FWHM	full width half maximum
GPS	global positioning system
H_{λ}	height of the detector in the spectral direction
H_{X}	height of the detector in the spatial direction
HOE	holographic optical element
IFOV	Instantaneous Field of View
IR	infrared
JPL	Jet Propulsion Laboratory, California Institute of Technology, Pasadena, USA

KOSI	Kaiser Optical Systems Inc, USA
l	length
LSPIM	Land Surface Processes and Interactions Mission Satellite of ESA
LVF	linear-variable filter
m_B	integer that represents the Bragg diffraction order
MTF	Modulation Transfer Function
MWIR	mid wavelength infrared, 3–5 µm
n	refractive index of material
n_B	refractive index of the material for the Bragg wavelength λ_B
n_C	refractive index of the material for the central wavelength λ_C
n_{laser}	refractive index of the material for the laser wavelength
n_x	refractive index of the material for the current wavelength λ_x
N_{min}	minimum number of pixels in a detector
NA	numerical aperture
NEMO	Naval EarthMap Observer Satellite of NASA
NIR	near infrared wavelength range, 700–1000 nm
O.D	optical density
OEM	original equipment manufacturer
OFS-12	the 12th Optical Fiber Sensors Conference
OFS-14	the 14th Optical Fiber Sensors Conference
OMI	Ozone Monitoring Instrument of NASA
P_1	thickness of the first half of a PGP
P_2	thickness of the second half of a PGP
PC	personal computer
PGP	direct vision dispersing prism-grating-prism component invented by the author in 1991
PRISM	multispectral imager for LSPIM of ESA

R_λ	optical resolution along the spectral axis
R_x	optical resolution along the spatial axis
RGB	red-green-blue
SNR	signal to noise ratio
SWIR	short wavelength infrared, 1.0–3.0 µm
T	transmission
TNO-TPD	Research Organization in the Netherlands
UV	ultraviolet
WD	working distance
VIS	visible wavelength range, 400–700 nm
VNIR	visible and near infrared wavelength range, 0.40–1.0 µm
VTT	Technical Research Center of Finland
z	distance between a PGP and a screen in the alignment set-up for a PGP

1 Introduction

1.1 Motivation and background

The history of imaging specrometry begins with the Airborne Imaging Spectrometer (AIS) developed in the early 1980's by the Jet Propulsion Laboratory (JPL), California Institute of Technology, Pasadena, USA. The instrument used a 32 x 32 element detector array. In 1983 JPL then proposed to develope a hyperspectral imaging spectrometer called the Airborne Visible/Infrared Imaging Spectrometer, AVIRIS, which is the best-known imaging spectrometer. Its first flight, measuring a spectrum from 400 nm to 2500 nm at 10 nm intervals, was in 1987. AVIRIS has been the primary provider of calibrated imaging spectrometer data for the research community (Goetz 1995).

These large, complicated and expensive airborne research instruments increased our knowledge and understanding of the possibilities offered by imaging spectroscopy. Other applications of hyperspectral imaging spectroscopy, such as industrial inspection, process/quality control and medical inspection uses, started to be studied. A need arose for a simple, small and inexpensive imaging spectrometer suitable for industrial and research use. On the other hand the development of the detector technology in the early 1990's improved both the sensitivity and the available number of pixels in detector arrays while still leaving them relatively economical. Computer technology has also improved the processing capacity needed for the drastically increasing amount of data that can be generated by imaging spectrometers utilizing the new, larger detector arrays. The time was right for developing a small hyperspectral imaging spectrometer.

1.2 Contribution of the thesis

In 1991 VTT Electronics designed its own hyperspectral imaging spectrograph based on the direct vision dispersing prism-grating-prism (PGP) component invented by the author (Aikio 1992, 1997a–e, 2000). The design allows a small, low-cost spectrometer to be constructed that is suitable for industrial and research use in the wavelength range from 320 nm to 2700 nm, limited by the transmission of the grating material. The advantages of the patented PGP component and the form of the PGP spectrograph are that

- The PGP provides large, linear dispersion due to its diffraction grating, as compared with a direct vision prism with small, non-linear dispersion.
- The PGP can be modified for different wavelength ranges quite freely by changing the vertex angles of the two prisms, the materials of the prisms and the grating period, contrary to the very limited grism construction.
- The grating is a volume phase transmission holographic optical element, which is used for high diffraction efficiency (up to 70%) and has polarization-independent throughput.
- The direct vision property permits a unique tubular optomechanical construction for the spectrograph, which makes it stable and small: D30mm x L 110mm with f/2.8 for a 2/3" detector (Hyvärinen et al. 1998).
- The same tubular optomechanical construction can be used in spectrographs with different kinds of PGP components designed for different wavelength ranges.

The PGP concept has been applied to many hyperspectral imaging spectrographs. The potential of this construction will be illustrated here by introducing the following four designs in detail. The research and development work was carried out during the period from 1991 to 1995 and again in 1999. The first application of the PGP concept was a prototype for a low-cost airborne hyperspectral imaging spectrograph, AISA, which was introduced after test flight experiments in 1993 by Braam et al. (1993a; 1993b), and is nowadays a commercially available instrument. Secondly, a microscope imaging UV-VIS-NIR spectrometer system for pulp quality inspection is described (Johansson and Pettersson 1997). Thirdly, a multiple points PGP spectrograph connected to optical fibre probes was designed for industrial applications such as on-line colour and oil film thickness measurements (Herrala et al. 1994, Vaarala et al.

1997). Finally, the latest PGP spectrograph design for a high-speed interrogation system for large-scale fibre optic Bragg grating arrays is described (Aikio et al. 1997, Aikio et al. 2000, Christiansen et al. 2000).

The author's contributions to these spectrograph systems were the invention of the PGP component, the design of the PGP components and the optics, the layout of the mechanical design and the assembly and alignment work for the opto-mechanical system, including test measurements but not the application measurements presented here.

The PGP concept and the results of the developement work were so promising that a company named Specim, Spectral Imaging Ltd, was founded in 1995 to commercialize and manufacture PGP spectrograph technology under licence from VTT Electronics. Specim’s products include many versions of a small, low-cost imaging spectrograph, ImSpector™, and the smallest commercial airborne imaging spectrometer system, AISA.

Nowadays PGP spectrographs are used world-wide for industrial machine vision and spectral analysis, airborne remote sensing and scientific applications in the form of standard products and customized OEM components.

1.3 Structure of the thesis

The basic concept of hyperspectral imaging spectroscopy is described in Chapter 2, "Principle and status of hyperspectral imaging spectrographs". The principle of the optics is introduced and the current status of research and development work related to imaging spectrographs (not generalizable to all imaging spectrometers) is reported briefly.

Chapter 3, "Direct vision, dispersing prism-grating-prism component for an imaging spectrograph", introduces the PGP component and the spectrograph optics based on it. The design of the component is described in detail following the author’s actual design process.

Chapter 4, "Imaging PGP spectrographs designed for imaging spectroscopy", shows two hyperspectral imaging spectrographs: the prototype of the AISA

Airborne Imaging Spectrometer and a unique microscope imaging UV-VIS-NIR spectrometer system for pulp quality inspection. A commercially available PGP spectrograph is also compared with two other low-cost spectrographs quoted from Fisher et al. (1998).

Chapter 5, "Imaging PGP spectrographs designed for fibre optic applications", presents designs of an intelligent PGP spectrometer for use in multiple points fibre optic remote spectroscopy and a PGP spectrograph for fibre optic Bragg grating sensor network interrogation.

2 Principle and status of hyperspectral imaging spectrographs

2.1 Hyperspectral imaging spectroscopy

2.1.1 Spectroscopy

Spectroscopy is used in the laboratory to investigate material properties via the interaction of electromagnetic radiation with matter. It has been used to investigate atomic structure, utilizing the spectral lines in emission and absorption exhibited by various elements, and chemical analyses of innumerable compounds and solutions by infrared spectroscopy. The use of colorimetry for the investigation of cholesterol or blood sugar, for example, in medical laboratories is a form of spectroscopy. It has also been used for checking automobile emissions, determining blood alcohol levels, and monitoring smokestack pollution, for example (Wolfe, 1997).

2.1.2 Hyperspectral system

Every imaging system has its own spectral bandwidth, defined by either a filter, detector or both. According to Willoughby et al. (1996), if only a single waveband is used, the system is referred to as panchromatic. Multispectral imagers make use of multiple filters (typically 3–12) as is the case in a 3-colour RGB camera. Systems with a relative spectral resolution (an absolute spectral resolution/a length of the spectrum) order of 0.1 are sometimes called as ultraspectral. Hyperspectral systems are characterized by having tens or hundreds of spectral bands and a relative spectral resolution order of 0.01 (Willoughby et al. 1996, Wolfe 1997). This classification of imaging systems is widely used, as can be seen from the proceedings of the latest Conference on Imaging Spectrometry VI, 31th July – 2nd August, 2000 (Descour and Shen, 2000). Also, every image is a spectral image, in that it is formed by radiation in a limited part of the entire electromagnetic spectrum. In colorimetry three categories are used to classify images: gray scale, trichromatic (for example

RGB), and multispectral. An image generated by an imaging spectrometer is a 3D data set, which is discussed in the following section.

2.1.3 Imaging spectroscopy and definition of Data Cube

The concept of imaging spectroscopy is shown in Figure 1 with a spectrum measured for each spatial element in an image (Green et al. 1998). According to Willoughby el al. (1996) hyperspectral imaging spectrometers generate a two-dimensional spatial image as well as a third spectral dimension using a two-dimensional detector array. This 3D data set is called the data, image- or object cube, which is defined by spatial **x** and **y** and wavelength λ coordinates, see Figure 2.

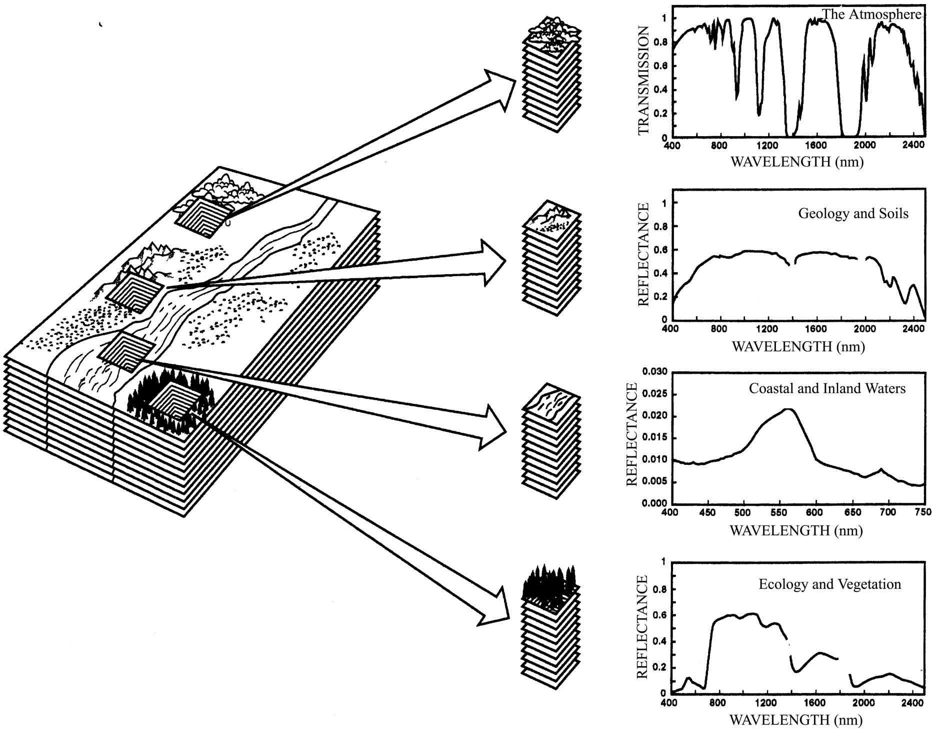

Figure 1. The concept of imaging spectroscopy is shown with a spectrum measured for each spatial element in an image. The spectra can be analyzed for the purposes of science research or for applications to a range of disciplines (Green et al. 1998).

Most system designs either image the two spatial dimensions and temporally sample the spectral dimension or image one spatial dimension and the spectral dimension while temporally sampling the second spatial dimension. An example of the first type is a filtered camera or any of the Fourier transform imaging spectrometers (FTIS), such as those presented by Otten et al. (1995), Carter et al. (1995) and Villemaire et al. (1998). The output of one image of a filtered camera or FTIS, as shown in Figure 2, is a plate **b**, whose thickness, Δλ, is determined by the spectral bandpass of the filtered camera. In a FTIS the plate corresponds to an optical path difference in the interferometer (Descour & Dereniak 1995a). Scanning the spectral dimension means that the plate moves along the λ axis. Instruments of this kind have the fundamental drawback that the spectra for a given pixel are not taken simultaneously. This can result in pixel-to-pixel spectral mixing if the scene is moving while the spectra are being scanned (Willoughby et al. 1996).

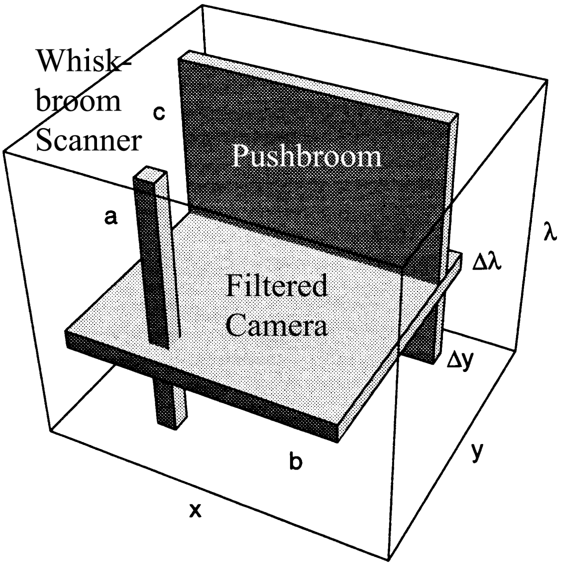

Figure 2. The data cube and data-acquisition modes characteristic of many conventional spectrometer types (Descour & Dereniak 1995a).

The second technique, a pushbroom scanner type of imaging spectrometer, which is the topic of this thesis, will be described in detail in section 2.2 "Principle of hyperspectral imaging spectrograph". It utilizes a field-limiting entrance slit and an imaging spectrometer with a dispersive element to allow the 2D detector to sample the spectral dimension and one spatial dimension simultaneously. The second spatial dimension, **y**, is typically generated by scanning or moving the instrument's field of view relative to the scene. The instrument provides a 1D spectral image and produces information, which is described by plate **c** of finite width Δy in Figure 2 (Descour & Dereniak 1995a). The disadvantage is that relative motion in the scene during the process of generating the second spatial dimension, which can result in a distorted or warped image (Willoughby et al. 1996).

Simultaneous collection of both spatial dimensions and the spectral dimension is allowed by a Computed Tomography Imaging Spectrometer (CTIS) based on three crossed gratings and proposed by Descour and Dereniak in 1995 (Descour and Dereniak 1995a and 1995 b). CTIS can collect data on dynamic scenes at high speed. In a demonstration the data cube was reconstructed with a spatial resolution of 29 x 29 pixels and a spectral sampling interval of 10 nm between 420 nm and 710 nm (31 spectral bands). The image integration time was 16 ms, but reconstruction of the data cube took a couple of minutes (Volin et al. 1998). CTIS has been used in MWIR from 3.0 to 4.6 μm with 20 x 20 pixels spatial resolution and a third generation CTIS device operates from 300 nm to 1200 nm with 1024 x 1024 matrix camera (Volin et al. 1999, Schau et al. 2000). The latest CTIS for fluorescence microscopy is able to resolve 75 x 75 spatial pixels with 30 spectral bands between 450–750 nm (Ford et al. 2001). This technique has limitations in terms of both the need for large enough area arrays to achieve higher spatial and spectral resolution and the long time needed for processing the data cube, but it will continue to evolve.

Also a non-imaging spectrometer employing a grating and linear array of detectors that provides data on a column **a**, is shown within the data cube in Figure 2. This is called a whiskbroom scanner when used as an imaging spectrometer.

2.1.4 The origin of imaging spectroscopy

According to Goetz (1995), the vision of imaging spectrometry originated from the geological disciplines. Geologists who make maps have a direct need to identify and plot the outlines of geological units characterized by a given mineralogy, for example. In the olden days they had to walk out to the outcrops and locate and identify them. Since this was a time-consuming activity, they then started to use aerial photographs, but it soon became clear that the spatial context of the photographs did not provide the key to mapping the geological units, nor was multispectral imaging in four 100–200 nm wide spectral bands obtained with the Landsat™ satellite (Figure 3a) adequate to discriminate the minerals. Field and laboratory measurements with spectrometers covering the 0.4–2.5 μm region performed in the 1970's showed that spectral reflectance could be used to identify the mineralogy and that a spectral resolution of 20 nm or less was necessary to identify individual minerals. Work on developing the first imaging spectrometer for earth observation began at the Jet Propulsion Laboratory (JPL), Pasadena, California, USA, in 1980. A pushbroom type of Airborne Imaging Spectrometer, AIS, was built as a testbed for the first infrared area arrays with 32 x 32 HgCdTe elements (see Figure 3d). In 1983, the JPL proposed and developed their hyperspectral Airborne Visible/Infrared Imaging Spectrometer, AVIRIS, which is the best-known instrument of its kind. Its construction can be seen in Figure 4. It first measured spectral images in 1987 and was the first hyperspectral imaging spectrometer to measure the solar reflectance spectrum from 400 nm to 2500 nm. This whiskbroom type of scanner (see Figure 3c) had 224 channels at 10 nm intervals across the spectrum (Green et al. 1998).

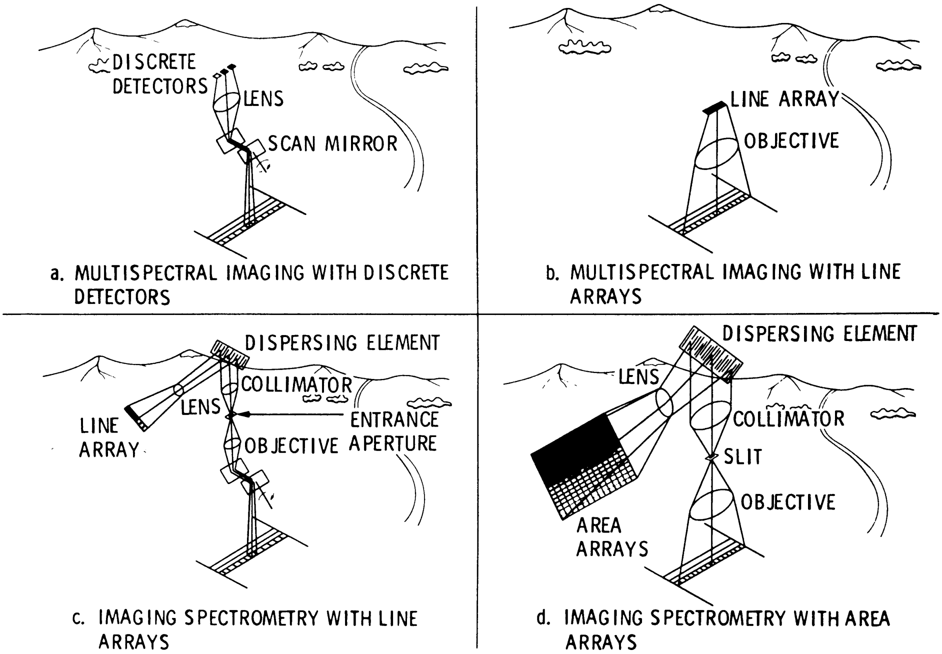

a. MULTISPECTRAL IMAGING WITH DISCRETE DETECTORS

b. MULTISPECTRAL IMAGING WITH LINE ARRAYS

c. IMAGING SPECTROMETRY WITH LINE ARRAYS

d. IMAGING SPECTROMETRY WITH AREA ARRAYS

Figure 3. Image acquisition techniques:a) Whiskbroom imaging with discrete detector elements (e.g. Landsat TM), b) Pushbroom imaging with line detector arrays, c) Whiskbroom imaging spectroscopy with line detector arrays (e.g. AVIRIS) d) Pushbroom imaging spectroscopy with area detector arrays (e.g. AIS and AISA) (Goetz 1995).

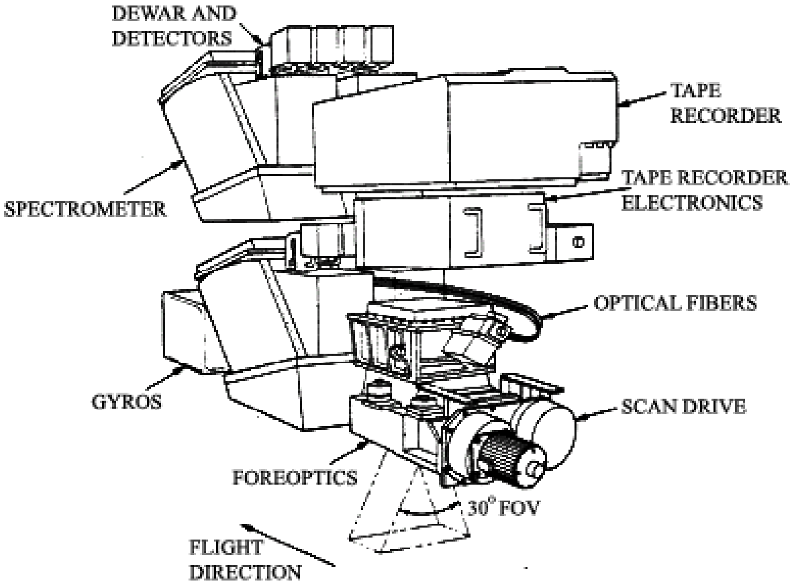

Figure 4. The AVIRIS Airborne Visible Infrared Imaging Spectrometer (Jet Propulsion Lab 2001).

Four years later, in 1991, VTT Electronics developed its own type of hyperspectral imaging spectrograph based on a patented invention, the prism-grating-prism (PGP) direct vision dispersing component (Aikio 1992). The first application of the PGP concept was the pushbroom airborne hyperspectral imaging spectrograph AISA (see Figure 3d), introduced after test flight experiments in 1993 by Braam et al. (1993a, 1993b), and which is nowadays a commercially available instrument.

A multispectral imager, with the acquisition technique shown in Figure 3b, can be constructed using a filter called a wedge or linear-variable filter (LVF). It is a rectangular interference filter with linear-variable bandpass along its vertical direction and fixed bandpass along its horizontal direction. When LVF is placed at the focal plane of a CCD camera, with LFV's vertical direction aligned to sensor's vertical direction, it becomes an imaging spectrometer. The formed image is from the same spatial area as that of a regular CCD camera (Mao et al. 1997).

2.1.5 Applications

Aerospace remote sensing has been the most important application of hyperspectral imaging spectroscopy, driven by a desire to satisfy a number of earth observation mission objectives with the same instrument. Its potential for industrial applications is enormous, given the capabilities of this type of instrument. Depending on their design, hyperspectral imagers allows great flexibility in terms of the modification of spectral and spatial parameters. The user can select only spectral bands of interest from the raw data cube, for example, or create wider spectral channels by combining individual bands. Spatial channels can be manipulated in the same manner. This is attractive for industrial applications, since a single instrument can be used for widely varying applications simply by programming the manipulation of the the data (Willoughby et al. 1996).

In 1993, Battey and Slater introduced an imaging spectrograph connected to a fibre optical probe for process control measurements based on Raman spectroscopy. This was employed for on-line monitoring of the polymerization of an acrylamide solution and for measuring the spectrum of aspirin (Battey and Slater 1993, Battey et al. 1993). Vaarala et al. (1995), Åstrand (1996) and Hagman (1996) have studied the use of imaging spectroscopy for wood quality inspection, and Borregaard (1997) for crop-weed discrimination. Willoughby et al. (1996) demonstrated the capabilities of this technique for measuring the spectra of magazine-quality newsprint.

The following PGP designs developed by VTT Electronics are described in detail in this thesis: an airborne imaging spectrometer (Braam et al. 1993a), a multiple points spectrograph using optical fibre probes for on-line industrial applications such as colour and oil film thickness measurements (Herrala et al. 1994, Vaarala et al. 1997), a microscope imaging UV-VIS-NIR spectrometer system for pulp quality inspection (Johansson and Pettersson 1997) and a high-speed interrogation system for large-scale fibre optic Bragg grating arrays (Aikio et al. 1997, Aikio et al. 2000, Christiansen et al. 2000).

2.2 Principle of hyperspectral imaging spectrograph

A spectrograph is a system for delivering multiple images of an illuminated entrance slit onto a photosensitive surface. The location of the images is a function of wavelength. It is normally characterized by an absence of moving parts (Loewen and Popov 1997, p. 439).

The basic elements of a hyperspectral imaging spectrograph are shown in Figure 5. The light source, such as a halogen lamp or the sun, illuminates the object to be measured, and the entrance optics, e.g. a camera lens or microscope objective, collects the radiation from the object and forms an image on the image plane (Image Plane 1 in Figure 5), where the entrance slit of the imaging spectrograph is located. The slit acts as a field-stop to determine the instantaneous field of view (IFOV) in spatial directions to a length of Δx and a width of Δy, marked as the measured area in Figure 5. Each point A in the spatial x-direction of the measured area has its image A' on the entrance slit. The radiation from the slit is collimated by either a lens or a mirror and then dispersed by a dispersing element, which is typically a prism or grating, so that the direction of propagation of the radiation depends on its wavelength. It is then focused on image plane 2 by the focusing optics, i.e. a lens or mirror. Every point A is represented on image plane 2 by a series of monochromatic images forming a continuous spectrum in the direction of the spectral axis, marked with different sizes of A''. The focused radiation is detected by a 2D detector array such as a CCD or CMOS detector (Hutley 1990, p. 5–58, Willoughby et al. 1996).

The imaging spectrograph allows a 2D detector array to sample one spatial dimension of length Δx and infinite width Δy and the spectral dimension of the 3D data cube simultaneously. The width Δy also defines the spectral resolution, which can be seen as Δy'' in the direction of the spectral axis in Figure 5. The second spatial dimension of the object, y, is generated by scanning or moving the FOV of the instrument relative to the scene, corresponding to the positions yN, yN+1, yN+2 in Figure 5. (Descour & Dereniak 1995a)

According to Fisher et al. (1998), grating imaging spectrographs have certain advantages over other hyperspectral technologies such as those incorporating prism, wedge filter or interferometric techniques. The primary advantage is simultaneity in the acquisition of a linearly dispersed spectrum without the need for post-processing other than correction of non-uniformities in the detector. The main limitations that traditional grating-based systems have typically encountered are correction for apertures faster than f/4 (reflection grating), multiple diffraction orders and polarization effects (reflection grating).

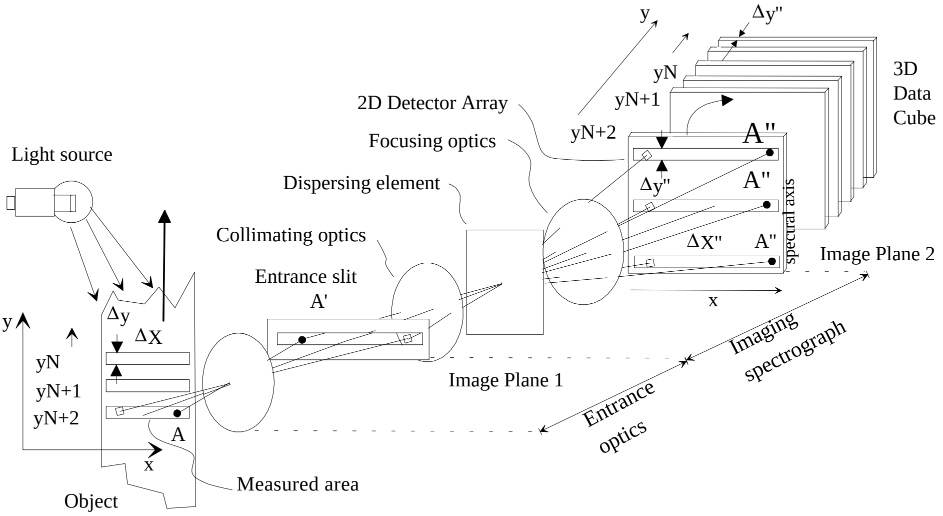

Figure 5. The basic elements of a hyperspectral imaging spectrograph, with the entrance optics and generation of the 3D data cube: spatial (x and y) and spectral dimensions.

The two main approaches adopted in grating spectrographs are reflective surface relief gratings and transmission volume holographic gratings. Traditional reflective mountings, such as the Czerny-Turner (Figure 6a) and Ebert (Figure 6b) types, have a limited flat field and large spot sizes. By varying the groove density across the grating aperture, some degree of aberration correction can be obtained with these mounts. An aberration-corrected concave grating in a Rowland mount (Figure 6c) is a second improvement, but this still falls short of the 8 to 25 µm pitch of large CCDs according to Fisher et al (1998). The Offner spectrograph with reflective convex grating (Figure 6d) offers significant improvements in image quality (Fisher et al 1998). The author used an Offner spectrograph in 1993 for the UV range in the UV-VIS-NIR microscope spectrograph system introduced in Chapter 4.2. More information on Offner spectrometers can be found in the works of Kwo et al. (1987), Mouroulis (1998), Mouroulis and Thomas (1998), Fisher et al. (1998) and Mouroulis (1999), for example, and information on the Offner unit magnification system is given by Korsch (1991).

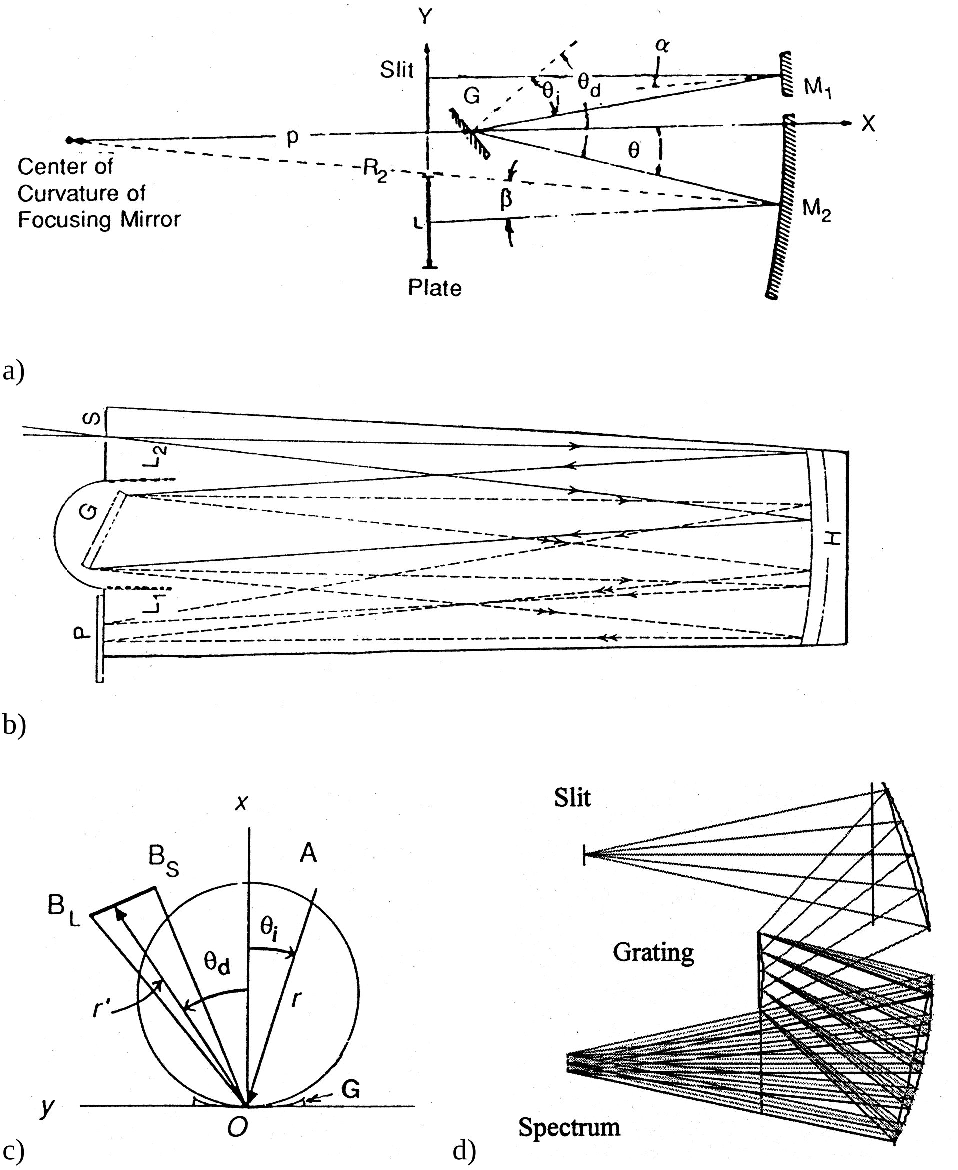

Figure 6. Mountings for a reflective grating. a) Czerny-Turner, b) Ebert, c) Rowland and d) Offner (a–c Loewen and Popov 1997 pp. 449, 450, 462; d Fisher et al. 1998)

Transmission volume holographic gratings are used in prism-grating-prism spectrographs such as that shown in Figure 7, which form the topic of this thesis. Volume grating provides very high diffraction efficiency (DE) of up to 80–90% across a narrow spectral range, but can also produce a good DE of 40–70% across a broad spectral range, depending on the design parameters. A typical DE curve for a volume holographic transmission grating is shown in Figure 8a. The DE is practically independent of polarization, unlike the situation in a reflection grating, which typically shows a polarization dependence of several tens of percent, as seen in Figure 8b. This is a benefit in reflectance measurements (Hyvärinen et al. 1998). In spectrographs of this kind the image quality is determined by the complexity of the collimating and focusing optics (Fisher et al. 1998).

The problems associated with imaging spectrographs are change of dispersion angle with field position (smile) and change of magnification with wavelength (spectral keystone), see Figure 9 (Fisher et al. 1998).

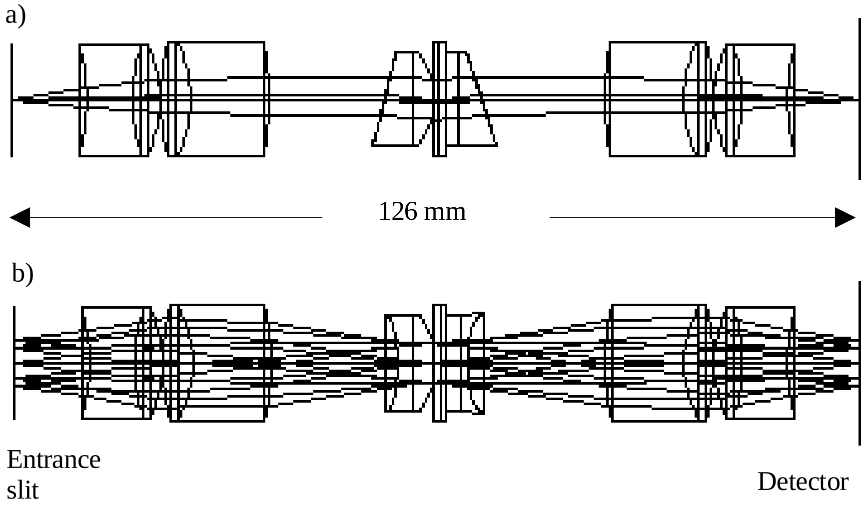

Figure 7. A compact optical construction of a PGP spectrograph seen from a) the spectral and b) the spatial direction.

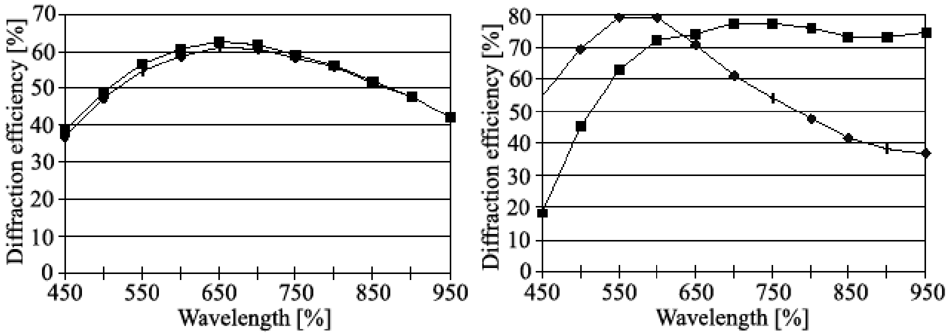

a) b)

Figure 8. Polarization dependence of the diffraction efficiency of a) a volume-phase holographic transmission grating and b) a reflection grating shown for parallel (■) and perpendicular (◆) polarization (Hyvärinen et al. 1998).

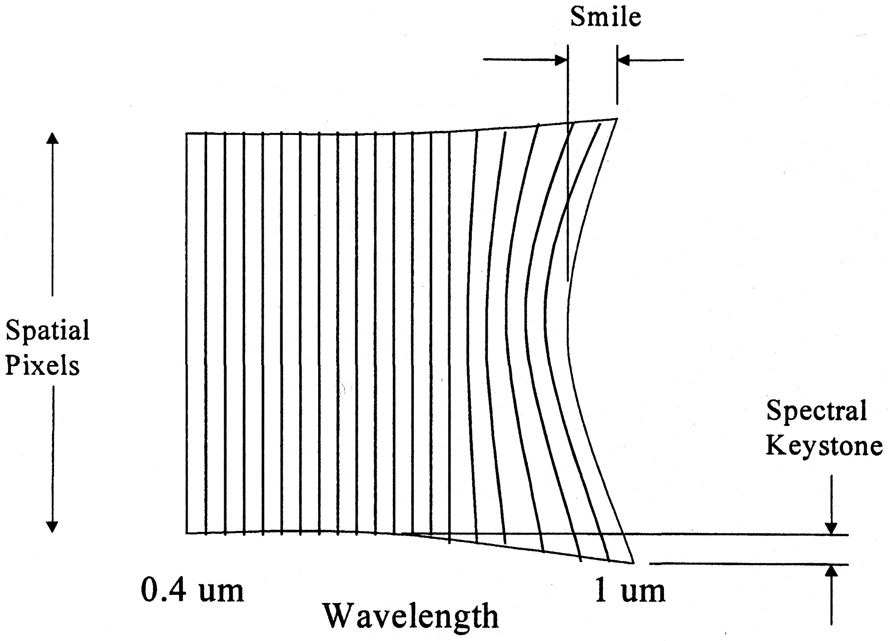

Figure 9. Definition of smile and keystone distortion (Fisher et al. 1998).

2.3 Current status of hyperspectral imaging spectrographs

The best-known airborne imaging specrometer system is AVIRIS, a world-class instrument in the realm of Earth remote sensing developed by the Jet Propulsion Laboratory (JPL) of the California Institute of Technology in Pasadena, California. AVIRIS has been in active use ever since its first flight in 1987. The AVIRIS system has been upgraded and improved in a continuous effort to meet the requirements of investigators (Green et al. 1998). It is a unique optical sensor that delivers calibrated images of the upwelling spectral radiance in 224 contiguous spectral channels with wavelengths from 400 to 2500 nm. The instrument flies aboard a NASA ER-2 aeroplane approximately 20 km above sea level at about 730 km/h. AVIRIS has flown all across the US, Canada and Europe (Jet Propulsion Lab 2001). The last special journal issue related to AVIRIS, with a long list of references, was written by Green et al. (1998). Information can also be found in the AVIRIS website http://makalu.jpl.nasa.gov/aviris.html.

The technical development of hyperspectral imaging spectrographs is much slower than that of consumer electronics such as mobile phones. VTT Electronics designed its own type of hyperspectral imaging spectrograph in 1991, based on the direct vision dispersing PGP component (Aikio 1992). The first publications regarding this airborne imaging spectrograph, called AISA, were produced in 1993 (Braam et al. 1993a; Braam et al. 1993b), and in the same year Burns at JPL and Battey at Kaiser Optical Systems Inc (KOSI) also introduced low-cost designs for imaging spectrographs based on a volume transmission grating and off-the-shelf optical components (Burns et al. 1993; Battey and Slater 1993; Battey et al. 1993). Two of these instruments, AISA from Spectral Imaging Ltd (Specim) and Holospec™ from KOSI, are commercially available nowadays as various versions suitable for many applications. Their technical data can be found at the websites http://www.kosi.com/raman/products/holospec.html and http://www.specim.fi/ (Specim 2001a; KOSI 2001). A comparison between Holospec™ and an imaging PGP spectrograph, ImSpector™, based on the same optics as AISA is presented in section 4.3 (Specim 2001b, Fisher et al. 1998).

Development of the optics for hyperspectral imaging spectrograph has recently been focused on the Offner construction, based on a convex reflection grating, as shown in Figure 6d. The lack of an appropriate technology for grating fabrication had earlier made the practical realization of these designs difficult, limiting the interest in Offner spectrometer. However, progress in electron-beam lithography techniques has now permitted fabrication of the required high-performance convex gratings (Mouroulis 1998). Mouroulis at JPL presented several Offner spectrograph designs, showing that this flexible, all-reflective form can satisfy the stringent requirements of imaging spectroscopy over a broad spectral band from UV to thermal IR, reducing the spectral and spatial distortion to a small fraction (~1%) of a pixel (Mouroulis 1998). The advantages of the Offner specrograph are that a) it operates with a relatively low f-number (≥f/2), b) it accepts a long slit while maintaining compact size, c) it has very small spectral and spatial distortion, d) it needs only three optical surfaces, and e) it utilizes only spherical and centred surfaces (Mouroulis and Thomas 1998). Mouroulis and Thomas (1998) also quoted experimental results obtained with an Offner spectrograph for wavelengths of 400–1000 nm with 3 nm spectral resolution, producing 750 spatial pixels and having a measured distortion of 2% of a pixel. Fisher et al. (1998) and Davis et al. (1999) have reported on the measured performance of a three-mirror Offner spectrograph, HyperSpec™ VS-15, from American Holographic Inc. that has a wavelength range of 400–1000 nm and measured smile and keystone distortions of < 1 pixel (12 μm).

Mouroulis (1999), comparing the Offner construction with a high-speed Dyson spectrograph (Mertz 1962, 1977), concluded that both of these simple spectrographs with only co-centric spherical surfaces can satisfy stringent spectral and spatial uniformity requirements. The choice between them must be based on the all-reflective nature of the Offner model as against the high speed of the Dyson design. Another spectrometer, also based on the Offner relay concept but using curved prisms as dispersing elements, has been proposed by Lobb and patented by SIRA Electro-Optics Ltd, UK (Lobb 1998). The design is used in the spaceborne imaging spectrometer CHRIS for ESA’s PROBA satellite launched late in 2000. The CHRIS spectrometer provides 10 nm spectral resolution over a range from 415 nm to 1050 nm (Cutter et al. 1999). The addition of prisms to the Offner model is a considerable complication as compared to a simple grating construction (Mouroulis and Thomas 1998).

In addition to the instruments mentioned above, many unique hyperspectral imagers have been reported. The TRW Imaging Spectrometer III (TRWIS III), for 380–2450 nm with 384 spectral channels divided between two spectrographs, has been in use since 1996 and is a commercially available airborne instrument (Sandor-Leahy et al. 1998). The Naval EarthMap Observer (NEMO) Satellite carries a Coastal Ocean Imaging Spectrometer (COIS) consisting of two Offner spectrographs, VNIR for 0.4–1.0 µm and SWIR for 1.0–2.5 µm, with a common entrance slit (Wilson and Davis 1999). Labandibar et al. (1999) proposed a multispectral imager, PRISM, for the Land Surface Processes and Interactions Mission (LSPIM) Satellite of the European Space Agency (ESA). This consisted of a thermal imager with two spectral bands, 8.0–8.5 µm and 8.6–9.1 µm, and a dual-channel imaging spectrograph for 0.45–2.35 µm. The spectrograph employs Offner relay optics with prisms as dispersing elements. The large wavelength range is divided between two detectors, VNIR for 0.45–1.0 µm and SWIR for 1.0–2.35 µm, by a dichroic plate just before the focal plane of the spectrograph.

One of these unique hyperspectral imagers is the Ozone Monitoring Instrument (OMI) introduced by Laan et al. (2000). This is a new imaging spectrograph system covering UV/VIS from 250 nm to 500 nm with 740 wavelength bands (NASA 2001 b). The wavelength range is divided among three spectrographs: UV-1 for 270–314 nm, UV-2 for 306–380 nm and VIS for 350–500 nm. Its optical construction is seen in Figure 10. The OMI is one of the four instruments which will be launched aboard NASA's third Earth Observing Satellite (EOS), AURA, in June 2003. The EOS AURA mission is a component of the international efforts to understand changes in the Earth's ozone layer, air quality and climate (NASA 2001). OMI is being developed by Finnish and Dutch companies in close collaboration with the climate research and meteorological community and under contracts from the Finnish Meteorological Institute and the Netherlands Agency for Aerospace Programmes (Laan et al. 2000). The contributing contractors are TNO-TPD in the Netherlands and Patria Finavitec and VTT in Finland (NASA 2001b).

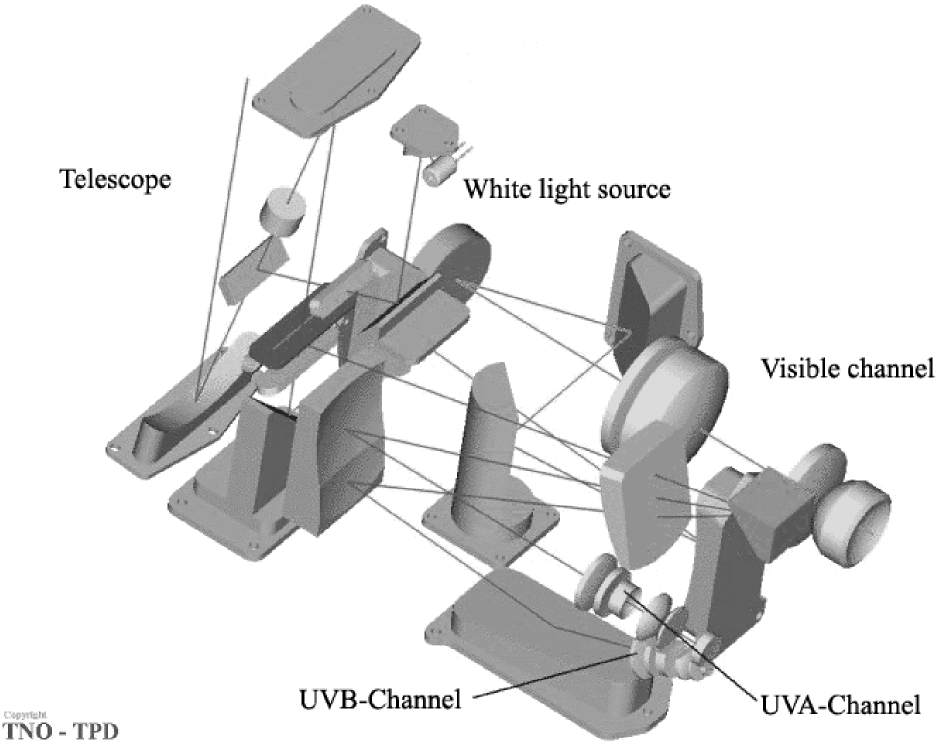

Figure 10. Optical construction of the ozone monitoring instrument, OMI, which is hyperspectral imaging spectrograph system for 250–500 nm (NASA 2001b).

3 Direct vision dispersing prism-grating-prism component for an imaging spectrograph

3.1 Principle of the prism-grating-prism component

The optical construction of the direct vision dispersing prism-grating-prism (PGP) component is illustrated in Figure 11. It is composed of a specially designed volume transmission grating cemented between two identical or almost identical prisms. Short and longpass filters are typically placed between the grating and the prisms, cutting off unwanted wavebands and changing the spectral response. When the filters are integrated in this way inside a PGP, reflections from their surfaces can be avoided. The PGP often contains the aperture stop of the spectrograph optics, which is located in contact with the grating.

The operating principle of the PGP component and the effects of its parameters on the throughput can be seen in Figure 11. A collimated light beam from the collimating optics of the imaging spectrograph is refracted by Prism 1. Its vertex angle, β_1, is calculated so that the incidence angle of the refracted beam on the grating is so called Bragg angle, θ_B, for a certain wavelength λ_B, but not necessarily for the central wavelength λ_C of the spectrum from λ_S to λ_L. The grating disperses the light in the diffraction order -1. The vertex angle, β_2, of Prism 2 and the thickness, P_2, of the second half of the PGP are optimized to refract the spectrum so that the light spots of both ends of the spectrum on the detector are at the same distance from the optical axis, i.e. the spectrum is centred.

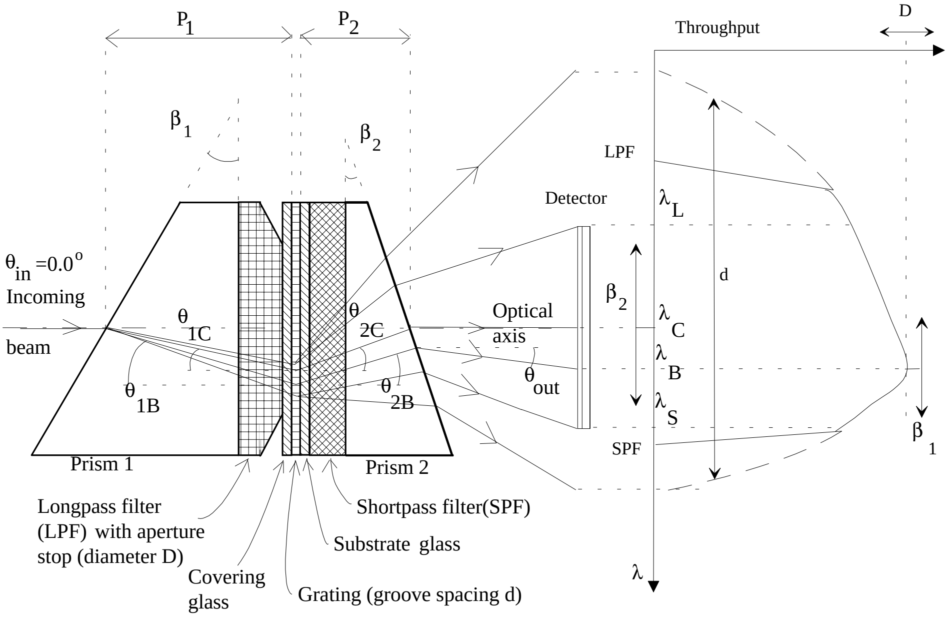

Figure 11. Principle of the PGP component, effects of its parameters on the throughput and symbols used in its design: λ_S *= shortest wavelength,* λ_C *= central wavelength,* λ_L *= longest wavelength,* P_1 *and* P_2 *= central thicknesses of the halves of the PGP;* β_1 *and* β_2 *= vertex angles of the prisms;* θ_{1B} *and* θ_{1C} *= angles of incidence on the grating for the Bragg,* λ_B*,, and central,* λ_C *, wavelengths in the prism material;* θ_{2B} *and* θ_{2C} *= output angles from the grating in the prism material;* $\theta_{out} = \theta(\lambda_x)_{out}$ *= output angle from the PGP; d = groove spacing of the grating; D = diameter of the aperture stop.*

The Bragg condition: When monochromatic light, λ_B, is incident on a volume grating at the Bragg angle, θ_B, the angle of incidence and the angle of diffraction are equal, and the diffracted power gets a maximum, see Figure 12. When the thickness of the grating is large enough, only two waves in the grating need be taken into consideration, the incoming wave and the outgoing wave. The Bragg condition is given by

Equation 1 $$m_B \cdot \lambda_B = 2 \cdot d \cdot \sin(\theta_B)\,,$$

where m_B is an integer that represents the Bragg diffraction order, which is -1 in the case of a PGP, and d is the grating spacing. The terms “Bragg wavelength” and “Bragg angle” are commonly used to describe the wavelength and angle that exactly satisfy the Bragg condition. In reality there is an envelope about the Bragg wavelength and Bragg angle in which there is significant diffracted light energy, giving rise to a spectral bandwidth and angular bandwidth for the volume phase grating (Arns et al. 1999; Hariharan 1996, p. 49; George and Matthews 1966).

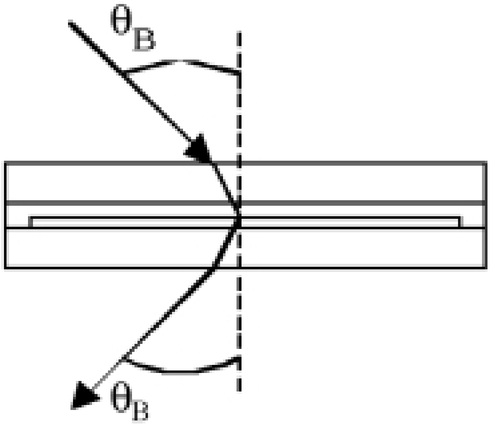

Figure 12. Light path at Bragg condition throuhg a transmission volume grating.

The PGP concept has been applied to the wavelength range from 340 nm to 1750 nm. The applicable wavelength range of the used grating material, dichromated gelatin, is from about 320 nm to about 2700 nm, as can be seen in Figure 13, where the transmittance of uniformly exposed and processed dichromated gelatin with a 15 µm depth is shown. The transmittance of the BK7 substrate and surface reflection losses has been ratioed out (Barden et al. 2000).

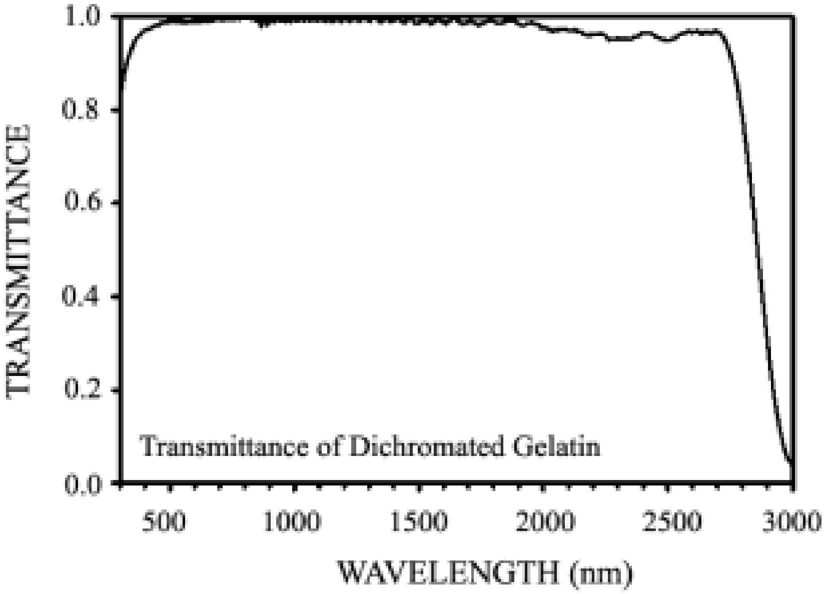

Figure 13. The transmittance of dichromated gelatin uniformly exposed and processed with a 15 μm depth. The transmittance of the BK7 substrate and surface reflection losses were ratioed out (Barden et al. 2000).

The direct vision property, a straight optical axis, is the most important advance in the PGP component. As an example the simple imaging spectrograph for research and industrial use is presented in Figure 14: the imaging PGP spectrograph optics can be easily assembled and adjusted between a standard CCD camera lens and a B/W CCD camera with C-mount. The concept can be modified for different wavelength ranges simply by changing the PGP, see Figure 15. The author has designed and implemented three versions of the above spectrograph optics in which the lenses and all the mechanics are the same and only the PGP component has different designs for VIS (400–700 nm), VIS–NIR (450–900nm) and NIR (700–1000 nm) wavelength ranges.

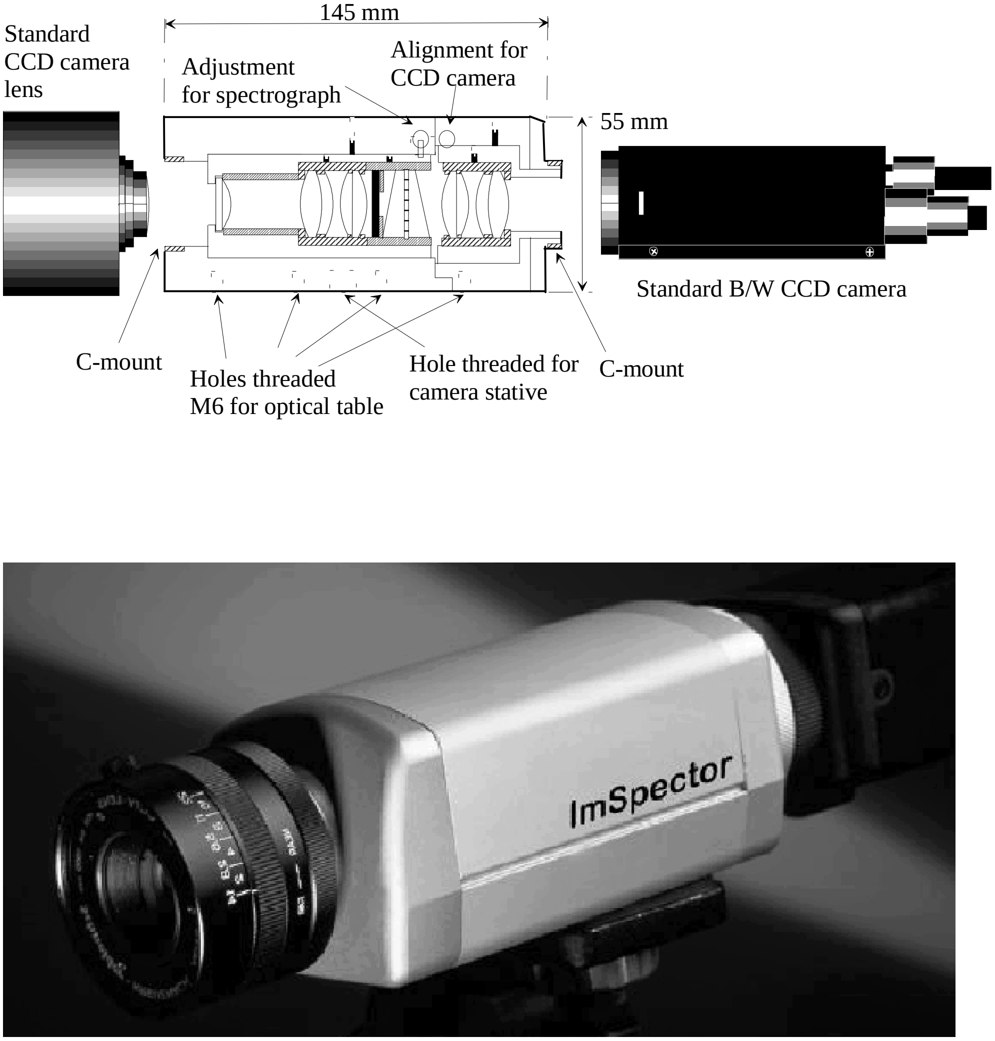

Figure 14. One version of an imaging PGP spectrograph. ***Drawing****: the spectrograph optics can be easily assembled between a standard CCD camera lens and a B/W CCD camera with C mount.* ***Photo****: A commercially available PGP spectrograph (Specim 2001b).*

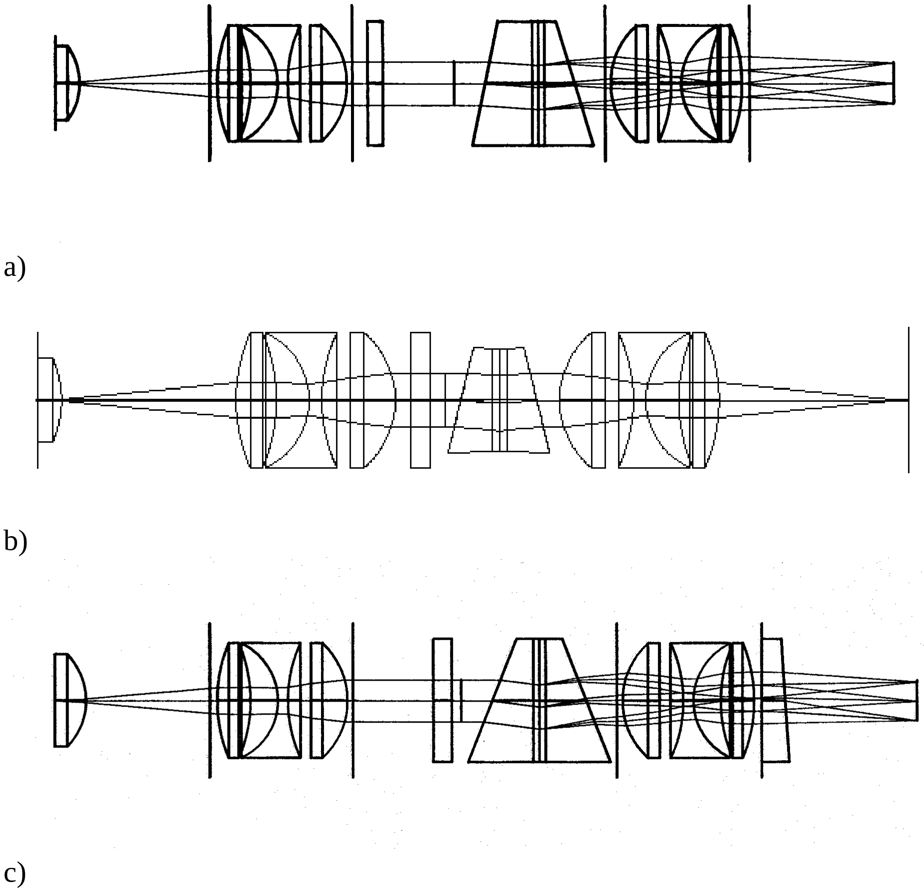

a)

b)

c)

Figure 15. Imaging PGP spectrographs implemented on the basis of the same optics and mechanics. Only the PGP has different designs for wavelength ranges of a) 400–711 nm (measured), b) 450–900 nm (measured) and c) 712–1021 nm (measured).

3.2 Procedure for designing an imaging PGP spectrograph

The purpose of this section is to look briefly at the procedure that the author used for designing the optics for the prototypes of low-cost imaging PGP spectrographs for different applications.

The first task in the design procedure is to choose the detector according to the geometry of the matrix detector, i.e. the dimensions and the number of elements. When two light spots on a discrete detector have to be resolved, four elements are needed (Schlemmer and Mächler, 1985). If the shortest wavelength in the range of the spectrograph is λ_S, the longest λ_L and the spectral resolution $\Delta\lambda$, the minimum number of pixels in the spectral direction of the detector can be calculated by $N_{min} = 4(\lambda_L - \lambda_s)/\Delta\lambda$, while the minimum number of elements in the spatial direction of the detector is four times the number of spatial channels.

As there are only limited number of sizes of detector commercially available (number of elements in the horizontal and vertical directions) and customizing is expensive, it quite often happens that there are too many elements in the detector in either the spectral or the spatial direction. In this situation neighbouring elements can be summed together. If there are unused elements between two spatial channels, for example, these can be skipped when reading the detector or storing the measured data.

The dimension of the detector in the spectral direction fixes the length of the spectrum and thus scales the size of the whole spectrograph including the width of the entrance slit. That is because the field of view of the focusing optics is limited to approximately +/-10°. The size of the element also determines the optical resolution for the spectrograph optics. The optical resolution along the spectral axis is calculated from the formula $R_\lambda = (\lambda_L - \lambda_S)/(\Delta\lambda a H_\lambda)$, where H_λ is the height of the detector in the spectral direction and a is an assembly coefficient for the detector, $a = 1-(2\cdot \text{assembly margin})/H_\lambda$, see Figure 16. Assembly margins, typically 0.1–0.2 mm, are needed because there are no transverse adjustments for the detector.

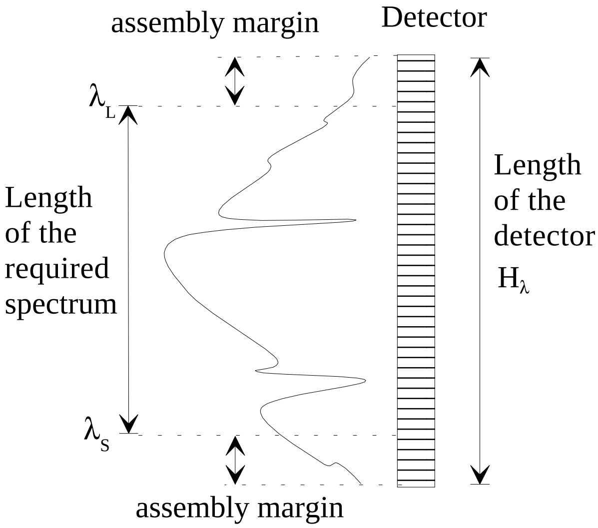

Figure 16. The assembly coefficient, a, for the detector is defined as the ratio of the length of the required spectrum and the length of the detector,H_λ.

Once the wavelength range and dimensions of the detector are known, an approximate value for the number of lines in the grating as a function of the focal length, $v(f)$, is calculated to choose the focal length. The PGP is optimized for the selected focal length. The following equation, based on a simplified model consisting of the grating, the focusing optics and the detector, can be used (derived in Appendix A).

Equation 2

$$v(f) = \left[\sqrt{\left(\frac{\lambda_L}{Q}\right)^2 - \frac{2W\lambda_L\lambda_C}{Q^2} + \left(\frac{W\lambda_C}{Q}\right)^2 + \lambda_C{}^2} \right]^{-1} ,$$

where

$$Q = \frac{aH_\lambda}{2f\sqrt{1+\frac{aH_\lambda}{2f}}} \quad \text{and} \quad W = \frac{1}{\sqrt{1+\frac{aH_\lambda}{2f}}}\ ,$$

f = the focal length of the focusing optics,
λ_L = longest wavelength of the spectrum,
λ_C = central wavelength of the spectrum,
H_λ = the height of the detector in the spectral direction,
a = an assembly coefficient for the detector = the ratio of the required length of the spectrum and H_λ.

A calculation for the field of view, FOV, of the focusing lens is needed, too.

Equation 3 $$FOV = a\tan\left(\frac{\sqrt{{H_\lambda}^2 + {H_X}^2}}{2f}\right),$$

where H_X = the height of the detector in the spatial direction.

A suitable focal length and line number will be selected taking into account considerations such as the complexity of the optics, see Figure 17, the desired size of the spectrograph, which depends on the focal length of the optics, and possible special application requirements.

The collimating and focusing optics are then designed. The aperture stop is located outside the lens systems. The resolution requirement for the lens design comes from the spectral or spatial resolution target, depending on which is more stringent. Chromatic aberration must be efficiently corrected. In many constructions the optics are identical, to save design work and reduce manufacturing and assembly costs.

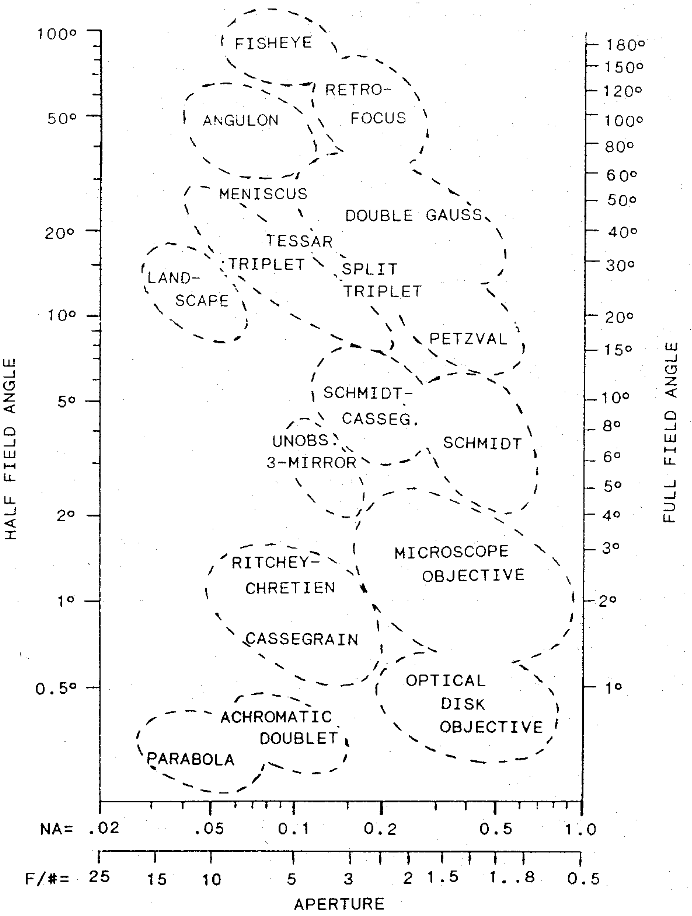

Figure 17. Map of design types commonly used for various combinations of aperture and field of view (Smith 1992).

The next phase is PGP component design, which is explained in detail in section 3.3. The PGP can easily be optimized in simple software using given equations. The wavelength range gives the information for selecting the optical longpass and shortpass filters and the prism material, while the selection of the Bragg wavelength for the grating is influenced by the spectral sensitivity of the detector and the emission spectrum of the light source.

After that, all the optical data are inserted into the optical design software to achieve the final optimization of the whole spectrograph.

3.3 Design of the PGP component

3.3.1 Diffraction grating

Since diffraction efficiency is one of the most important considerations for holographic optical elements (HOEs), these are usually fabricated in a volume phase material, as only volume phase HOEs can produce diffraction efficiencies of nearly 100% (Chang and Leonard 1979). The thickness and refractive index modulation of the grating material are two of the parameters that control the diffraction efficiency of a grating. This material is dichromated gelatin (DCG), which is an almost ideal recording material for volume phase HOEs (Hariharan 1996, p. 107). According to Chang and Leonard (1979), DCG had the highest refractive index modulation capacity of all the materials available (at that time), in that an index modulation of 0.08 with little scattering was achieved. DCG can also be reprocessed (or redeveloped) to produce the desired refractive index modulation, and the thickness of a DCG hologram can be controlled (increased or reduced) either by varying the preprocessing parameters or by using appropriate postprocessing treatments. DCG has low scattering and absorption over the range from visible to NIR wavelengths, see Figure 13, a high resolution capacity, greater than 5000 lines/mm, and a spatial frequency response that is almost uniform over a broad range of spatial frequencies, from 100 lines/mm to 5000 lines/mm.

Typical diffraction efficiencies of volume-phase holographic transmission gratings with a wide wavelength range (VIS 400–700 nm and VIS–NIR 450–950 nm) are shown in Figure 18a. These gratings are independent of polarization, as can be seen in Figure 8a, where cases of parallel and perpendicular polarization are shown (Hyvärinen et al. 1998).

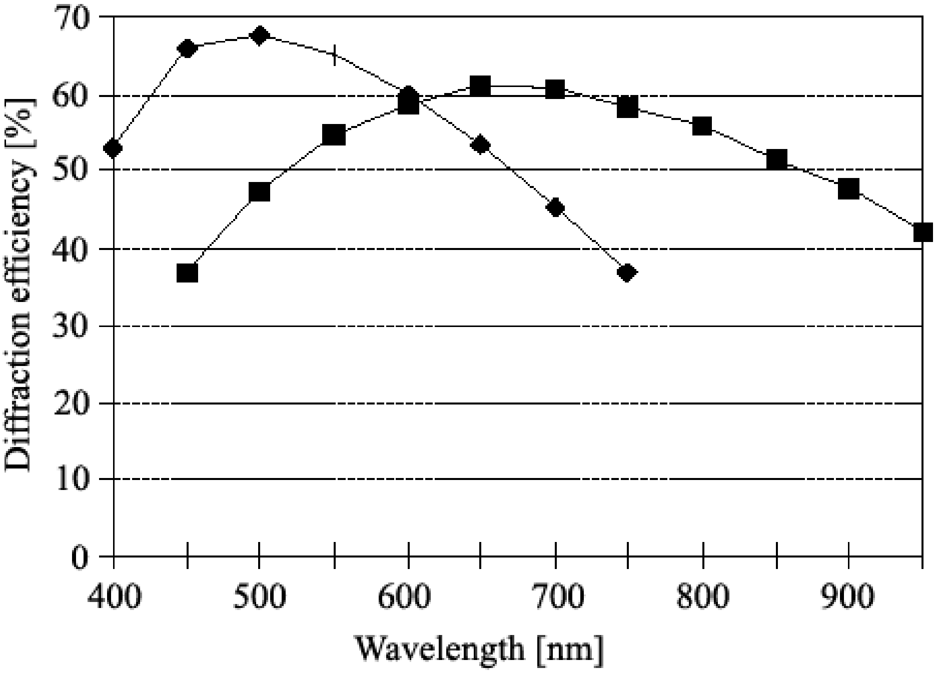

Figure 18. Typical diffraction efficiencies of VIS, 400–700 nm (◆) *and VIS–NIR,450–950 nm* (■) *volume-phase holographic transmission gratings (Hyvärinen et al. 1998).*

Environmental stability with respect to humidity and temperature is an important requirement for practical systems such as imaging spectrometers. HOEs recorded in DCG are well known to be extremely sensitive to humidity, in that high humidity causes a drastic decrease in diffraction efficiency, because the swelling of gelatin reduces the refractive index modulation. This effect can be eliminated by cementing a glass cover plate over the well-dried gelatin layer, see Figure 19. The destructive tests performed on DCG HOEs by Chang and Leonard also showed that if they are well dried and have a cover plate they will be stable up to about +110°C but will degrade rapidly thereafter (Chang and Leonard 1979). When the DCG gratings were purchased the manufacturer guaranteed that they would remain stable for one hour in boiling water.

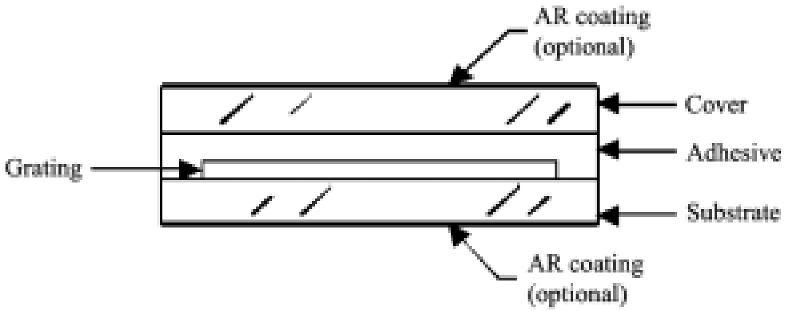

Figure 19. Humidity protection of a dichromated gelatin grating (Arns et al. 1999).

The optical properties and environmental stability of DCG and the availability of commercial sources of customized high-quality gratings led to the use of this material in the PGP components. The fact that the grating is cemented between the prisms also means that a volume type of transmission grating is needed.

3.3.2 Long and short pass filters

Short and longpass filters are typically placed between the grating and the prisms to cut off unwanted wavebands and possibly change the spectral transmission of the PGP component. When the filters are integrated in this way, i.e. inside a PGP, reflections from their surfaces can be avoided.

The longpass filter in a PGP is usually an absorbing color glass filter. The important properties to consider when selecting a filter are a) the cut position, λ_{cp}, i.e. the wavelength at which the internal spectral transmittance is $\tau_i = 0.50$; b) the limit of the stopband, λ_{sb}, i.e. the wavelength below which the internal spectral transmittance, τ_{isb}, is not exeeded; c) the limit λ_{pb} of the passband, above which the internal transmittance will not fall below τ_{ipb}. According to the "Optical Glass Filters" catalogue of Schott Glaswerke, longpass filter glasses can have a very steep transmission edge and the internal spectral transmittance is below 10^{-5} in the stopband for most glass types and above 0.99 in the passband. For example, the values for glass type OG 590 are: thickness 3mm, $\lambda_{cp}(\tau_i = 0.50) = 590$ nm, $\lambda_{sb}(\tau_{isb} = 10^{-5}) = 540$ nm, $\lambda_{cp}(\tau_{ipb} = 0.99) = 640$ nm (Schott 84, p. 19).

3.3.3 Prisms

Equations for PGP component calculation are given in this section based on a simple 2D model.

At first, a wavelength satisfying the Bragg condition, λ_B, in the grating has to be chosen, taking into account the wavelength response of the detector and the emission spectrum of the light source, for example.

The refractive index as a function of wavelength is calculated from the Schott dispersion formula:

Equation 4 $$n^2 = A_0 + A_1\lambda^2 + A_2\lambda^{-2} + A_3\lambda^{-4} + A_4\lambda^{-6} + A_5\lambda^{-8},$$

where λ is the wavelength for which the refractive index is to be calculated and A_0–A_5 are the coefficients of the optical glass, available in most manufacturers' catalogues (Zemax 2000, p. 331).

The equations from Equation 5 to Equation 11 are based on Snell's law and the grating equation. The angle of incidence θ_{1B} in the prism material at the grating was calculated from

Equation 5 $$\theta_{1B} = \arcsin\,[-(\lambda_B\, \nu)/\, 2n_B],$$

where n_B is the refractive index for λ_B and ν is the frequency of the grating.

The vertex angle of the first prism was calculated using the equation

Equation 6 $$\beta_1 = \arctan\{[(\tan\theta_{1B})^{-1} - (n_B\sin\theta_{1B})^{-1}]^{-1}\}.$$

The angle of incidence at the grating for the central wavelength λ_C had to be calculated taking into account the dispersion in the first prism. The equation was

Equation 7 $$\theta_{1C} = \theta_{1B} + [\arcsin(\sin\beta_1/\, n_B) - \arcsin(\sin\beta_1/\, n_C)],$$

where n_C is the refractive index of the prism material for λ_C.

The output angle from the grating for λ_C is then given by the equation

Equation 8 $$\theta_{2C} = \arcsin(\sin\theta_{1C} + \lambda_C v/n_C).$$

The vertex angle of the second prism was calculated

Equation 9 $$\beta_2 = \arctan\{[(\tan\theta_{2C})^{-1} - (n_C\sin\theta_{2C})^{-1}]^{-1}\},$$

and the output angle from the PGP for wavelength λ_x using

Equation 10

$$\theta(\lambda_x)_{out} = \beta_2 + \arcsin[n_x\sin\{\arcsin(-\lambda_x m/dn_x + \sin[\beta_1 + \arcsin(\sin\{-\beta_1\})])-\beta_2\}],$$

where d is the grating period, *m* is the diffraction order (-1 in the PGP) and n_x is the refractive index of the prism material for the current wavelength λ_x, calculated using Equation 4.

Two optical filters were selected for the PGP: a shortpass filter and, more importantly, a longpass filter, cutting off the unwanted short (UV) wavelengths. The mechanical dimensions of the PGP were then calculated. Since the optical thicknesses of the prisms are linked together, the second prism was calculated first, because its vertex angle β_2 is larger. The central thickness P_2 consisted of the thicknesses of the shortpass filter, the substrate of the transmission grating and the central thickness of the second prism. The central thickness of the first half of the PGP was calculated from

Equation 11 $$P_1 = P_2\tan(\theta_{2C}) / \tan(|\theta_{1B}|).$$

3.3.4 Aperture stop

The aperture stop for the whole spectrograph and for the focusing optics is located in the centre of the PGP, as close as possible to the grating, see Figure 20 and Figure 11. In this way the aperture stops for both spatial and spectral directions are located at the same distance from the optics, which enables telecentricity in the optics to be acheived for both directions.

The aperture stop inside the PGP was implemented by grinding down the edge of the filter in front of the grating to form the desired size of aperture, see Figure 11. After the PGP had been glued together, the ground surface was carefully painted black.

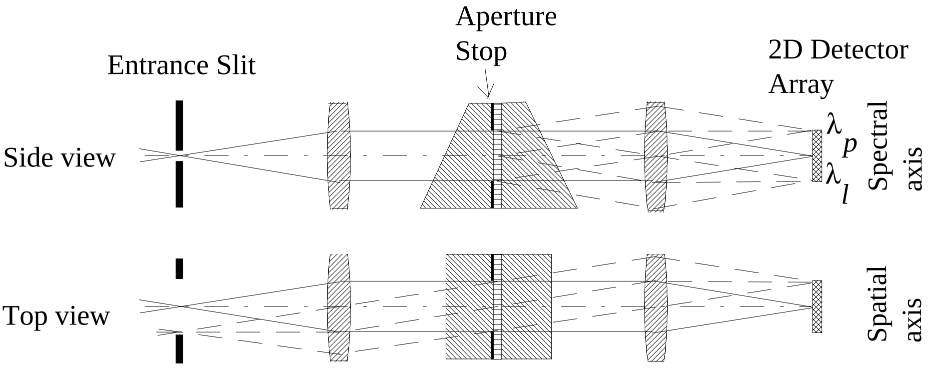

Figure 20 The aperture stop of a spectrograph is located in the centre of the PGP, as close as possible to the grating.

3.3.5 Alignment of a PGP component

The angular orientation of the three main components of a PGP, the two prisms and the grating, is critical. The phases of the alignment method are shown in Figure 21. The set-up requires a laser, a suitable holder for the components of the PGP and a screen. In the first phase (number 1 in Figure 21) the position of the laser spot without any optical component is marked on the screen and a straight alignment line is drawn through it. Then, in the phase 2, the first prism is placed in the holder and the spot is shifted downwards. The prism is turned around the optical axis to adjust the spot on the alignment line. In the third phase the grating is inserted in the holder, where it generates several diffraction orders, e.g. from +1 to -2, as in Figure 21. The grating is then turned around the optical axis so that all the existing spots lie on the alignment line. The zero order should retain its position, because this is affected only by the first prism. The grating now has the correct orientation. In the fourth phase the second prism is placed in the holder. This shifts the spots downwards. It is then adjusted so that all the spots lie on the alignment line.

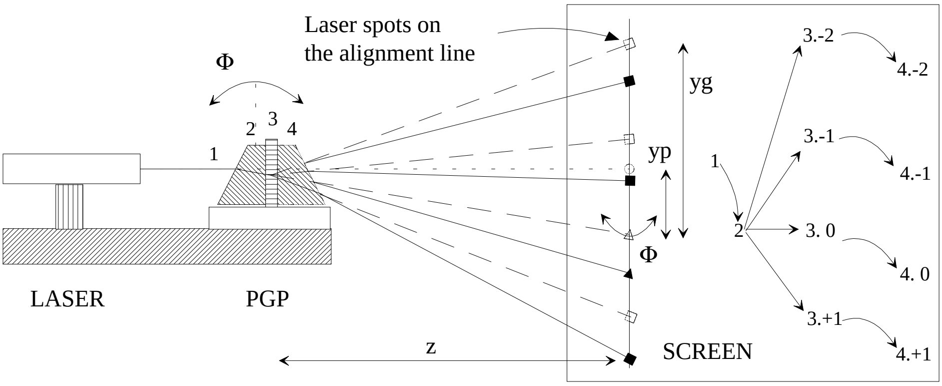

Figure 21. Process of alignment of a PGP component. Numbers 1–4 show the phases in the process: 1. laser spot on the screen without any optical component, 2. first prism in position, new location of the spot, 3. grating generates diffraction orders from +1 to -2, of which the zero order (3.0) retains its position, 4. the second prism shifts the spots downwards.

The accuracy of the angular alignment, ΔΦ, depends on the distance between the PGP and the screen, z, and on the method used to control the centring of a spot on the alignment line, Δx, as follows

Equation 12

$$\Delta\Phi = \arcsin\left(\frac{\Delta x}{y}\right),$$

where y is replaced by yp

Equation 13

$$yp = z * \tan\left(\arcsin\left\{n_{laser}\sin\left[\beta_1 - \arcsin\left(\frac{\sin\beta_1}{n_{laser}}\right)\right]\right\}\right)$$

for a prism and by yg

Equation 14
$$yg = z * \tan\left(\arcsin\left\{-\frac{\lambda_{laser} m}{d}\right\}\right)$$

for a grating, where the refractive index of the prism at the laser wavelength, λ_{laser}, is n_{laser} and the vertex angle is β_1. The diffraction order is m and the period of the grating is d.

Typically a HeNe-laser is used, λ_{laser} = 632.8nm, with beam diameter of 2 mm and the distance z = 2 m. The spot centring accuracy is Δx = 0.3 mm. If β_1 = 13.97°, the material of the prism is FK5 with n_{laser} = 1.486 and the grating has 460 lines/mm, so that the period is d = 2.174 µm and a diffraction order m = -2 is used, then $\Delta\Phi_g$ = 0.7 min and $\Delta\Phi_p$ = 4.3 min.

In practice there are often two more components in a PGP, low and high pass filters. All the components are cemented together, avoiding air bubbles in the cement layers.

3.4 An imaging PGP spectrograph

3.4.1 Adjustments

Four adjustments of the optics are needed during the basic construction of an imaging PGP spectrograph; focus adjustments for both the collimation and focusing optics and angular alignment around the optical axis for two of the following three components: the entrance slit, the PGP component and the detector.

The process of alignment of a spectrograph for the visible wavelength range, as introduced in section 5.1, may be presented as an example. First the collimation optics are adjusted using a collimator with a resolution reticle such as Siemens Star. The set-up can be seen in Figure 22.

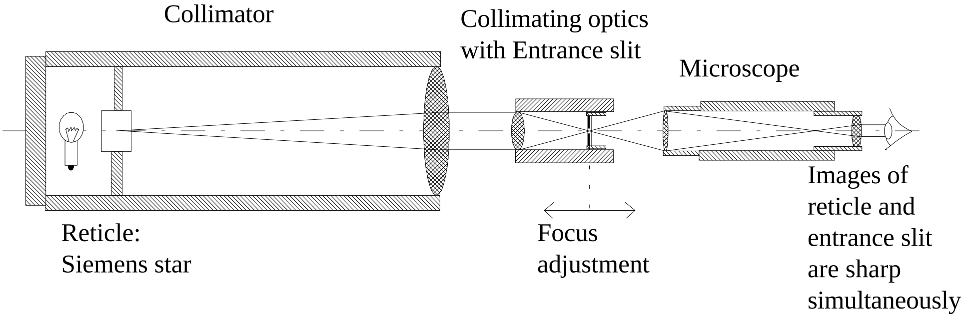

Figure 22. Adjustment of the focus of the collimating optics using a collimator and a microscope.

In this case all the optical and mechanical parts are then assembled and the PGP component is fixed in the housing. The cooled CCD camera, which is the detector in the spectrograph system, is connected to a PC with image processing software. The whole entrance slit is illuminated by a spectral lamp, see Figure 23. The focus of the focusing optics is the point at which the spectral lines are at their minimum width. To align the detector with the fixed PGP component, a small part of the entrance slit is illuminated with an optical fibre, for example, and the detector is turned until the spectrum lies over the same vertical pixel line (Figure 23, panel 2). The whole entrance slit is illuminated again and is aligned parallel with the horizontal pixel lines of the detector (Figure 23, panel 3).

An accurate adjustment unit equipped with micrometer screws was designed for this particular spectrograph system, see Figure 24, and the mechanical construction of the specrometer was designed so that the entrance slit and the camera could be adjusted externally. After each adjustment the part concerned was fixed with locking screws.

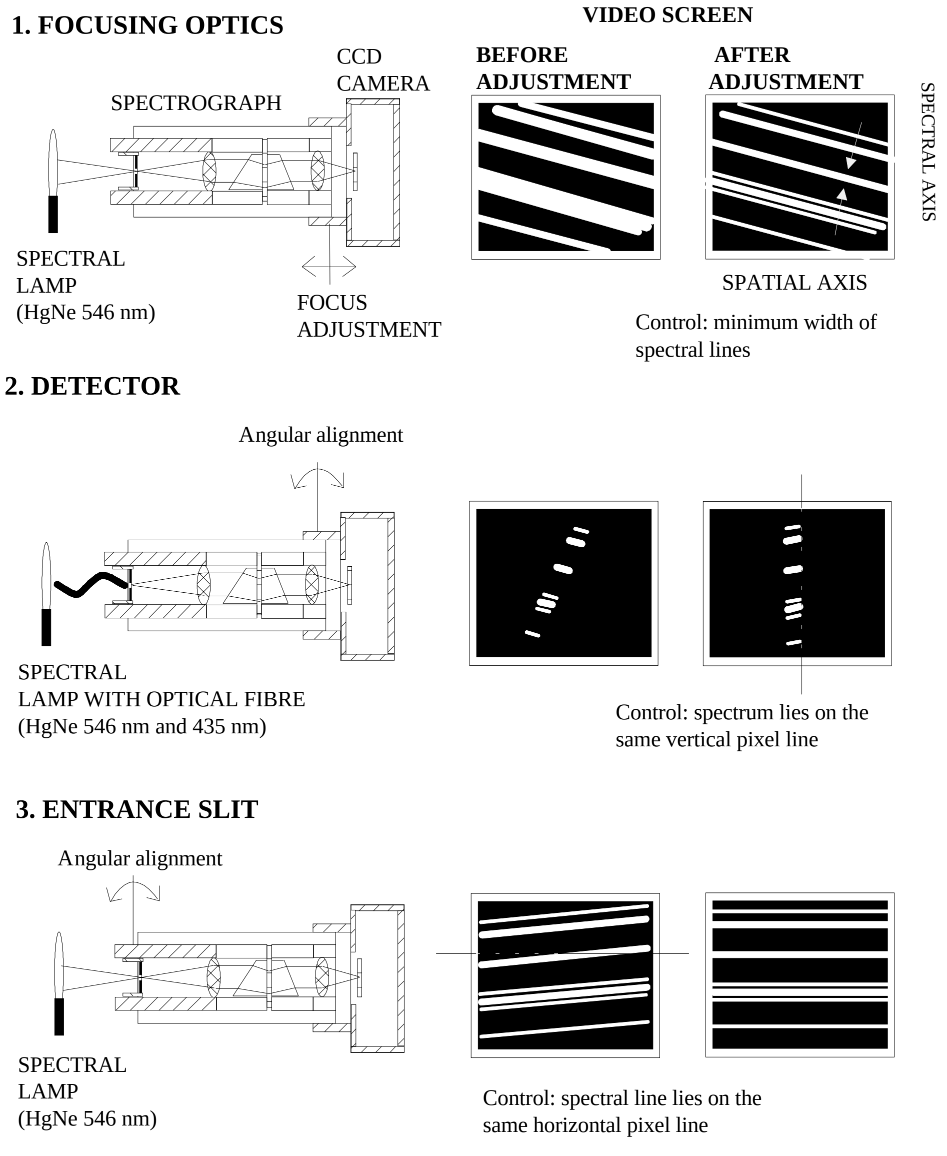

Figure 23. Adjustments made to an imaging PGP spectrograph for the visible wavelength range, with the image on a video screen before and after the operation. The PGP component is fixed. The wavelengths used for adjustment purposes are shown. 1. Focus adjustment for the focusing optics; 2. Angular alignment of the detector; 3. Angular alignment of the entrance slit.

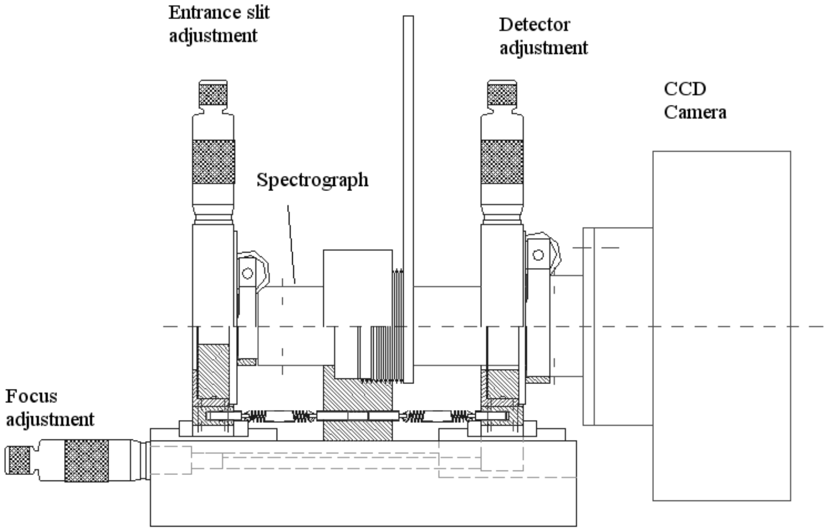

Figure 24. An adjustment unit equipped with micrometer screws was designed for external spectrograph adjustments.

3.4.2 Ghost image elimination

The construction developed to eliminate ghost images caused by reflections from the surfaces of the field lens and the surroundings of the entrance slit is shown in Figure 25. The slit was made in a 100 μm thick chromium layer on a glass substrate using laser ablation technology. The slit was tilted 10° between the two prisms. The light reflected from the AR-coated surface of the field lens was reflected further by the chrome layer around the slit aperture onto the black-painted baffle.

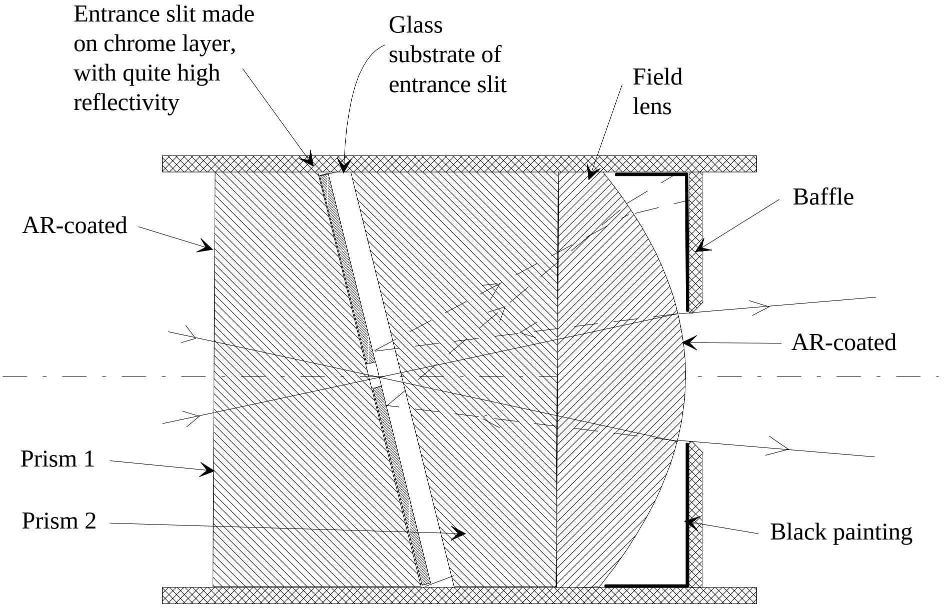

Figure 25. The entrance slit with the construction developed to eliminate ghost images caused by reflections from the surfaces of the field lens and the entrance slit.

3.4.3 Order-sorting filter

If the wavelength range is more than one order, grating spectrographs of this kind experience the problem of spectral overlapping caused by second-order diffraction. If the wavelength range is from 400 nm to 900 nm, for example, the wavelengths of the second order between 400 nm and 450 nm will overlie the spectral range of 800–900 nm in the first order. The problem can be avoided by an order-sorting filter construction as shown in Figure 26. This has been used in an UV-VIS spectrograph for wavelengths from 340 nm to 700 nm.

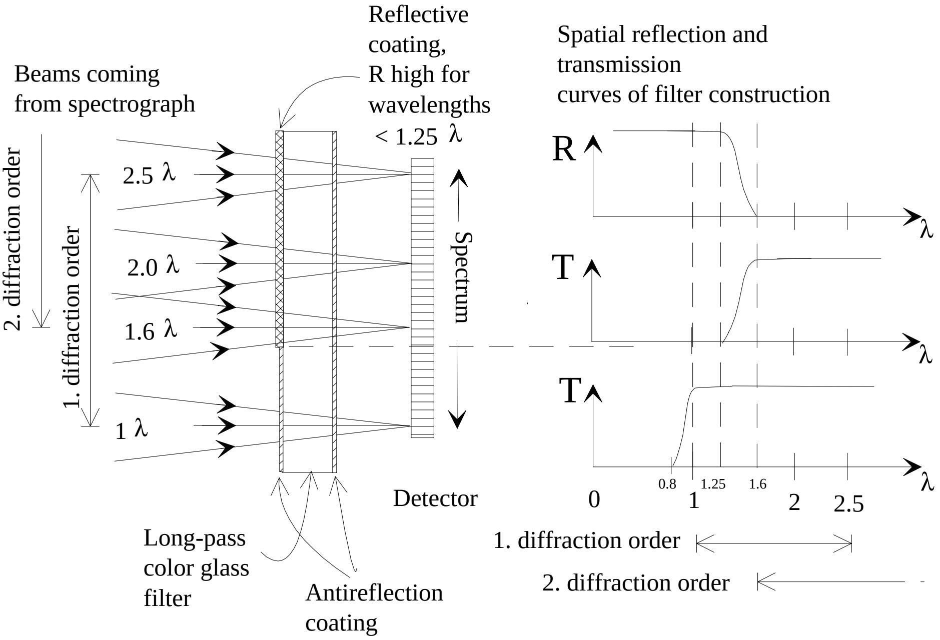

Figure 26. Principle of an order-sorting filter construction to remove spectral overlapping in a spectrograph.

4 Imaging PGP spectrographs designed for imaging spectroscopy

Two imaging PGP spectrograph designs are presented here: an airborne imaging spectrometer and an imaging UV-VIS-NIR microscope spectrograph system. Also, a commercially available PGP spectrograph is compared with two other low-cost spectrographs, quoted from Fisher et al. (1998).

The first prototype of the Airborne Imaging Spectrometer for different Applications (AISA) was evolved during the year 1992 for technology demonstration, performance verification and algorithm development. The first tests were performed at the end of the year and in the beginning of 1993. Development of the second prototype was started in 1994, but then the project was cancelled and the work continued only in 1996. The AISA was the first imaging spectrograph designed by the author.

The microscope spectrograph system, implemented in 1993–1994, serves to demonstrate the wide range of applications of imaging spectroscopy.

The author's contributions to these spectrographs were the optical design including the PGP, the layouts of the mechanical designs and the assembly and alignment work associated with the opto-mechanical systems, including some test measurements.

4.1 Prototype of the AISA airborne imaging spectrometer

4.1.1 Instrument overview

This section is based on Braam et al. (1993a) and Specim (2001a).

AISA is a versatile programmable imaging spectrometer based on the pushbroom imaging mode of operation. The instrument consists of two parts: sensor head and a portable PC, see Figure 27. The front end contains the optics and the CCD detector with related electronics and a microcontroller for CCD operation. The controller and data acquisition system were built around a portable computer. The spectral range was chosen to be 430–900 nm, with a spectral resolution of 1.56 nm. This choice was based on the requirements of the potential users of the instrument and the technical limitations of the CCD and the optics. The spatial resolution has been defined as 1 meter and 360 pixels per swath using an aircraft flying at 50 m/s and 1000 meters above the ground.

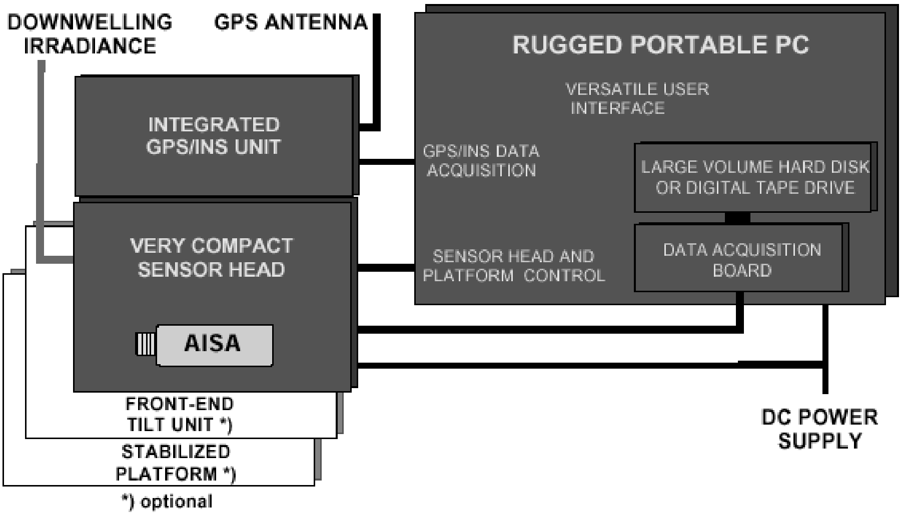

Figure 27. Block diagram of AISA (Specim 2001a).

The data acquisition system uses the analogue CCD video, digital synchronisation and sampling signals provided by the front end. The system digitizes the analogue CCD video data into 12-bit pixels and stores the raw data as packets of frames. Every packet contains a header, including auxiliary information such as GPS data.

The instrument is flexibly programmable during flight and the features which can be selected are given in Table 1. Operational use requires wide spatial coverage and the collecting of spectral information that is specific to the desired application. In research work it is often important to have full spectral coverage, but achieving both of these goals with reasonably priced storage medium was not possible at that time. This led to the implementation of 4 modes in which the spatial and spectral resolution could be selected quite freely (Table 2). Mode D, for example, is very useful for research work, as it enables full spectral resolution to be attained for a large number of pixels. These channels are also very useful for the segmentation of homogeneous areas, which may then be found to contain many full spectral samples.

Table 1. Selectable features of the first prototype of the AISA.

* number of channels [I   286]
* wavelength [430–900 nml
* bandwidth [1.6–9.4 nm]
* spectral, spatial or combined spectral and spatial modes
* rate of data storage
* integration time
* geometric resolution
* radiometric resolution.

Table 2. Description of the 4 AISA modes.

Mode	**Description**
A	Complete CCD information is stored.
B	A number of spectral channels are selected for storage, the width of each being selected between 1.6–9.4 nm. The maximum number of channels which can be used is a function of integration time, channel spacing and the total sum of channel bandwidths.
C	Full spectral information is stored on 47 equally spaced spatial lines.
D	The user can select a set of spatial channels and a set of views with full spectral information within the limits of the data recorder.

4.1.2 Spectrograph design

The optics of the first prototype of an airborne imaging spectrograph is shown in Figure 28. The CCD in this prototype had 288 x 384 elements. The pixel size was 23 µm x 23 µm, so that the dimensions of the sensitive area were 6.624 mm x 8.823 mm. The optics were based on two triplets, f 40 mm, f/2.8, from Melles-Griot Inc, type 01 LAS 003. The field lens is also a catalogue lens: 01 LPX 047, f 30.0 mm, f/2.56, and the wavelength range was 450–900 nm. The design of the first AISA and its test results were reported by Braam et al. (1993a). The laboratory and field tests were promising. The first test flight was carried out on 26th February 1993, leading to acquisition of the first image, shown in Figure 29 (Braam et al. 1993a).

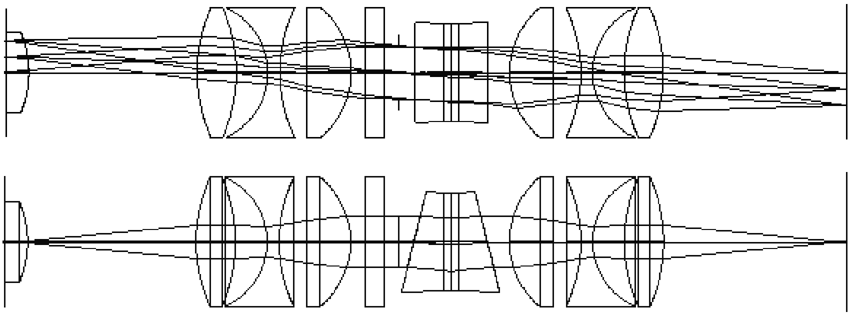

Figure 28. Optics of the first prototype for an airborne imaging spectrograph. The longpass filter is located in front of the aperture stop.

Figure 29. The first image acquired with the first AISA. The timber store of a paper and saw mill. Altitude 1072 m, v = 50 m/s, wavelength 547.3–556.1 nm (Braam et al. 1993a).

The optical construction of the second prototype can be seen in Figure 30. The f/4 optics is basically the same as in the first AISA. The spectral range was enlarged, being from 430 nm to 900 nm, and therefore the PGP was redesigned. The longpass filter, a Hoya Colour Glass Sharp Cut Filter Y-42, was integrated inside the PGP. This has $\lambda_{cp}(\tau_i = 0.50) = 422$ nm, $\lambda = 430$ nm, and $\tau_i = 0.84$ with a catalogue thickness of 2.5mm. The aperture stop is located in front of the PGP, because the idea of integrating the stop inside it came later.

The parameters of the PGP were as follows: the grating line number was 315 l/mm, the vertex angle of the first BK7 prism was 11.8° and that of the second 11.2°. According to the simulations, the on-axis centring of the spectrum was good: the wavelength of 430 nm had a spot on the detector in a position 3.18 mm below the optical axis and 900 nm had one 3.16 mm above it. The length of the spectrum was 6.34 mm.

This spectrograph also suffered from the problem of spectral overlapping caused by the second diffraction order. Wavelengths of the second order between 430 nm and 450 nm overlay the spectral range of 860–900 nm in the first order. The design task for the author did not include solving this problem. The problem can be avoided by the filter construction shown in Figure 26.

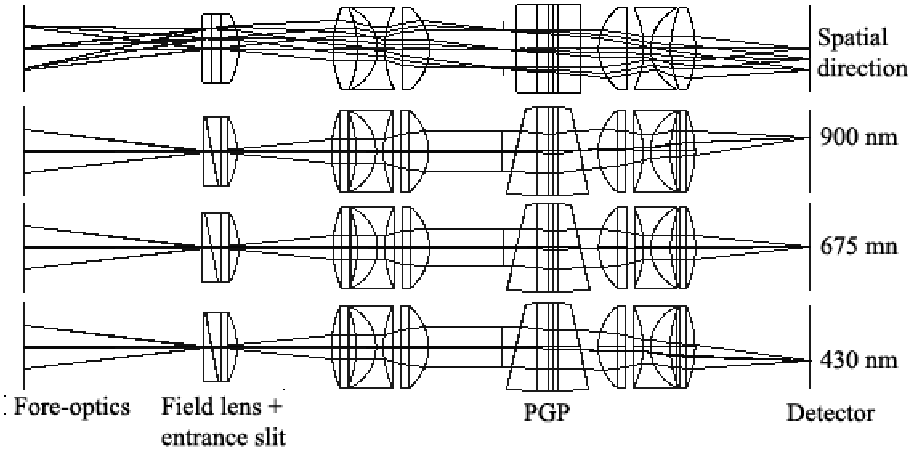

Figure 30. Optics of the second prototype of the airborne imaging spectrometer, seen from the spatial and spectral directions and traced with three wavelengths.

The fore optics consisted of a Schneider Xenoplan 1.4/23 C-mount video camera lens with a focal length of 22.5 mm and a maximum aperture of f/1.4 designed for a wavelength range of 400–1000 nm. The data available on this lens showed excellent transmission over the whole spectral range of 430–900 nm.

The entrance slit was of width 23 µm and length of 10 mm. The principle of the construction around the entrance slit was as shown in Figure 25. The length of the detector in a spatial direction was 8.8 mm, which set the field of view to 21°. The width of the slit gave an IFOV of 1 mrad for the 384-column CCD. This gave an across-track resolution of 1 meter at an altitude of 1000 meters.

The AISA Airborne Imaging Spectrometer system has been commercially available since 1996. Papers published about it include an introduction by Mäkisara et al. (1993), a report on the development of a system for radiometric and geometric correction of AISA data by Mäkisara et al. (1994), a description of its application to the national forest inventory by Mäkisara and Tomppo (1996) and a discussion of its use for monitoring of inland and coastal waters by Kutser et al. (1998).

4.2 Imaging UV-VIS-NIR microscope spectrograph system for pulp quality inspection

The optical design of an imaging spectrometer system for microspectroscopy is described in detail in this section. The author's contributions to the system were the design of the imaging optics of the PGP spectrographs for VIS and NIR (excluding illumination), the lay-out of the mechanical design and the assembly and alignment of the opto-mechanical system for VIS and NIR spectrographs, including some test measurements. The customer was supplied one year later with an Offner-type UV spectrograph with relay optics for the UV channel designed by the author and he has also specified the whole spectrograph based on a reflecting grating.

This system is the most complicated optical instrument, that the PGP concept is applied to.

4.2.1 System overview

The imaging UV-VIS-NIR microscope spectrograph system was developed for the spectral measurement of micrometer-sized objects such as wood fibers by means of transmitted light over a broad wavelength range from ultraviolet to NIR, i.e 250–975 nm. It can measure objects up to 900 μm x 27 mm in size with a spatial resolution better than 5 μm x 5 μm and a spectral resolution of 5 nm.

A schematic diagram of the spectrograph system is presented in Figure 31. The system consisted of two light sources, a halogen lamp and a xenon lamp, a motorized sample stage, the imaging optical system with three spectrographs and CCD cameras. The stage and data acquisition were controlled by a PC and the image processing and analysis were performed on a workstation.

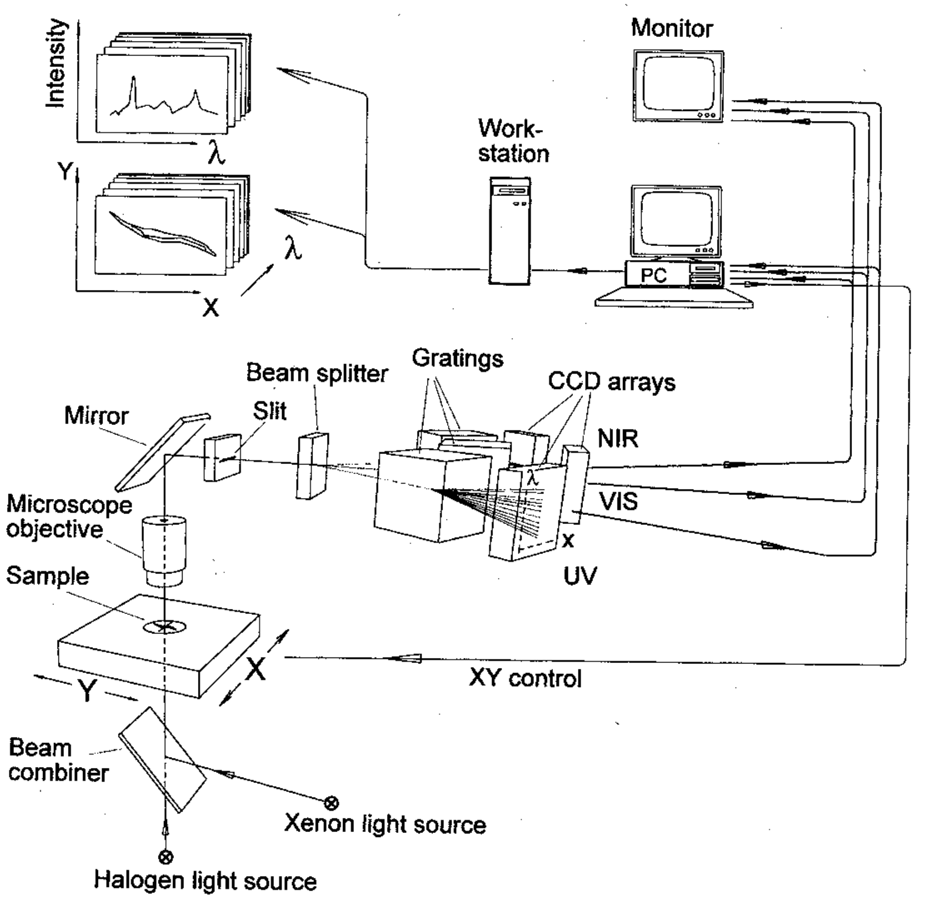

Figure 31. Schematic diagram of the imaging UV-VIS-NIR spectrograph system. The author has designed the optics (Johansson and Pettersson 1997).

4.2.2 Basic layout of the optical system

The optical requirements for an imaging UV-VIS-NIR spectrograph for microspectroscopy were that the wavelength range should be very broad, from 250 nm to 975 nm, with a spectral resolution of 5 nm, the field of view on an object should be 1.5 mm and the spatial resolution should be 5 μm.

Since it was not possible to cover the broad wavelength range with 5 μm spatial resolution using a single imaging spectrograph, the range was divided into three parts: UV from 250 nm to 450 nm, VIS from 400 to 700 nm and NIR from 700 to 975 nm. A schematic layout of the imaging optics of the instrument is shown in Figure 32.

A reflective microscope objective was used because of the broad spectral range. This type of objective contains no refracting elements, thereby eliminating all chromatic aberrations. The object to be measured was imaged on a system entrance slit, called the main slit, which was common to the three spectrographs and ensured that they all measured excactly the same area on the object at the same time.

The wavelength range was divided by dichroic beam splitters located after the slit. This arrangement was possible because of the small numerical aperture of the microscope objective in the image space.

An imaging PGP spectrograph design was employed for the visible and near-infrared wavelength ranges, with the main slit serving as an entrance slit for these spectrographs. In the UV part an image of the main slit was formed by a relay lens system on the entrance slit, Slit 2, of an UV Offner spectrograph module based on all reflective optics.

A removable folding mirror and an eyepiece were installed in the instrument for visual inspection and focus adjustment. When the mirror was taken away from the optical path, the objective and eyepiece formed a microscope. For focus adjustment, a reticle in the eyepiece was located in the image plane of the microscope objective. The same optical distance to the slit was achieved when the mirror was switched in the optical path.

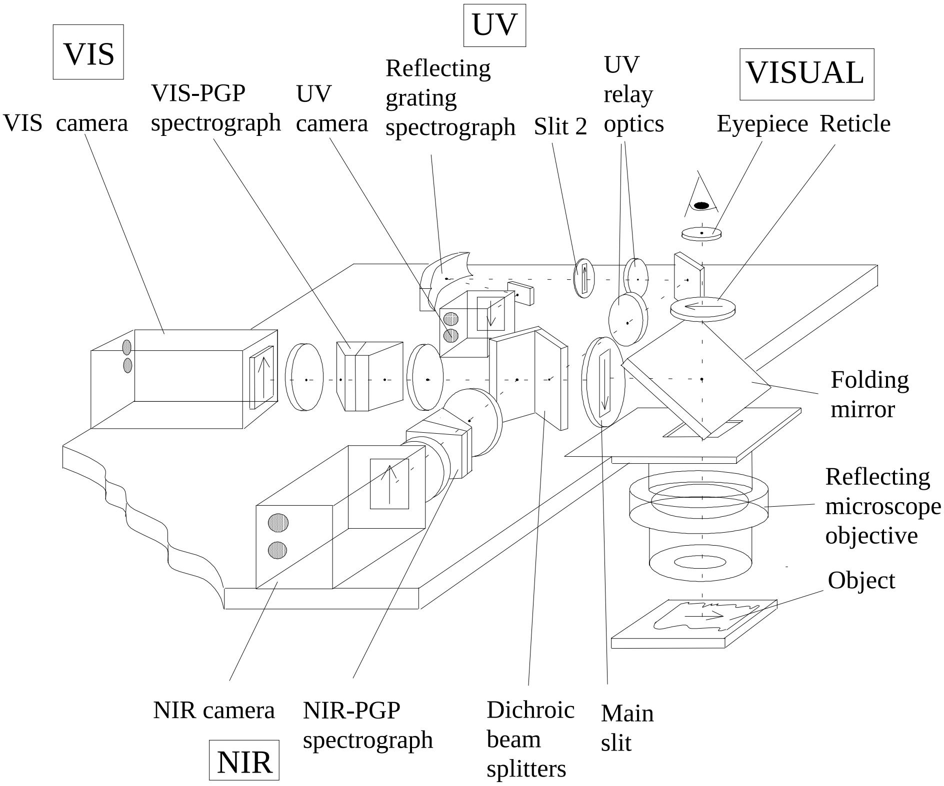

Figure 32. Schematic layout of the optical system for the triple imaging spectrograph for UV-VIS-NIR microspectroscopy.

4.2.3 Design of the optical system

4.2.3.1 Cameras for VIS, NIR and UV ranges

According to the requirements for spectral resolution, 60 spectral channels were needed in the VIS range, 55 in the NIR range and 30 in the UV range. Each channel consisted of at least two pixels. Thus the minimum number of pixels in the spectral direction was 120 for VIS, 110 for NIR and 60 for UV. The spatial resolution was more demanding. When the field of view was 1.5 mm and the spatial resolution 5 μm, the spatial direction of the detector had to have at least 600 pixels.

A standard 2/3” CCD matrix camera, Kappa CF 7, with 800 (H) x 582 (V) pixels was selected for both the VIS and NIR ranges. The size of each pixel was 11µm (H) x 11.3 µm (V) and the matrix 8.8 mm (H) x 6.6 mm (V). The relative sensitivity of the detector in the VIS range was 0.2–0.3 between 400 nm and 500 nm and rose from 0.3 up to 0.8 from 500 nm to 700 nm. The detector had a good response, over 0.8, in the NIR range of 700–1000 nm. When the field of view on the object was 1.5 mm and the length of the detector in the spatial direction was 8.8 mm, a total magnification about 6x was needed, whereupon a 5 µm object was imaged on 2.7 pixels of the detector.

The camera for the UV region was also of the 2/3” CCD matrix type, the SBIG ST-6V of the Santa Barbara Instrument Group. The 750 (H) x 242 (V) pixels formed a 8.63 mm (H) x 6.53 mm (V) detector, which was thermoelectrically cooled. The size of each pixel was 23 µm (H) x 27 µm (V). The average quantum efficiency for UV light was acceptable, 26 %. The camera was used in a mode in which 2 pixels were added in the spectral direction for a higher signal while still fulfilling the spectral resolution requirements for the system. It was also possible to set the exposure time according to the light intensity level of the object to be measured.

4.2.3.2 Reflecting microscope objective

On account of the broad spectral range, a reflecting microscope objective from Ealing Electro-Optics was selected. The Schwarzschild design consisted of a small primary convex mirror and a large secondary concave one and had spherical, coma and astigmatic aberrations close to zero. This type of objective has also zero chromatic aberration due to the absence of refractive optical elements.

As a total magnification of 6x was needed for the VIS and NIR spectrograph, the lowest-power objective, 15x, was selected and 12x magnification was used (Figure 33). The focal length was 13 mm. Since 6x magnification was shown in an optical simulation to cause unacceptable image quality, the spectrographs had to have a magnification of 0.5x in this instrument. When the optics were used for 12x magnification, the numerical aperture was 0.216 in the object space but only 0.018 in the image space. The working distance was long, 24.8 mm.

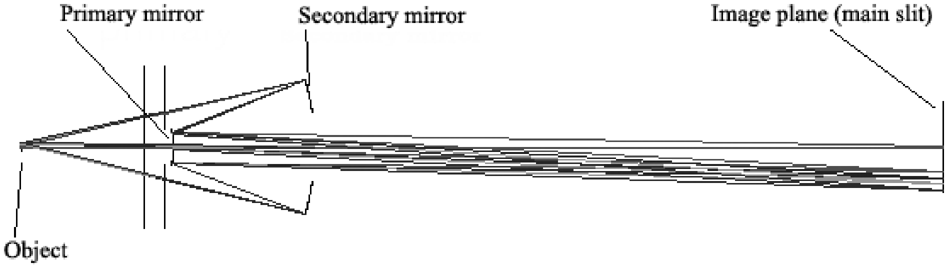

Figure 33. A 15x reflecting microscope objective used for 12x magnification.

4.2.3.3 Main slit and dichroic beam splitters

The main slit was located on the image plane of the microscope objective, Figure 33. The width of the slit was selected to be 80 μm, corresponding to a 6.7 μm width of the view on the object. The width also determines the spectral resolution of the spectrographs. The slit was an UV-transparent sapphire window plated with chromium and copper. It was produced by an etching process to provide less than 4% width variations.

The broad wavelength range was divided into three parts by two dichroic, multilayer dielectric mirrors with a 45° angle of incidence, the first reflecting UV and transmitting VIS and NIR and the second reflecting NIR (Figure 32). According to measurements, the first mirror reflected wavelengths between 250 nm and 400 nm with an efficiency of over 90%, while the transmission for wavelengths longer than 480 nm and up to 1100 nm was over 80%. For 440 nm the transmission was 50%. The custom-designed mirror was made by Technical Optics Limited, UK.

The second mirror, which transmitted VIS and reflected the NIR range, had a transmission of 65% for 400 nm and varied from 70% to 90% for 450–680 nm. The reflectance was 60% for 700 nm and over 90% for wavelengths longer than 750 nm.

As can be seen in Figure 32, a vertical orientation was chosen for the main slit, because the dimension of the beam splitter along the optical axis would then be smaller and it would thus be possible to assemble it between the main slit and the collimating lens. The advantage of this solution can be seen in Figure 34a and b.

4.2.3.4 Imaging PGP spectrographs for VIS and NIR

The imaging spectrographs for VIS and NIR had to have a magnification of 0.5x, which was the ratio of the focal length of the focusing lens to that of the collimating lens. A focal length of 80 mm was chosen for the collimating lens and 40 mm for the focusing lens. The optical arrangements and the components of the VIS spectrograph can be seen in Figure 34, where a ray tracing of the central wavelength is also shown. The folding mirror was not taken into account in the optical simulations.

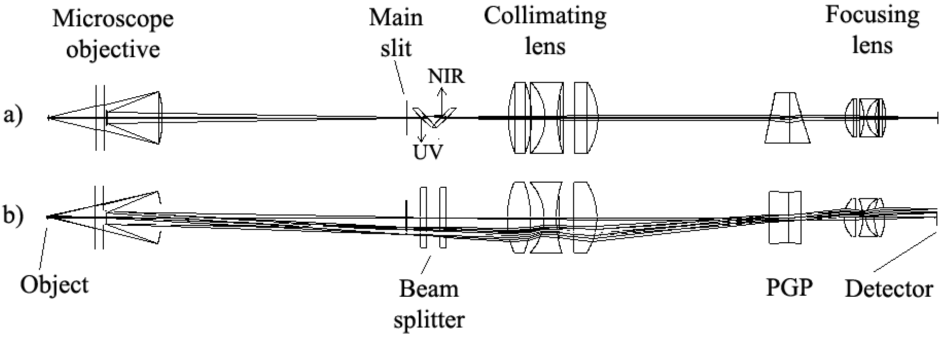

Figure 34. Ray tracing of the VIS spectrograph seen from a) the top and b) the side.

The NIR spectrograph was similar to the above except that the PGP component was optimized for the NIR range, see Figure 35. A wedge was added to the optics to compensate for the wavelength dependence of the back focal length, as the triplets had been designed for visible light. This chromatic aberration correction method worked here because, due to the small numerical aperture of the instrument, the wavelengths were separated spatially after the focusing lens.

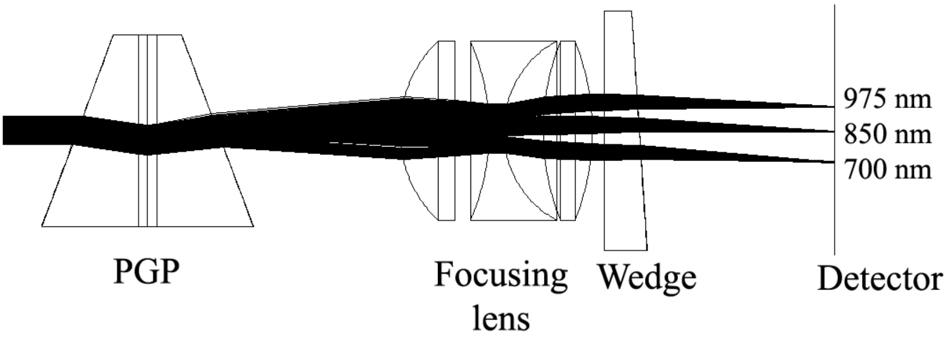

Figure 35. The last few components of the NIR spectrograph and a ray tracing of three wavelengths.

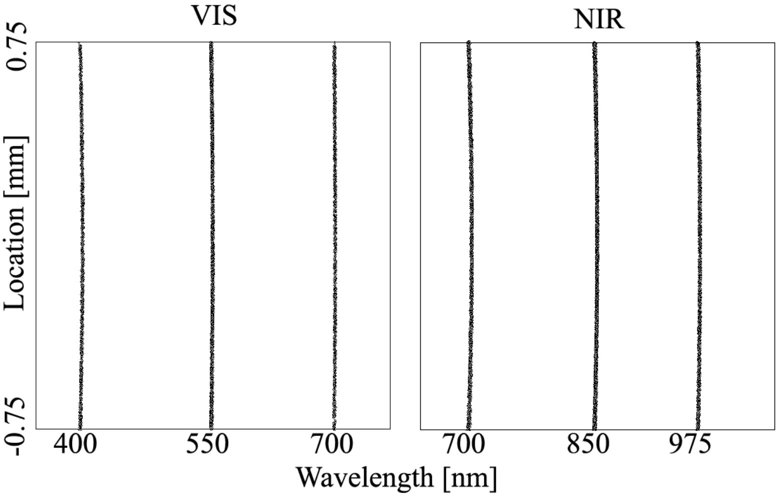

Figure 36. Simulated spectral lines on the detectors (9.0 mm x 9.0 mm) of the VIS and NIR spectrographs. The real sizes of both detectors were 8.8 mm x 6.6 mm. Location is expressed on the object to be measured.

The theoretical spectral resolution of the VIS and NIR spectrographs was approximately 2 nm, because the width of the slit was 80 µm. Simulated spectral lines of some wavelengths in the VIS and NIR spectrographs are shown in the

Figure 36. There were intentional overlaps between the three spectrographs to permit internal sensitivity calibration of the system. This overlap was eliminated by the data aquisition procedure.

4.2.3.5 Imaging Offner spectrograph for UV

The optical arrangement of the UV spectrograph differed from that of the VIS and NIR spectrographs. The microscope objective, the main slit and the dichroic beam splitter were the same for all three, but the most important part of the UV optics was a custom-designed imaging Offner spectrograph module made by Jobin Yvon and based on a convex reflection grating, as shown in Figure 37. Because of the small numerical aperture of the system, the image quality of the module was high even at the edges of the slit.

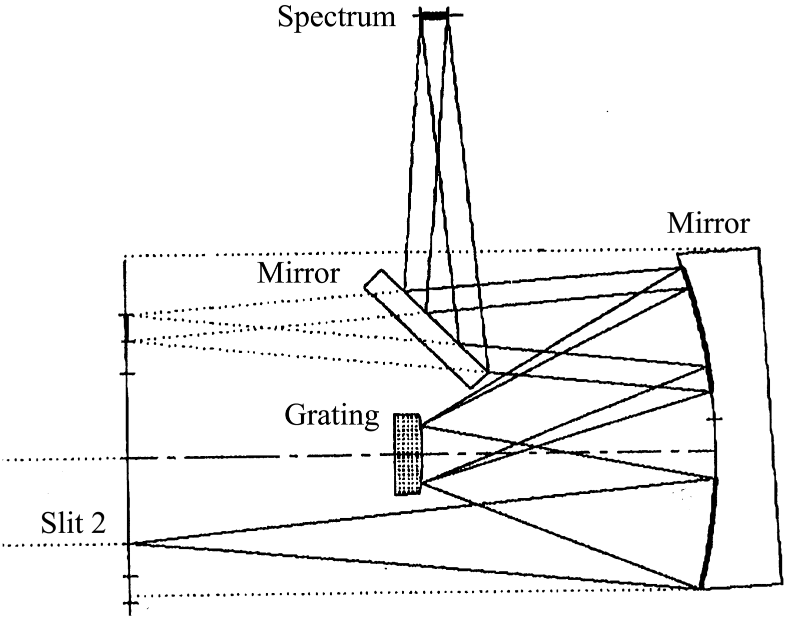

Figure 37. Offner type of UV spectrograph module based on a reflection holographic grating (top view).

As the UV spectrograph module, forming a single mechanical unit, had its own entrance slit, Slit 2, it was not possible to assembled it so that the main slit could be used as its entrance slit. Relay optics were needed to form an image of the main slit on Slit 2.

The magnification of the UV spectrograph had to be higher than that for the VIS and NIR spectrographs in order to achieve equal spatial resolution, because the pixel size in the spatial dimension is twice as large as in the UV detector. Two pixels were needed to resolve a 5 µm object point, which means a 46 µm spot size on the detector. The microscope objective had 12x magnification and the UV spectrograph module unit magnification. According to optical simulations using two air-spaced UV f100 mm achromats made of lithium fluoride and silica, the formation of a relay lens system with 0.8x magnification gave good enough image quality and a large enough field of view (FOV): a 0.8–0.9 mm line on the object. If the magnification was increased, the FOV became smaller. This was more than sufficient for the practical measurement applications planned, as the total magnification of the UV spectrograph was 9.6x. The front optics and relay lens system for the UV part are shown in Figure 38. The optics were so long that a folding mirror had to be added between the achromats. Spots of three UV wavelengths 254 nm, 302 nm and 391 nm, imaged from the object to Slit 2 are shown in Figure 39, where the chromatic aberration can be clearly seen. In spite of this, the image quality was good, however: for 22 lp/mm MTF > 0.3 up to 0.7 mm of FOV on the object and MTF >0.15 for 0.8 mm of FOV.

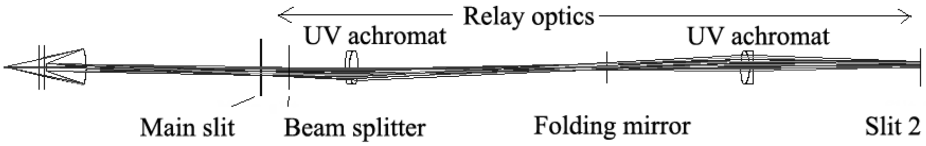

Figure 38. Front and relay optics for the UV spectrograph (side view).

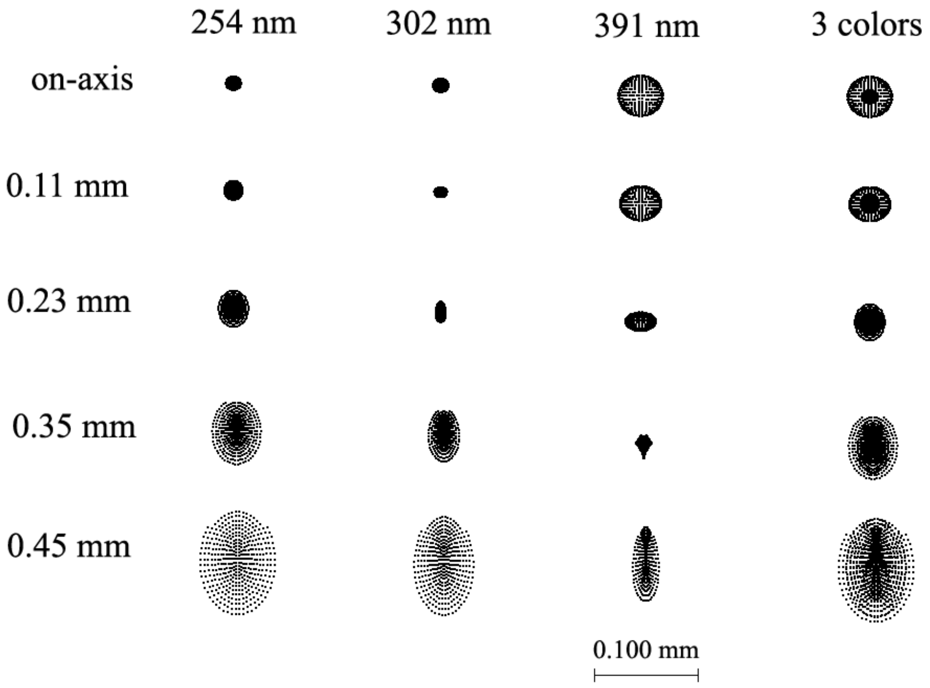

Figure 39. Simulated spot sizes for three wavelengths and combined spots on Slit 2 from different points on the object. Chromatic aberration can be clearly seen.

4.2.4 Test measurements performed with the optical system

Mercury and neon spectral calibration lamps were used for optical measurement of the spectral resolutions and wavelength ranges of the spectrographs. Transmission gratings of different line pitches etched in a metal layer on a glass substrate were used for investigating the spatial resolution. The grating was illuminated from underneath and the microscope objective focused on it. The 10 µm / 10 µm pitch (10 µm transparent line and 10 µm metal stripe) was clearly resolved for all wavelength ranges, as was the 4 µm / 4 µm pitch. Spatial resolution at the shortest UV wavelength was not examined due to the lack of UV-transparent gratings, but there was no physical reason why the resolution should have been different in this region. The field of view was examined by calculating the number of lines of the 10 µm / 10 µm pitch grating seen in each spectrograph. The results are collected together in Table 3.

Table 3. Results of the optical test measurements performed on the spectrograph system.

Parameter	**Value**	**Notice**
NIR spectrograph		**PGP spectrograph**
- spectral resolution	better than 5.0 nm	Peaks 743.9 nm and 748.9 nm resolved, $\Delta\lambda$=5.0 nm Peaks 748.9 nm and 753.6 nm resolved, $\Delta\lambda$=4.7 nm
- wavelength range	672–976 nm	
- spatial resolution	4 µm	4 µm/4 µm pitch grating can be resolved
- field of view	1.42 mm	71 lines of 10 µm /10µm pitch grating can be seen on the object
VIS spectrograph		**PGP spectrograph**
- spectral resolution	better than 5.0 nm	Peaks 585.2 nm and 588.2 nm resolved, $\Delta\lambda$=3.0 nm Peaks 667.8 nm and 671.7 nm resolved, $\Delta\lambda$=3.9 nm
- wavelength range	390–693 nm	
- spatial resolution	4 µm	4 µm/4 µm pitch grating can be resolved
- field of view	1.42 mm	71 lines of 10 µm /10µm pitch grating can be seen on the object
UV spectrograph		**Offner spectrograph**
- spectral resolution	better than 5.0 nm	Peaks 296.7 nm and 302.2 nm resolved, $\Delta\lambda$=5.5 nm Peaks 404.7 nm and 407.8 nm resolved $\Delta\lambda$=3.1 nm
- wavelength range	251–458 nm	
- spatial resolution	4 µm	4 µm/4 µm pitch grating can be resolved
- field of view	0.9 mm	45 lines of 10 µm /10µm pitch grating can be seen on the object
Spectrograph system		
- spectral resolution	< 5.0 nm	
- spatial resolution	4 µm	
- wavelength range	251–976 nm	
- field of view	0.9 mm 1.42 mm	UV VIS and NIR

4.2.5 Application measurements

Johansson and Pettersson (1997) present the following results obtained with the imaging UV-VIS-NIR microscope spectrograph system. Wood pulp fibres have an average length of 2–4 mm and width of 20–40 µm. A spectral image of such a fibre is shown in the wavelength ranges of 280–285 nm and 880–885 nm in Figure 40 a and b, respectively. The images were fairly sharp, especially in the UV range, where even 1 µm details can be resolved.

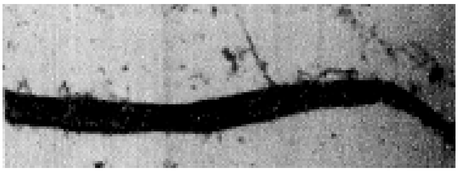

a) 280 - 285 nm

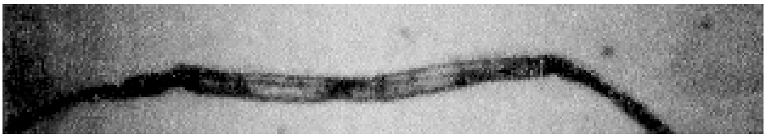

b) 880 - 885 nm

Figure 40. (a) A spectral image from the wavelength band 280–285 nm showing part of a soft wood pulp fibre of width varying between 20 µm and 50 µm. (b) A corresponding spectral image from the wavelength band 880–885 nm (Johansson and Pettersson 1997).

4.3 Comparison of the imaging PGP spectrograph with two other hyperspectral imaging spectrographs

Fisher et al. (1998) have compared three low-cost (<$100K.) hyperspectral imaging spectrographs: a PGP spectrograph, ImSpector™ V9 (Figure 41b), built by Specim Ltd, Holospec™ (Figure 41a), built by Kaiser Optical Systems Inc., both off-the-shelf spectrographs based on a transmission grating, and a custom-designed all-reflective Offner spectrograph, called VS-15 (Figure 41c). The specifications of the spectrographs are collected together in Table 4.

The principle of the optical construction of this PGP spectrograph is shown in Figure 30, but the optics for ImSpector™ (see Figure 14) have been re-designed to be faster, f/2.8. The unique characteristics of the PGP spectrograph are its small size (compare the sizes in Figure 41a and b), ease of mounting and straight optical axis. The entrance slit was 27 µm x 8.8 mm. The degree of correction of smile, keystone and image quality is determined by the complexity of the relay optics.

The Holospec™ spectrometer consists of two Nikon f 75 mm lenses, a folding mirror and a transmission grating, as seen in Figure 41a forming a simple but large design with high performance imaging. The field is defined by a 12 µm x 12 mm slit and the aperture stop determined by the grating aperture.

The Offner spectrograph, VS-15, was designed by the authors of the paper in question, Fisher et al. (1998). The spectrograph without folding mirrors, as shown in Figure 6d, is telecentric (entrance pupil at infinity). Telecentric spectrographs do not match most available C-mount or photographic lenses, which typically have their exit pupils located from 10 mm to 50 mm in front of the image plane. The result is significant vignetting. The authors claim that some modifications will be adopted in the next generation of systems to solve this problem. The grating groove density was 150 l/mm, but the problem was to make blazed gratings on a convex substrate while retaining low polarization and scatter (Fisher et al. 1998).

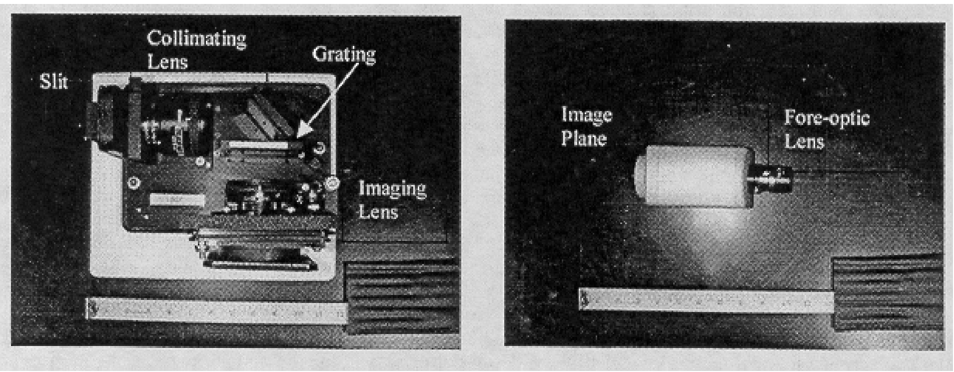

a) Holospec™ Spectrograph b) PGP Spectrograph, ImSpector™

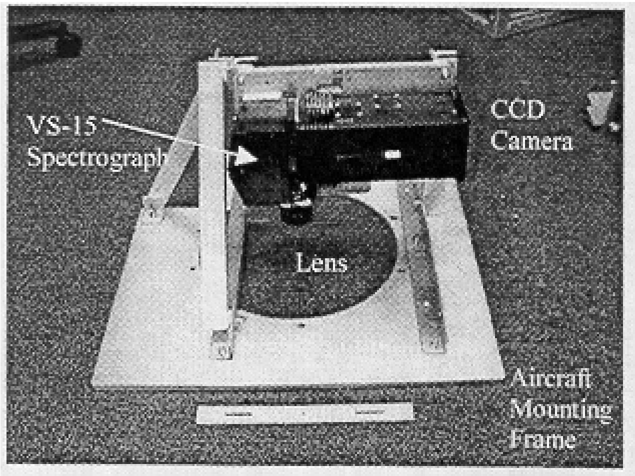

c) Offner Spectrograph, VS-15

Figure 41. The spectrographs compared by Fisher et al. (1998).

The performance metrics were evaluated by imaging onto a 1024 x 1024 CCD array with 12 μm pixel size. A Schneider f 25 mm f/1.4 C-mount lens was used as the fore-optics, because of its low distortion and correction for the broad spectral range from 400 nm to 1000 nm. The results are a convolution of the properties of the fore-optics, the slit, the spectrograph and the detector sampling, and also of the accuracy of the focusing and alignment of the camera, and not just of the spectrograph alone (Fisher et al. 1998).

The specifications of the spectrographs and the measurements performed on them are presented in Table 4. The measured keystone for the PGP spectrograph was 0.8%, with a 48 µm spot size, which included a contribution from the 27 µm slit in this particular spectrometer. Smile was 1.0%, due to the short focal length of the spectrograph optics. Measurements performed on the Holospec™ spectrograph showed a spot size of 3 pixels in spite of a slit height of 12 µm, smile 0.2% and keystone 0.6%. Some field curvature across the spectra was observed. The Offner spectrometer had a keystone of 48 µm (4 pixels), which was most likely due to alignment problems in the mirrors or in the grating recording process. According to the simulation, the keystone should be 20 µm. The smile was simulated to be <1 µm, which agreed with the measured value of <1 pixel, which is 12 µm. The largest measured spot size was 2 pixels (Fisher et al. 1998).

The PGP spectrograph is equal in performance to its competitors in this comparison in spite of its very small size and easy mounting, both features that enhance its usefulness.

Table 4. Summary of specifications and measurements (Fisher et al. 1998).

Specifications	**ImSpector™**	**Holospec™**	**VS-15**
- Size (LxWxH)	135x70x60mm	180x240mm	100 x100 mm
- Spectral range	430–900 nm	400–800 nm	400–1000 nm
- f-number	f/2.8	f/2.2	f/2
- Slit dimensions	27µm x 8.8mm	12µm x 12 mm	12µm x 12 mm
- Spectral resolution	7 nm	2.5 nm	5 nm
Measurements			
- Smile	1.0 %	0.2 %	< 0.1 %
- Keystone	0.8 %	0.6 % *	0.8 %
- Measured spot size	4 pixels	3 pixels	2 pixels

(*corrected according to the text in the publication. The original table contained the figure 0.4%)

5 Imaging PGP spectrographs designed for fibre optic applications

This chapter presents the designs for an intelligent PGP spectrometer for use in multiple points fibre optic remote spectroscopy and a PGP spectrograph for fibre optic Bragg grating sensor network interrogation.

The author's contributions to these spectrograph systems were the design of the optics of the spectrographs, the lay-out of the mechanical design and the assembly and alignment of the opto-mechanical system including test measurements. The application measurements, which are presented here, were done by Mr Tapio Vaarala and Mr Pekka Suopajärvi, Research Scientists at VTT Electronics.

5.1 An intelligent PGP spectrograph for on-line industrial applications

5.1.1 Background

Industrial process control and quality inspection based on spectral information on materials is accurate, but because it is mostly done off-line in a laboratory the response time is long. The most effective way is to use on-line, real time measurements made with imaging or multiple point spectrometers instead of single point measurements. The advantages of such spectrometers are obvious, i.e. real time measurement, no scanning movement, resulting in simpler mechanics, and simultaneous measurement over a line or multiple points, but there are also disadvantages, namely the huge amounts of data that have to be collected and processed on-line or stored for later processing. On-line spectrograph systems also have to be mechanically robust, easy to assemble, protected against dust and humidity and capable of being filled with nitrogen gas if required.

The problem caused by the huge amount of data generated in imaging spectroscopy can be overcome by using data reduction schemes in which only those wavelengths and spatial locations that are of special interest are selected for conversion into digital form. In this way the amount of data can be effectively reduced, which will benefit later data processing (Herrala and Okkonen 1996). This enabled a small PGP spectrograph and the programmable detector electronics developed to be integrated into a single mechanical unit forming an intelligent spectrometer.

5.1.2 Multiple points spectrograph

5.1.2.1 Optical requirements

The optical requirements and parameters for the fibre optic remote spectrograph are summarized in Table 5. The wavelength range, from 400 nm to 800 nm, and the spectral resolution of 5 nm are reasonable for many process control applications and colour measurements. One channel is needed for a light source reference and 15 channels for object point remote measurements. The idea for the construction of the multi point spectrometer is shown in Figure 42. The detector is a Texas Instruments TC277, ½” virtual phase CCD matrix. The optical resolution along the λ axis is calculated from the formula $R_\lambda = (\lambda_L - \lambda_S)/(\Delta\lambda a H_\lambda)$, where a is an assembly coefficient for the detector and H_λ is the height of the detector in the spectral direction, see Figure 16.

Table 5. Features of the fibre optic remote spectrograph.

Feature	**Symbol**	**Value**
Wavelength range [nm]	λ_S–λ_L	400–800
Wavelength resolution [nm]	$\Delta\lambda$	5
Numerical aperture of spectrograph	NA	0.125
Number of channels, i.e fibres		16
Numerical aperture of fibres		0.22
CCD matrix detector		
- Number of pixels (λ x spatial)		288 x 699
- Element size (λ x spatial) [μm]		16.8 x 9.2
- Size (λ x spatial) [mm]	H_λ x H_x	4.83 x 6.43
- Shortest working distance	WD	10.0 mm
Optical resolution		
- λ-axis [lp/mm]	R_λ	17
- Spatial axis [lp/mm]	R_x	2.5

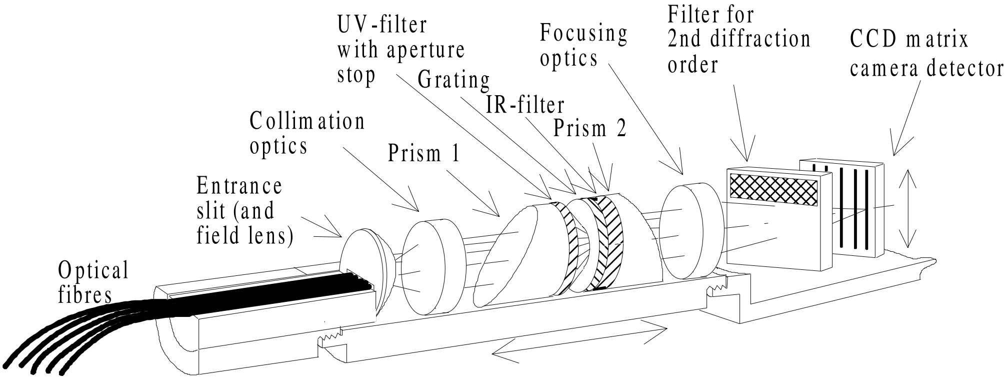

Figure 42. A CCD matrix camera and a specially designed imaging PGP spectrograph connected to N optical fibres to form a multipoint spectrograph.

5.1.2.2 Focal length and the line number of the grating

Once the wavelength range and dimensions of the detector are known, an approximate value for the grating frequency can be calculated from a simplified system consisting of the grating, only one prism, the focusing optics and the detector. In the present case Equation 2 is used to calculate the focal length as a function of the line number of the grating, $\nu(f)$. The length of the spectrum was prefered to be 4.7 mm. The ratio of the length of the spectrum and the detector gave value a = 0.973. The values mentioned above for λ_C, λ_L, a and H_λ were used and values between 10 mm and 60 mm were given for the focal length. The FOV was calculated using Equation 3. The results are shown in Figure 43. A focal length of 22.5 mm was chosen, because the FOV of the focusing optics was then ±10.2°. The grating frequency was chosen 420 l/mm, but after the design iteration 460 l/mm was selected.

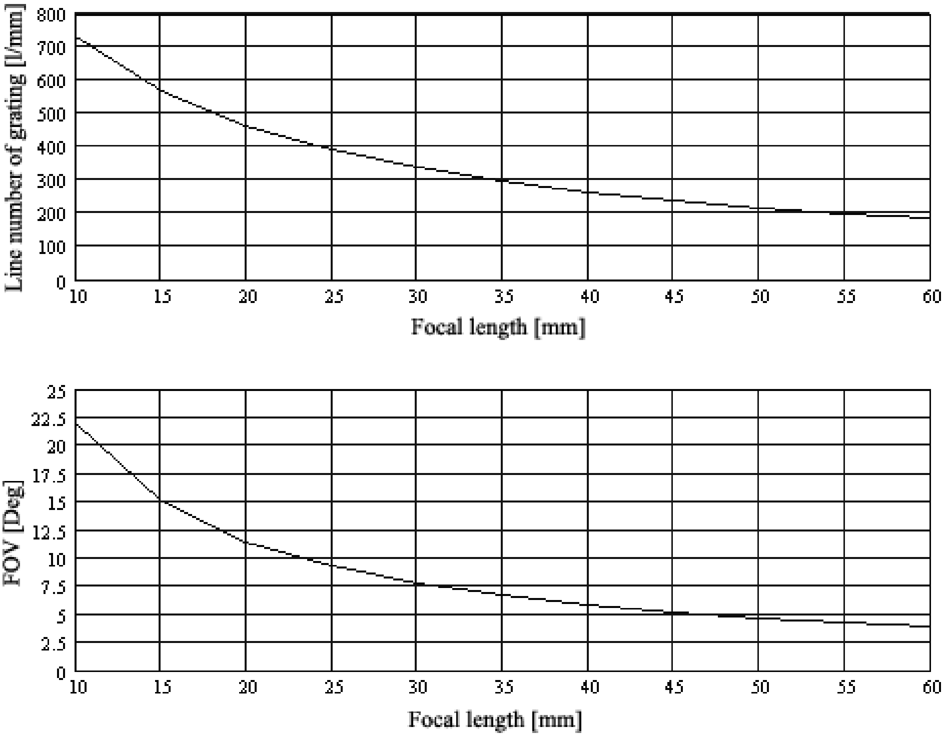

Figure 43. Line number of the grating and FOV of the focusing lens as a function of the focal length of the focusing lens.

5.1.2.3 PGP component design

In this case Bragg wavelength λ_B of 525 nm was chosen. The prisms for the visible wavelength range were made of FK5 (487704) because of the low dispersion of this material, Abbe-value is 70.41. The optimized parameters for the PGP are summarized in Table 6.

Table 6. Parameters of the PGP component.

Component	**Parameter**	**Symbol**	**Value**
First prism	- vertex angle	β_1	13.97°
	- top edge		2.36 mm
	- bottom edge		5.84 mm
	- central thickness		4.10 mm
	- material		FK5
	- diameter		14.0 mm
Second prism	- vertex angle	β_2	17.75°
	- top edge		1.00 mm
	- bottom edge		5.48 mm
	- central thickness		3.24 mm
	- material		FK5
	- diameter		14.0 mm
Grating	- line number	ν	460 l/mm
	- angle of incidence	θ_{1B}	4.648°.
	- Bragg wavelength	λ_B	525 nm
	- substrate thickness		1.00 mm
	- cover glass thickness		1.00 mm
	- diameter		20.0 mm
UV filter	- type		GG375
	- thickness		3.0 mm
	- diameter		14.0 mm
IR filter	- type		KG4
	- thickness		2.0 mm
	- diameter		14.0 mm

5.1.2.4 Simulated optical properties

The focusing and collimating lens systems were designed to be identical. The telecentric lens system consisted of four elements in two cemented doublets to reduce the number of air-glass interfaces to a minimum. A broad band antireflection coating was used on the lens surfaces and the measured average reflection from 400 nm to 800 nm was below 0.5 %.

The lens design was finalized by Prof. Wang MinQiang from Tsinghua University, Beijing, China. The optical construction of the PGP spectrograph is shown in Figure 44. The optics were symmetrical and 126 mm long. The aperture stop composed of an UV filter can be seen in the PGP component.

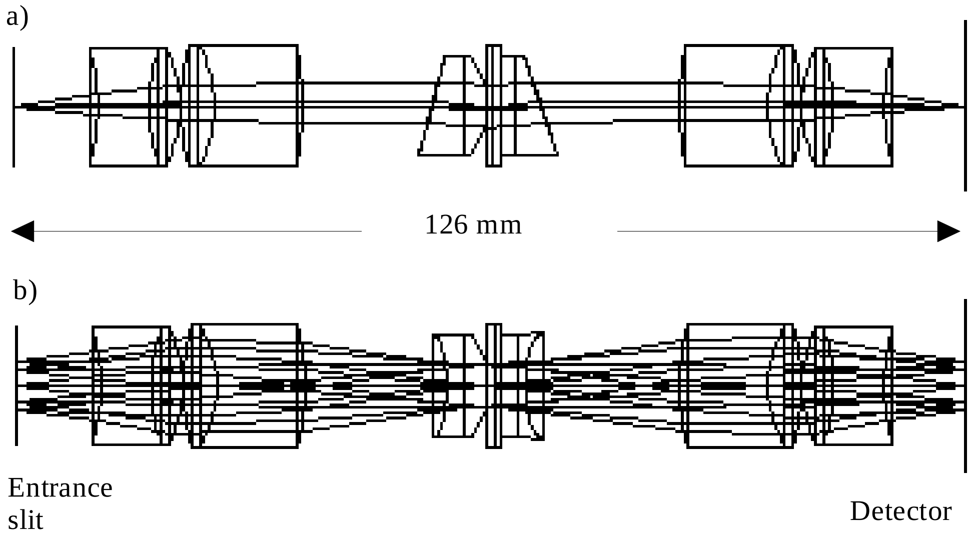

Figure 44. Designed optical construction of the PGP spectrograph seen from a) the spectral and b) the spatial direction.

An entrance slit was used, because when the fibres were disconnected and reconnected, the spectrograph should keep its spectral calibration. A 50 μm width of the slit gave the required spectral resolution of 5 nm. According to the simulations of the whole optics, the spectrum from 400 nm to 800 nm was 4.50 mm long at the detector. The total wavelength range seen by the ½” CCD matrix was 426 nm, and an optical resolution target of 17 lp/mm for the spectrograph was attained. The images of the slit formed by the wavelengths 400 nm, 600 nm and 800 nm on the surface of the detector are shown in Figure 45, where the bending of the spectral lines can be seen. When the average linear dispersion on the detector was 0.089 nm/μm, the maximum simulated bending, expressed using the unit of wavelength [nm], was 3.71 nm for 400 nm, 4.43 nm for 600 nm and 5.47 nm for 800 nm.

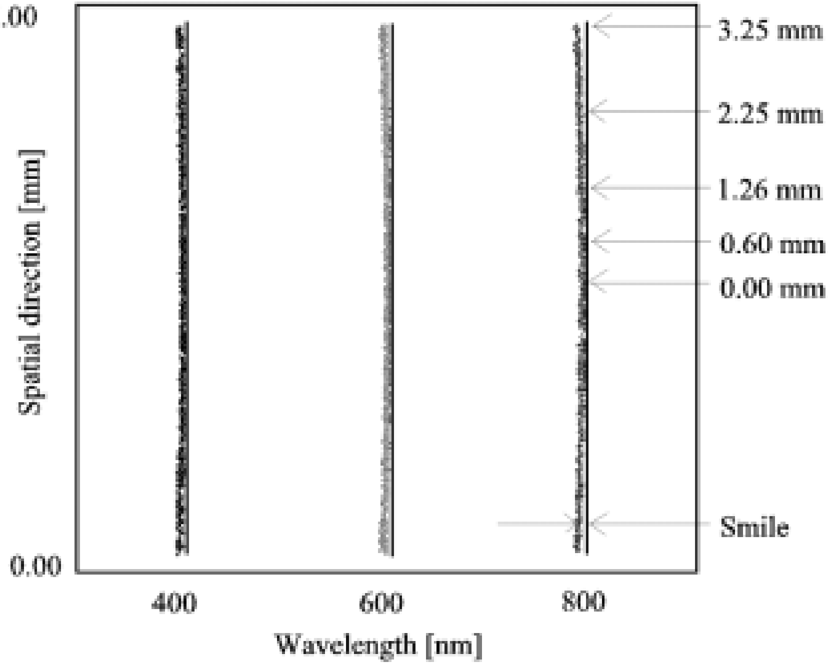

Figure 45. Simulated images of the slit formed by wavelengths of 400 nm, 600 nm and 800 nm on the surface of the detector, 7.00 mm x 7.00mm.

5.1.3 Optical measurements

The optics of the spectrometer were manufactured and installed into a set-up for measuring optical parameters, as shown in Figure 46. Optical fibres were not used in these measurements. The light sources were a halogen lamp, a HeNe-laser 632,8 nm and HgAr and Ne spectral lamps. A 200 µm slit with a diffuser was located on the focal plane of the collimating lens and Nikon f 50mm, f/1.4, and f 35mm, f/2, lenses were used as the collimating and focusing optics in the set-up. For stray light measurements a notch filter for 633 nm from Kaiser Optical Systems Inc. was used between the lenses. This had a 50% bandwidth of 18 nm and an O.D > 4.0. A cooled 2/3” CCD camera was used to measure the optical parameters. The pixel size of this camera was 23 µm x 27 µm and it had

375 pixels in the spectral direction and 242 in the spatial direction. The dimensions of the detector were 6.53 mm x 8.63 mm. For transmission measurement laser beams from HeCd 442 nm, HeNe 543.5 nm and HeNe 632.8 nm were directed through the spectrograph and the ingoing and outcoming intensities were measured.

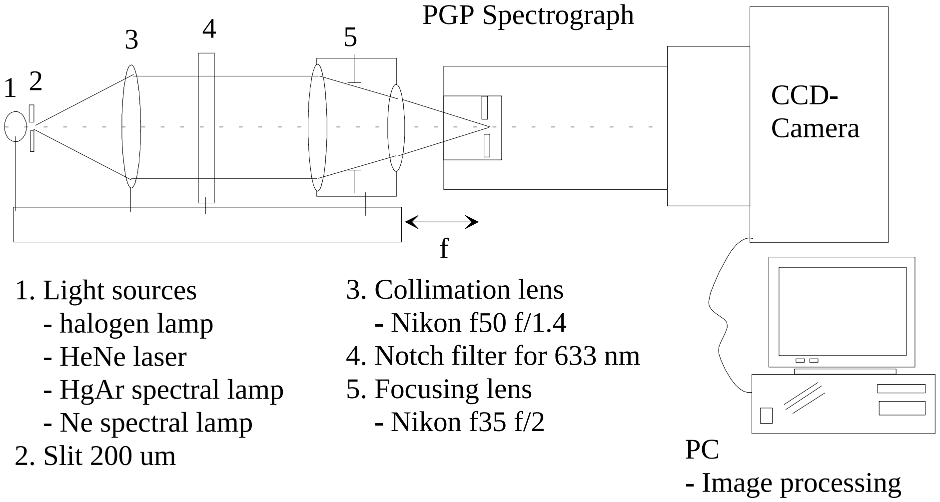

Figure 46. Set-up for measuring the optical properties of the PGP spectrograph.

The raw measured data from HgAr and Ne spectral lamps between detector pixels nos. 50 and 300 are shown in Figure 47, where the spectral peaks used in the analysis are also marked. As the pixel size of this camera was 23 μm and the final detector size will be 4.8 mm, only 209 pixels were used in the analysis of the optical properties. The range selected was from pixel no. 60 to 269.

The linear dispersion at the blue end of the spectrum was calculated using the Hg spectral peaks of 404.66 nm on pixel 71 and 435.87 nm on pixel 87, yielding a result of 1.95 nm/pixel. The dispersion for the NIR region was 2.42 nm/pixel using the Ne peaks of 724.5 nm on pixel 229 and 753.58 on pixel 242. Using these dispersion values, the wavelength range was calculated to lie between 383 nm (pixel 60) and 821 nm (pixel 269), covering 438 nm.

The spectral resolution can be seen in Figure 47b in the two neon peaks, 608.5 nm and 614.3 nm, which gave a wavelength separation of 5.8 nm and were clearly resolved. Even smaller separation, 3 nm, which existed between the 585.25 nm and 588.2 nm peaks, was below the spectral resolution in this arrangement and could not be resolved.

The bending of the spectral lines, smile distortion, can be seen in Figure 47a, where the pixel size was the same as the measured bending and the reading accuracy was 0.5 pixel. Plotting of the spectra from spatial lines 1, 121 and 242 in the same figure allows the bending to be estimated. This was between 1.5 and 2 pixels for the spectral peak of 404.66 nm, corresponding to values of 2.9–3.9 nm. The bending in the middle area of the spectrum, at 614.3 nm, was a little less than 2 pixels, and since the linear dispersion in that part of the spectrum was 2.2 nm/pixel, it corresponded to ≤ 4.4 nm. The bending for the 837.8 nm peak was just over 2 pixels but less than 2.5, which means between 4.8 nm and 6.0 nm.

The transmissions measured for the three laser beams mentioned above were T(442.0 nm) = 0.51, T(543.5 nm) = 0.47 and T(632.8 nm) = 0.52. The spectra measured for the notch filter at 633 nm illuminated by a broad-band light source and for a HeNe laser beam at 632.8 nm are shown in Figure 48. The dynamics of the cut-off wave band of the notch filter were more than 10^{-2} limited by the width of the spectral resolution. The straylight in the spectrum of the HeNe laser peak was very much smaller than 10^{-3} when measured farther than ±15 nm from the peak.

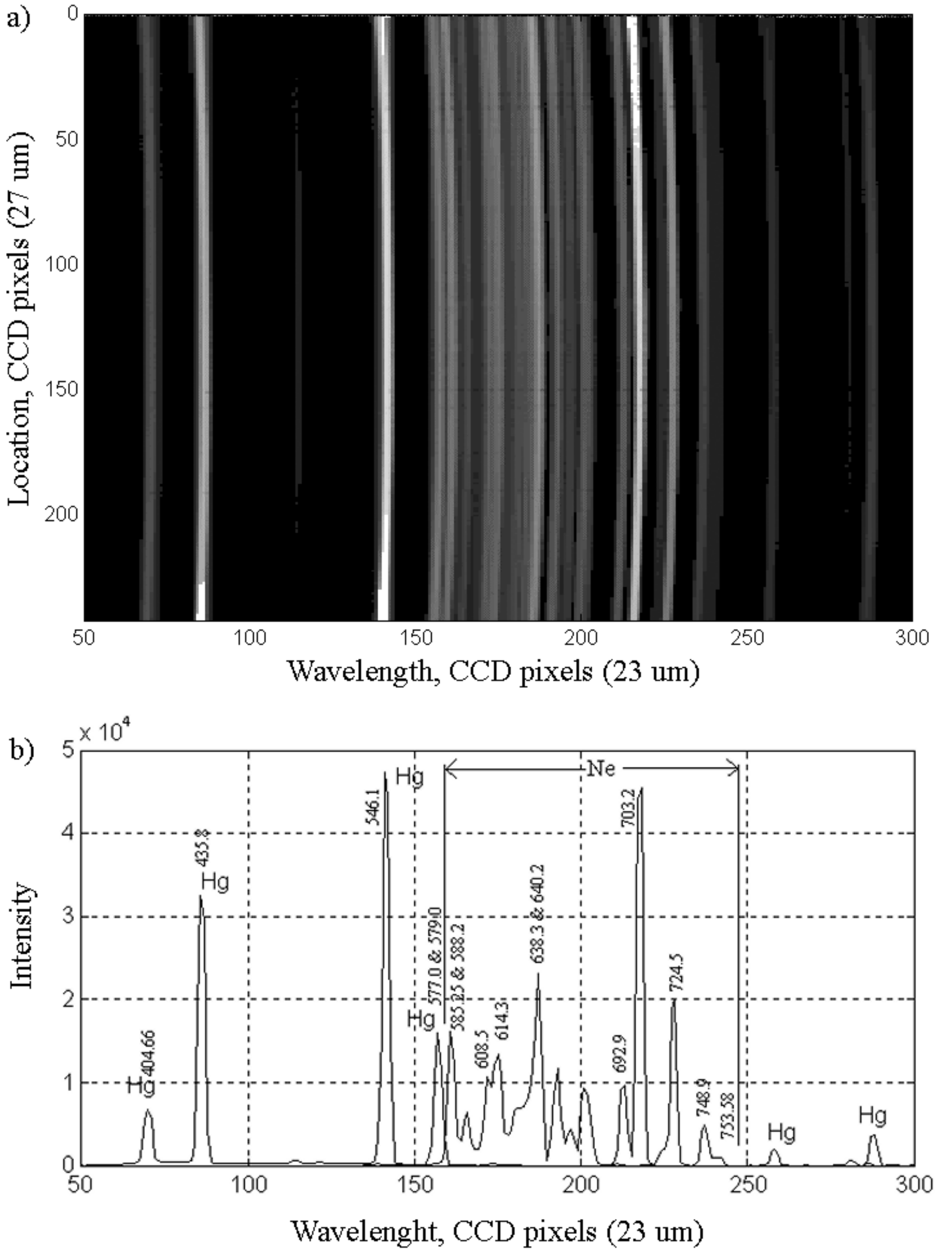

Figure 47. (a) Measured spectra of HgAr and Ne lamps. The spectral axis is shown horizontally and the spatial axis vertically. (b) Spectrum of spatial line 121. Some of the spectral peaks are marked on the spectrum.

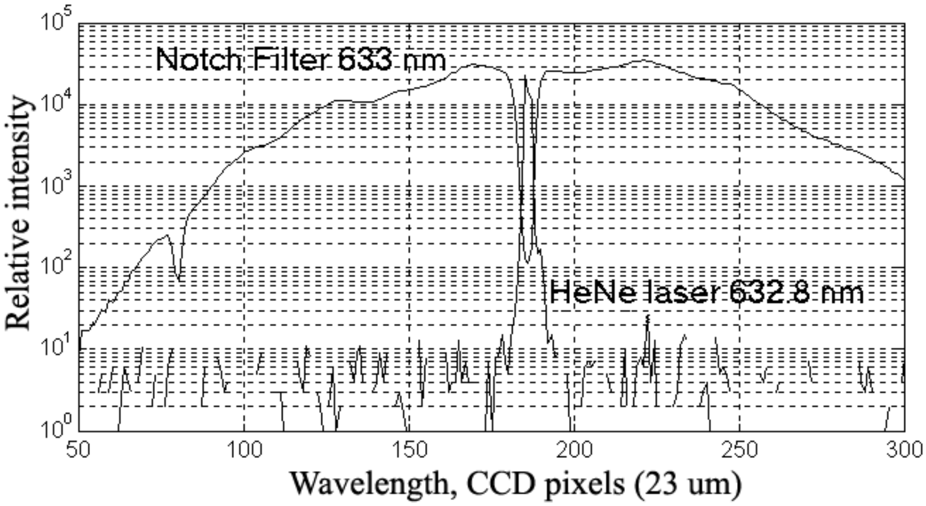

Figure 48. Spectra of a notch filter for 633 nm with a broad-band light source and a spectral peak of HeNe laser beam.

The simulated and measured optical properties are listed in Table 7. The measured wavelength range was 12 nm greater than the simulated range, corresponding to 5–6 pixels. The bending of the spectral lines was as simulated within the measuring accuracy, and the spectral resolution was as calculated, i.e. better than 6 nm. The transmission of the spectrograph was very high, but the stray light level was expected to be somewhat lower, although no comparisons were made with other instruments of the same kind.

Table 7. Simulated and measured optical properties of the PGP spectrograph.

Property	**Simulated**	**Measured**
Wavelength range	387–813 nm, Δ 426 nm	383–821 nm, Δ 438 nm
Bending of spectral lines, smile distortion	400 nm: 3.7nm 600 nm: 4.4 nm 800 nm: 5.7nm	404.6 nm: 2.9–3.9 nm 614.3 nm: < 4.4 nm 837.8 nm: 4.8–6.0 nm
Spectral resolution	5 nm	< 6 nm
Transmission	-	442.0 nm: 51 % 543.5 nm: 47 % 632.8 nm: 52 %
Stray light		632.8 nm: < 10^{-3}

5.1.4 Construction of the intelligent spectrometer

After the optical test measurements the optics were assembled into the designed intelligent spectrometer unit, which is shown in Figure 49. This had a 32 bit, 16 MHz processor with a 265 kByte program and 1 MByte image memory, and was connected to a PC for operation supervision and user interface via a RS-485/57.6 kBaud serial bus. When using this structure, only the useful wavelengths and channels that are of special interest are selected in the operating mode, to be converted into digital data. In this way the amount of data can be effectively reduced, which will benefit later data processing.

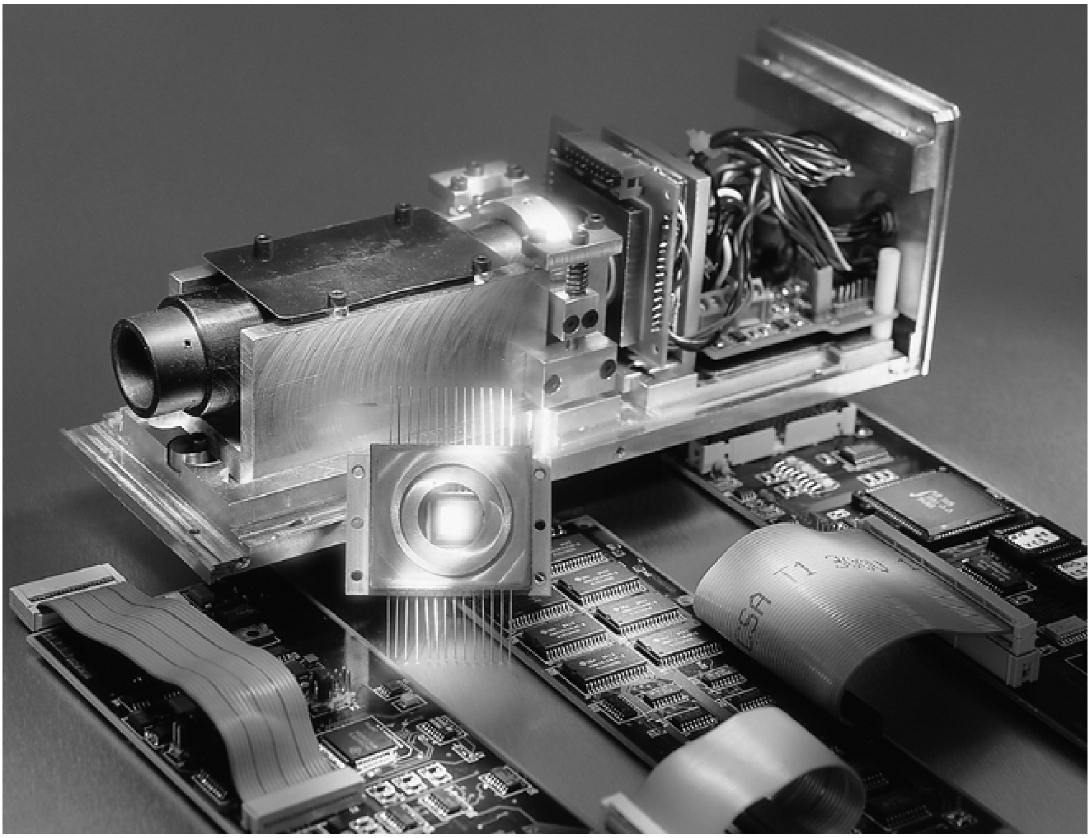

Figure 49. The intelligent spectrometer. A hermetically sealed CCD detector can be seen in the centre of the photo.

A hermetically sealed, temperature stabilized CCD detector can be seen in the centre of the photograph in Figure 49. The hermetic sealing between the window and the can was achieved using a specially developed glass-metal bond technique. The optical housing was capable of being filled with nitrogen gas if required. The three electronic boards were placed around the optics of the spectrometer. The case of the instrument fulfils the IP54 tightness requirements and is suitable for a harsh environment. The dimensions were small: 25 cm x 9 cm x 9 cm. The main features of the intelligent spectrometer are summarized in Table 8.

Table 8. Features of the intelligent spectrometer.

Feature	**Value(s)**
Detector	1/2” CCD, 735x288 pixels
Detector package	Hermetically sealed, peltier temperature stabilisation
Integration/Exposure time	3–60 000 ms
Processor	32 bit, 16 MHz
Image memory	1 MByte
Program memory	256 kByte
A-D Conversion	12 bit, 3 units
Communications	RS-485/57.6 kBaud Serial bus, 2 units
Case class	IP54

The measured raw data for 16 fibre optic channels can be seen as an example in Figure 50. The data were measured using the intelligent PGP spectrograph unit installed in an application test set-up. The light source was a white fluorescent lamp, the spectrum of which had a few spectral peaks and broad-band background emission. All the channels in these figures represent the reflection from a sheet of white paper. The fibres were 200 μm in active diameter and the pitch was 330 μm. The optical isolation between neighbouring channels was 10^{-2}. The positioning error of the fibres on the optical measuring head did not cause any problems because the location of each channel could be programmed into the intelligent PGP spectrograph. As compared with the measurements presented above, the detector has 735 x 288 pixels of 9.2 μm x 16.8 μm.

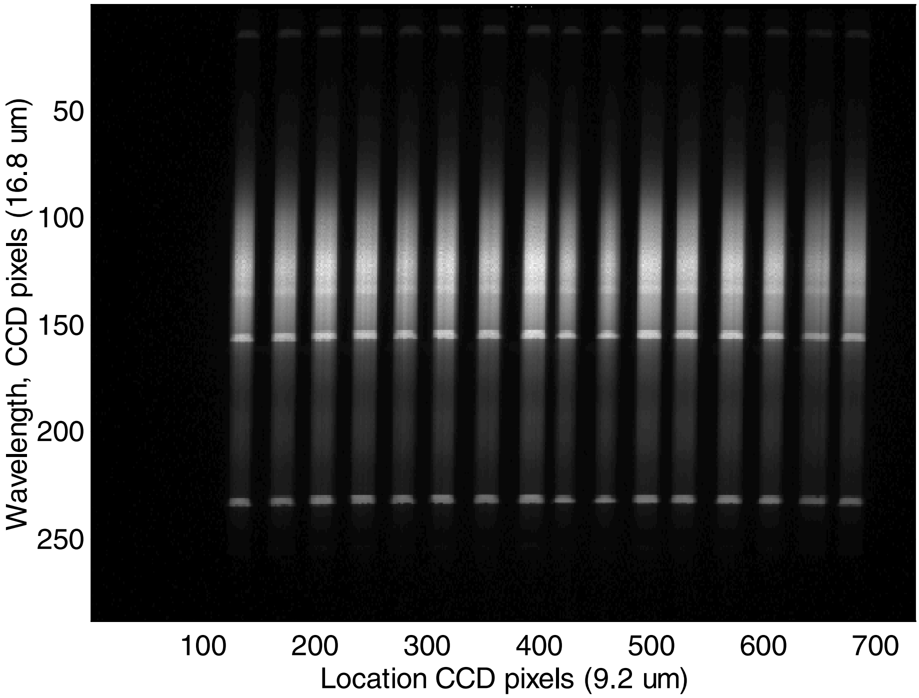

Figure 50. Measured raw data for 16 fibre optic channels. The spectral line on pixel row 240 is 435.87 nm for Hg.

5.1.5 System for oil film thickness measurement

This section is based on the paper of Vaarala et al. (1997).

Protective oils are used in cold rolling steel and aluminium mills. The surface is coated with a thin layer of oil in order to repel corrosion during storage and transportation. Also when manufacturing goods in pressforming lines the correct thickness of the oil layer is critical to the quality of forming. Thus there is a need for an on-line oil film thickness meter to supply feedback to the oiling machine.

The key requirements for an oil meter are ruggedness, reliability, ease of use and flexibility. Flexibility in this context symbolises the ability to conform to any change in production without a glitch. E.g., the protection oil and substrate may change, resulting in changes in the fluorescence spectrum, which means that the instrument has to be recalibrated, or better still, it can detect the changes and performs the recalibration automatically. In addition, the light source and optical transfer function of the instrument can be included in the measurement data. This enables us to use spectrally unstable light sources, because the instrument records the momentary spectra and is able to compensate for any variation in the source. In addition, it can be used to track the effects of dirt and ageing. The PGP spectrograph in combination with an intelligent camera can provide a solution to this.

A prototype version of an oil meter station was produced for evaluation purposes. The basic set-up is presented in Figure 51. This unit consisted of a special light source, a fibre optic bundle for light collection, the intelligent PGP spectrograph and a computer with control and analysis software.

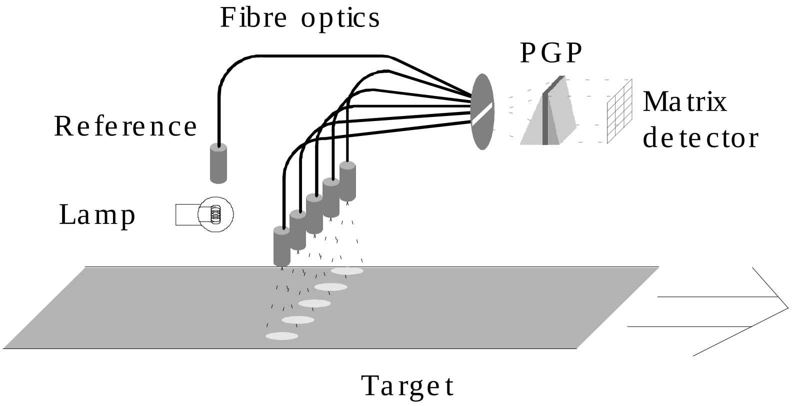

Figure 51 The measurement set-up for multipoint on-line oil and colour measurement.

The spectrograph was programmed to measure the spectra of 10 fibres with $\Delta\lambda$ = 40 nm with an exposure time of 1 s. The accuracy achieved is of the order of ±0.3 g/m² with an oil quantity in the range 0–5 g/m². A complete prototype and application environment evaluation revealed the potential for up to a 10-fold increase in performance. To be accepted for on-line use, at least one third of this potential would have to be realised.

5.2 PGP spectrograph for the interrogation of large scale fibre optic Bragg grating arrays

5.2.1 Introduction

Fibre Bragg Gratings (FBG) are among the most promising types of fibre optic sensors for many applications. The response of these sensors is a wavelength-dependent signal when sensors are applied, for example, to strain, which means a material fractional increase in physical length when stressed, $\varepsilon = \Delta l/l$. Figure 52 shows a diagram of a fibre grating reflector and the Bragg condition for reflection, in which the grating reflects the wavelength, which is twice the optical grating spacing (Dakin and Culshaw 1997).

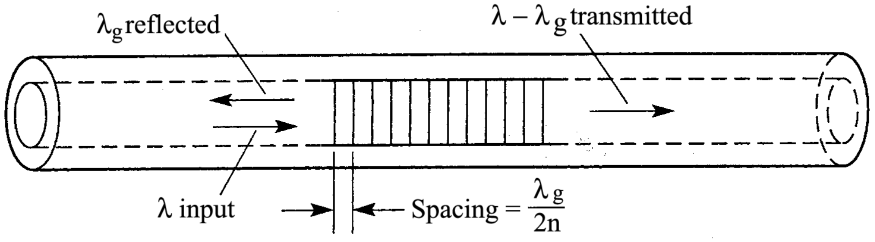

Figure 52. Diagram of Fiber Bragg Grating and the Bragg condition for reflection (Dakin and Culshaw 1997, p. 263).

The strain sensitivity of the FBG results primarily from the change in grating spacing when the fiber is stretched. However, a change in the axially polarized refractive index, caused by the stretching, also results from the photoelastic effect. The change in Bragg wavelength per unit wavelength is typically 74% of the strain, that is

Equation 15 $$\delta\lambda/\lambda = 0.74\ \Delta l / l = 0.74\ \varepsilon.$$

The width of the reflected Bragg wavelength range is typically 0.2 nm (Dakin and Culshaw 1997).

When using Bragg gratings for monitoring large structures, a network consisting of tens of point sensors is usually needed for good coverage of the structure. In these cases a wavelength multiplexed network interrogation device is needed in practical applications. There is a commercial instrument available for producing a serial Bragg grating network of a few sensors in a single optical fibre. Chen et al. (1997) published a digital spatial domain multiplexing method that involves the measuring of several wavelength channels from a fibre network.

5.2.2 System overview

The idea of an imaging PGP spectrograph-based method for wavelength multiplexed sensor network interrogation was presented at the 12th Optical Fiber Sensors conference, OFS-12, by Aikio et al. (1997). This aroused interest in developing a PGP spectrograph for the purpose. The resulting optical system capable of monitoring 50 optical fibers, each with 14 FBGs (700 sensors), was introduced at OFS-14 by Aikio et al. (2000). Christiansen et al. (2000) presented a demonstration of this first high-speed (1.9 kHz sample rate) interrogation system for large-scale fiber optic Bragg grating arrays.

The principle of the interrogation device is shown in Figure 53. The test system consisted of up to 25 optical fibres, each with multiple Bragg gratings, a PGP spectrograph, a CMOS detector and a computer for data acquisition and processing. The optical source was a superluminescent diode with a spectrum FWHM of 70 nm centred around 820 nm. The wavelength range of the spectrograph was 70 nm between 780 nm and 850 nm with a linear dispersion of 0.14 nm/pixel.

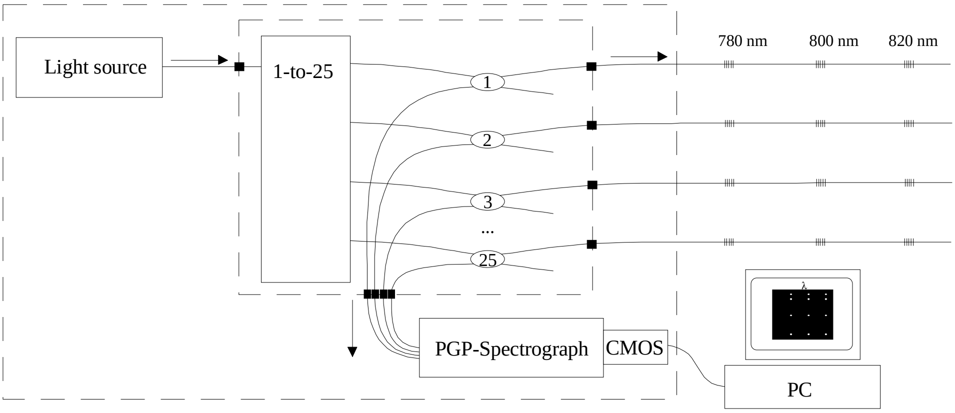

Figure 53. An interrogation device for a fiber optic Bragg grating sensor network, based on an imaging PGP spectrograph (Aikio et al. 2000).

5.2.3 Optical design and simulations of the PGP spectrograph

The selected CMOS detector size was 6 × 6 mm² with 512 × 512 elements and a pixel size of 12 × 12 µm². The PGP spectrograph design, with a wavelength range of 780–850 nm, is shown in Figure 54. In order to achieve high enough linear dispersion in the detector, 0.14 nm/pixel, and to keep the PGP component constructable, the following combination of focal length, grating frequency and prism angles was chosen. The triplet was designed for the NIR wavelength range with a focal length of 75 mm, the grating frequency was 963 l/mm, the vertex angle of the first prism was 40.8° and that of the second prism 38.6° and the prism material was BK7. No filters were needed in this application.

Simulated spots for three FBGs, 790 nm, 815 nm and 840 nm, in the on-axis and three off-axis channels are shown in Figure 55. The energy clearly peaked in the centres of the spots, even in the worst case, which enabled high-accuracy spectral measurement. The precise central position of each spot can be enhanced to sub-pixel level by calculating the centroid of each peak (Chen et al. 1997).

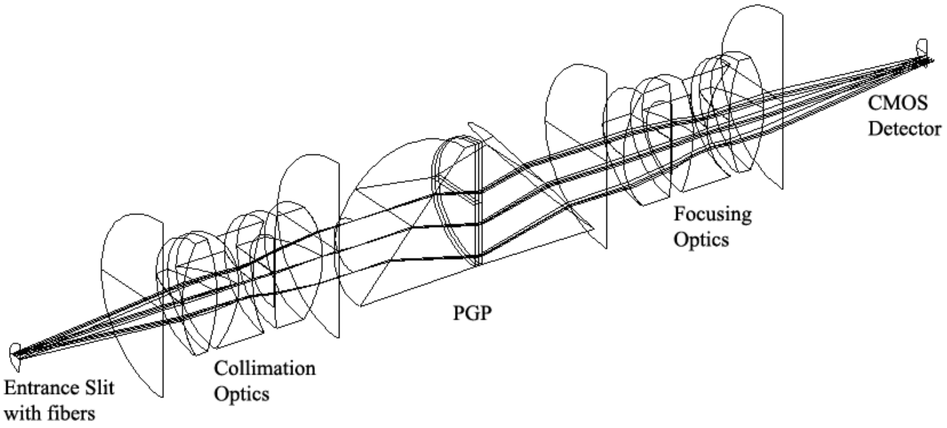

Figure 54. The PGP spectrograph with a ray tracing of 815 nm.

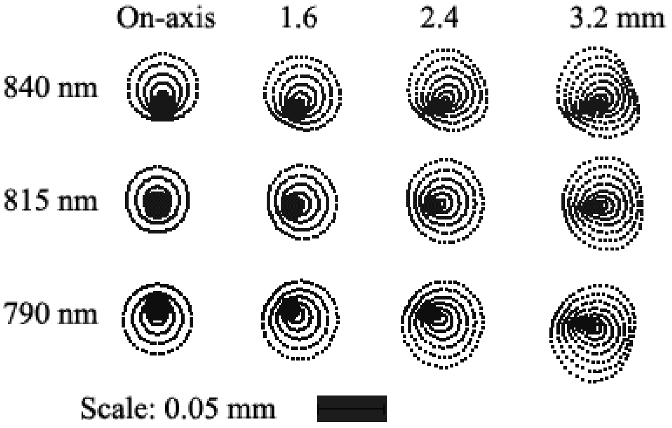

Figure 55. Simulated spot sizes for three FBG wavelengths in the on-axis and three off-axis channels.

The length of the spectrum, from 780 nm to 850 nm was 5.99 mm covering 512 pixels on the detector. A simulated 0.5 nm spectral shift from 815.0 nm to 815.5 nm launched from two fibres with a 10 μm core diameter and 130 μm pitch is shown in Figure 56. The separation of the grid lines in the graph is 8 μm and the distance between the tops of the spectral peaks, taken from the simulation data, is 43 μm on the detector, corresponding to 3.6 pixels. The linear dispersion is then 0.14 nm/pixel, which corresponds to 230 με/pixel at a wavelength of

800 nm. The simulated spot sizes were between 50 μm and 100 μm, e.g. 4–8.5 pixels.

According to the simulations, up to 50 fibres can be inserted into the input slit of the PGP spectrograph when the core diameter of the fibres is 10 μm and the centre-to-centre distance between neighbouring fibres is 120 μm.

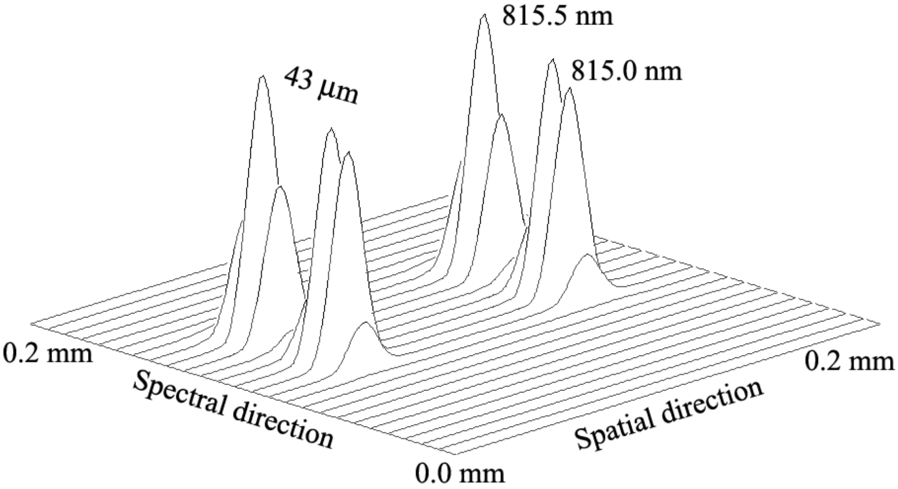

Figure 56. Simulated 0.5 nm spectral shift from 815.0 nm to 815.5 nm in fibres with a 10 μm core diameter and 130 μm spacing. The shift of the top is 43μm, corresponding to a linear dispersion of 0.012 nm/μm (=0.14nm/pixel).

5.2.4 Measurements

The measurements and calculations presented in this section were performed mainly by Pekka Suopajärvi, Research Scientist at VTT Electronics, and were published by Aikio et al. (2000), the paper which this discussion is based on.

The measured spectral width of the spectrograph was 73 nm, from 778 nm to 851 nm, so that the linear dispersion was as simulated, 0.14 nm/pixel, which corresponds to 230 με/pixel at a wavelength of 800 nm.

The resolution of the measurement system was determined in a load test in which a single optical fiber with a 800 nm Bragg grating was loaded in pure tension using small weights. Complete cycles of loading and unloading were performed and the spot positions on the CMOS pixel row were measured. The precise central position of each FBG peak was enhanced to sub-pixel level by calculating the centroid of each peak. The width of 19 pixels (see Figure 57) were used to calculate the centroid within the accuracy better than 0.02 pixels. The strain accuracy, measured by calculating the standard deviation of the measurement points, was 3.8 με. If strain in 1 m length object is measured, the accuracy is 3.8 μm. If only the length of a Bragg grating, f.ex. 10 mm, is used for the measurement, 38 nm local accuracy is achieved. The results of loading and unloading the FBG are presented in Figure 58.

The shape of the spot is elliptical, which can be seen in Figure 57, indicating that the realized PGP spectrograph has larger aberration in the wavelength direction than in the spatial direction contrary to simulations shown in Figure 55 and Figure 56. Spot profiles and spot images without a PGP component and with two different PGP components composed of gratings from two different batches of gratings ("new" and "old") can be seen in Figure 59. The pure lens system produced a spot size of 7 x 7 pixels. The optical quality of the gratings from different batches varied and were not high enough. The measured spot sizes ranged from 8 x 12 to 10 x 19 pixels. Christiansen et al. (2000) estimated the noise level of the imager from the intensity profiles of the spots to be approximately 8%, which is higher than typically for PGP spectrographs (see Figure 48).

If the desired strain range is 2000 με corresponding wavelength shift of 9 pixels and the spot size is 19 pixels, each FBG will require 32 pixels in the spectral direction including 2 pixels on both sides of the spot. Therefore, a single fiber channel will be capable of accommodating 14 FBGs. The maximum image width of each fibre in the spatial direction was 10 pixels and the distance between two adjacent fibers was 20 pixels, which corresponds to 240 μm. This means that the number of fibers in the input slit could be increased from 25 to 50 without interference between the fiber channels. This is clearly visible in the spot image (Figure 57) where the space between two adjacent spots is wider than the spots themselves. If up to 50 fibres can be inserted in the input slit of the

PGP spectrograph and each fibre has 14 FBGs, up to 700 FBGs can be interrogated simultaneously.

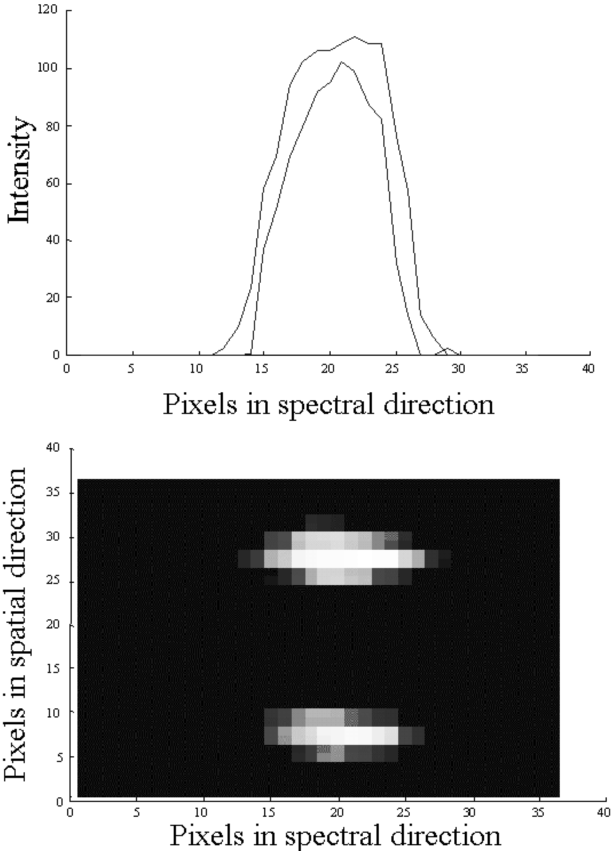

Figure 57. Spot profile and spot image from a CMOS detector when two FBGs with the same central wavelength are connected in adjacent fibres, the spot size is 10 x 19 pixels (Aikio et al. 2000).

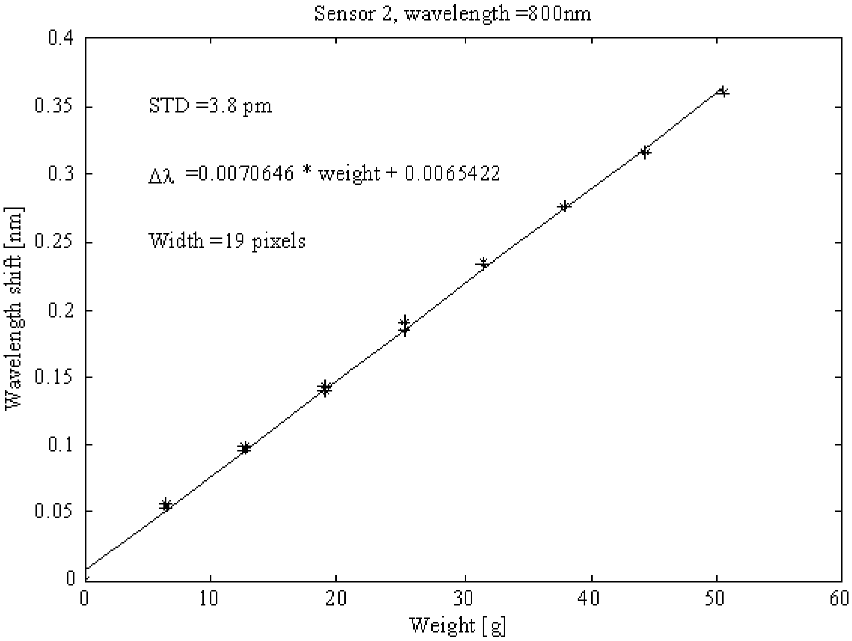

Figure 58. Wavelength change in a Bragg grating when loading and unloading the fibre (Aikio et al. 2000).

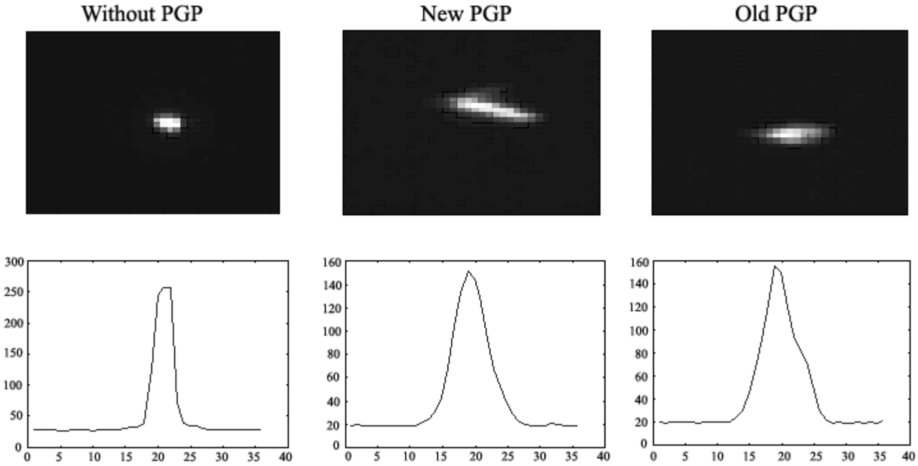

Figure 59. Spot profiles and spot images: without any PGP component and with two PGP components composed of gratings from two different batches of gratings ("new" and "old").

6 Summary

A new type of direct vision dispersing component, the prism-grating-prism (PGP) concept was invented by the author in 1991. This patented PGP component allows small, low-cost hyperspectral imaging spectrograph constructions (Figure 60) suitable for industrial and research applications. It can be used in the wavelength range from 320 nm to 2700 nm, limited by the transmission of the grating material.

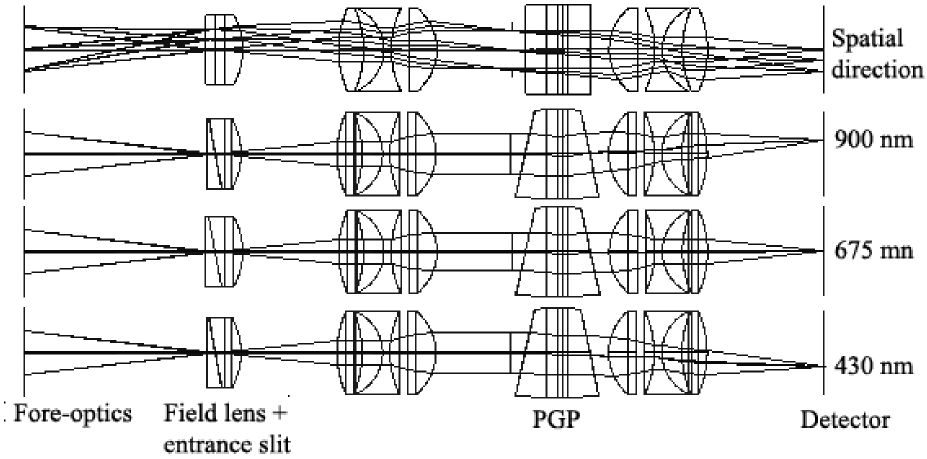

Figure 60. Optical principle of the small PGP spectrograph.

The PGP spectrograph has the following properties:

- The direct-vision PGP provides a large, linear dispersion, by virtue of the diffraction grating, as compared with a direct vision prism with small, non-linear dispersion.
- The direct-vision PGP can be modified for different wavelength ranges by changing the grating period and the vertex angles and materials of the two prisms, contrary to the very limited grism construction.
- The PGP has a high diffraction efficiency (up to 70%) and a practically polarization-independent throughput, because of its volume phase transmission holographic grating.

- The direct-vision property of the PGP allows stable, small tubular optomechanics in the spectrograph (e.g. diam. 30 mm x length 110 mm with f/2.8 for a 2/3" detector).
- The same tubular optomechanics can be used with different PGP components designed for different wavelength ranges.

This thesis introduces the PGP component and the spectrograph optics based on it and describes the PGP design procedure. The potential of the PGP construction is demonstrated by presenting the following four hyperspectral imaging PGP spectrographs in detail.

1) The prototype for an airborne hyperspectral imaging spectrograph AISA, designed in 1992, covering the wavelength range 430–900 nm with a spectral resolution of 1.6 nm/pixel. The spatial resolution was 1 m x 1 m with 360 pixels per swath using an aircraft flying 1000 metres above the ground at 50 m/s. AISA is the smallest commercial airborne imaging spectrometer system currently available.

2) The microscope imaging UV-VIS-NIR spectrometer system, developed in 1992–1993 for the spectral measurement of micrometer-sized objects such as wood fibres by means of transmitted light over a broad wavelength range from 250 nm to 975 nm. The range was divided between three imaging spectrographs by two dichroic plates: UV from 250 nm to 450 nm, VIS from 400 to 700 nm and NIR from 700 to 975 nm. The instrument can measure objects up to 900 μm x 27 mm with a spatial resolution better than 5 μm x 5 μm and a spectral resolution of 5 nm.

3) A telecentric PGP spectrograph connected with optical fibre probes, designed for industrial applications in 1994–1995. The wavelength range from 400 nm to 800 nm and the spectral resolution of 5 nm are reasonable for many process control applications and colour measurements. The small design (length 126 mm x diameter 30 mm) incorporates a highly advanced PGP component consisting of long and short bandpass filters, the aperture stop for the whole optics, two prisms and the grating. One fibre optic channel is used as a light source reference and 15 channels for object point remote sensing. The system has been used for on-line oil film thickness measurements.

4) The latest PGP spectrograph design, from 1999, for the first high-speed interrogation system for large-scale fibre optic Bragg grating arrays. The measured spectral width of the spectrograph was 73 nm, from 778 nm to 851 nm, with a linear dispersion of 0.14 nm/pixel. This design has the largest dispersion of any PGP component ever made, and therefore the largest prism angle, 40°. The system can interrogate up to 700 Bragg gratings simultaneously with a sample rate of 1.9 kHz.

The measured properties of the spectrographs are summarized in Table 9.

Table 9. Measured properties of the hyperspectral imaging PGP spectrographs presented in this work.

	Spectral range [nm]	**Spectral resolution**	**Spatial resolution**
AISA	430–900	1.6 nm/pixel	1m / FOV 384 m
Microscope imaging spectrom.	UV*: 251–458 VIS: 390–693 NIR: 672–976	< 5nm < 5nm < 5nm	4 µm / FOV 0.9 mm 4 µm / FOV 1.4 mm 4 µm / FOV 1.4 mm
Multi point	383–821	< 6 nm	16 fibers/entrance slit
Bragg	778–851	0.14nm/pixel	50 fibers/entrance slit

(* Offner spectrograph)

The author's contributions to these spectrograph systems were the invention of the PGP component, the design of the PGP components and the spectrograph optics, the lay-out of the mechanical design and the assembly and alignment of the opto-mechanical system including test measurements.

The PGP concept and the results of the development work that commenced in 1991, as reported in this thesis, were so promising that a company was founded in 1995 to commercialize, further develop and manufacture PGP spectrograph technology under licence from VTT Electronics. Its products include the many versions of the small, low-cost imaging spectrograph ImSpector™ and also the smallest commercial airborne imaging spectrometer system, AISA.

PGP spectrographs are nowadays used world-wide for industrial machine vision and spectral analysis, airborne remote sensing and scientific applications, in the form of both standard products and customized OEM components.

References

Aikio, M. 1992. Optinen komponentti (An optical component), Finnish Patent Application N:o 921564, April 8th, 1992; Finnish Patent N:o 90289 accepted January 10th, 1994.

Aikio, M. 1997a. Componente ottico comprendente prismi ed un reticolo, Italian Patent N:o EP/IT 0 635 138.

Aikio, M. 1997b. Optical component comprising prisms and a grating, English Patent N:o EP/GB 0 635 138.

Aikio, M. 1997c. Optisk komponent innefattande prismor och ett gitter, Swedish Patent N:o EP/SE 0 635 138.

Aikio, M. 1997d. Optisches Element mit Prismen und einem Beugungsgitter, German Patent N:o EP/DE 0 635 138.

Aikio, M. 1997e. French Patent N:o EP/FR 0 635 138.

Aikio, M. 2000. Optical component comprising prisms and a grating, Canadian Patent Application N:o CA 2117907.

Aikio, M., Vaarala, T. and Keränen, H. 1997. Intelligent prism-grating-prism spectrograph for multipoint fibre optic remote spectroscopy, OSA Technical Digest Series, Vol. 16, pp. 552–555.

Aikio, M., Suopajärvi, P., Chen, S., Vaithyanathan, K., Christiansen, M., Chen, P. and Kopola, H. 2000. PGP spectrometer for fibre optic Bragg grating sensor network interrogation, Proc SPIE, Vol. 4185, pp. 568–571.

Arns, J.A, Colburn, W.S. and Barden, S.C. 1999. Volume phase gratings for spectroscopy, ultrafast laser compressors, and wavelength division multiplexing, Proc SPIE, Vol. 3779, pp. 313–324.

Barden, S.C., Arns, J.A., Colburn, W.S. and Williams, J.B. 2000. Volume-Phase Holographic Gratings and the Efficiency of Three Simple VPH Gratings, Publications of the Astronomical Society of the Pacific, Vol. 112, Issue 771, June, pp. 809–820.

Battey, D.E. and Slater, J.B. 1993. Compact holographic imaging spectrograph for process control applications, Proc SPIE, Vol. 2069, pp. 60–64.

Battey, D.E., Slater, J.B., Wludyka, R., Owen, H., Pallister, D.M. and Morris, M.D. 1993. Axial transmissive f/1.8 imaging Raman spectrograph with volume-phase holographic filter and grating, Appl. Spectroscopy, Vol. 47(9), pp. 1913–1919.

Borregaard, T. 1997. Application of imaging spectroscopy and multivariate methods in crop-weed discrimination, *Doctoral Thesis*, The Royal Veterinary and Agricultural University, Taastrup, Denmark.

Braam, B., Okkonen, J., **Aikio, M**., Mäkisara, K. and Bolton, J. 1993a. Design and first test results of the Finnish Airborne Imaging Spectrometer for Different Applications, AISA, Proc SPIE, Vol. 1937, pp. 142–151.

Braam, B., Okkonen, J., **Aikio, M**., Mäkisara, K. and Bolton, J. 1993b. AISA, an Airborne Imaging Spectrometer for Different Applications: its operational potential, *Presented at the International Symposium Operationalization of Remote Sensing*, 19–23 April 1993, ITC Enschede, The Netherlands**.**

Burns, R., La Baw, C. and Duval, V. 1993. Lunar Scout Infrared Detector (LSIRD): simple low-cost imaging spectrometer, Proc SPIE, Vol. 1874, pp. 164–175.

Carter, M.R., Bennett, C.L., Fields, D.J. and Lee, F.D. 1995. Livermore Imaging Fourier Transform Infrared Spectrometer (LIFTIRS), Proc SPIE, Vol. 2480, pp. 380–386.

Chang, B.J. and Leonard, D.C. 1979. Dichromated gelatin for the fabrication of holographic optical elements, Applied Optics Vol. 18, No. 14, pp. 2407–2417.

Chen, S., Hu, Y., Zhang, L. and Bennion, I. 1997. Digital Spatial and Wavelength Domain Multiplexing of Fiber Bragg Grating Based Sensors, *OSA Technical Digest Series*, Vol. 16, pp. 448–451.

Christiansen, M., Vaithyanathan, K., Chen, P., Kopola, H., **Aikio, M.**, Suopajärvi, P. and Chen, S. 2000. High Speed Interrogation of Large Scale Fiber Optic Bragg Grating Arrays, Proc SPIE, Vol. 4185, pp. 256–259.

Cutter, M.A., Lobb, D.R., Williams, T.L. and Renton, R.E. 1999. Integration & Testing of the Compact High-Resolution Imaging Spectrometer (CHRIS), Proc SPIE, Vol. 3753, pp.180–191.

Dakin, J. and Culshaw, B. 1997. Optical Fiber Sensors, Vol. 4, Applications, Analysis and Future Trends, Artec House Inc.

Davis, O.C., Kappus, M., Bowles, J., Fisher, J., Antoniades, J. and Carney, M. 1999. Calibration, characterization and first results with the Ocean PHILLS Hyperspectral Imager, Proc. SPIE, Vol. 3753, pp. 160–167.

Descour, M.R. and Dereniak, E.L. 1995a. Nonscanning no-moving-parts imaging spectrometer, Proc of the SPIE, Vol. 2480, pp. 48–64.

Descour, M.R. and Dereniak, E.L. 1995b. Computed-tomography imaging spectrometer: experimental camibration and reconstruction results, Applied Optics, Vol. 34, No. 22; pp. 4817–4826.

Descour, M.R. and Shen, S.S. 2000. Imaging Spectrometry VI, Proceedings of the Conference on Imaging Spectrometry VI, Proc SPIE, Vol. 4132.

Fisher, J., Baumback, M., Bowles, J., Grossmann, J. and Antoniades, J. 1998. Comparision of low-cost hyperspectral sensors, Proc SPIE, Vol. 3438, pp. 23–30.

Ford, B.K., Volin, C.E., Murphy, S.M., Lynch, R.M. and Descour, M.R. 2001. Computed Tomography-Based Spectral Imaging For Fluorescence Microscopy, Biophysical Journal, Vol. 80, pp. 986–993.

George, N. and Matthews, J.W. 1966. Holographic diffraction gratings, Applied Physics Letters, Vol. 9, No. 5, pp. 212–215.

Green, R.O., Eastwood, M.L., Sarture, C.M., Chrien, T.G., Aronsson, M., Chippendale, B.J., Faust, J.A., Pavri, B.E., Chovit, C.J., Solis, M., Olah, M.R. and Williams, O. 1998. Imaging spectroscopy and the Airborne Visible/Infrared Imaging Spectrometer (AVIRIS), Remote-Sensing-of-Environment. Vol. 65, No.3, Sept., pp. 227–248.

Goetz, A.F.H. 1995. Imaging spectrometry for remote sensing: Vision to reality in 15 years, Proc SPIE, Vol. 2480, pp. 2–13.

Hagman, O. 1996. On reflections of Wood, Wood quality features modelling by means of multivariate image projections to latent structures in multispectra images, *Doctoral Thesis*, Luleå Univ. of Tech.

Hariharan, P. 1996. Optical holography: principles, techniques and applications, Cambridge University Press, 406.

Herrala, E., Okkonen, J., Hyvärinen, T., **Aikio, M**. and Lammasniemi, J. 1994. Imaging spectrometer for process industry applications, Proc. SPIE, Vol. 2248, pp. 33–40.

Herrala, E. and Okkonen, J. 1996. Imaging spectrograph and camera solutions for industrial applications, Int. J. of Pattern Recognition and Artificial Intelligence, Vol. 10, pp. 43–54.

Hutley, M.C. 1990. Diffraction gratings, Academic Press Inc.

Hyvärinen, T., Herrala, E. and Dall'Ava, A. 1998. Direct sight imaging spectrograph: a unique add-on component brings spectral imaging to industrial applications, SPIE symposium on Electronic Imaging, Proc SPIE, Vol. 3302.

Jet Propulsion Laboratory, California Institute of Technology, Pasadena California. 2001. Website of AVIRIS spectrometer:
http://makalu.jpl.nasa.gov/aviris.html

Johansson, T. and Pettersson, A. 1997. Imaging spectrometer for ultraviolet – near-infrared microspectroscopy, Rev. Sci. Instrum., Vol. 68(5), pp. 1962–1971.

KOSI, Kaiser Optical Systems Inc. 2001. Website
http://www.kosi.com/raman/products/holospec.html

Korsch, D. 1991. Reflective optics, Academic Press Inc.

Kutser, T., Hannonen, T., Kallio, K., Koponen, K., Pulliainen, J., Pyhalahti, T. and Servomaa, H. 1998. Monitoring of turbid coastal and inland waters by airborne imaging spectrometer AISA, Geoscience and Remote Sensing Symposium Proceedings, IGARSS '98. IEEE International Volume 5, pp. 2597–2599.

Kwo, D., Lawrence, G. and Chrisp, M. 1987. Design of a grating spectrometer from a 1:1 Offner mirror system, Proc SPIE, Vol. 818, pp. 275–279.

Laan, E., de Vries, J., Kruizinga, B., Visser, H., Levelt, P., van de Oord, G., H., J., Maelkki, A., Leppelmeier, G. and Hilsenrath, E. 2000. Ozone monitoring with the OMI instrument, Proc SPIE, Vol. 4132, pp. 334–343.

Labandibar, J-Y., Jubineau, F., Silvestrin, P. and Del Bello, U. 1999. The ESA Earth Explorer Land Surface Processes and Interactions Mission, Proc SPIE, Vol. 3753, pp. 12–23.

Lobb, D.R. 1998. Imaging Spectrometer, PCT patent, International publication number: WO 98/37389.

Loewen, E.G. and Popov, E. 1997. Diffraction gratings and applications, Marcel Dekker Inc.

Mao, C., Seal, M. and Heitschmidt, G. 1997. Airborne hyperspectral image aquisition with digital CCD video camera, Proc. of the 16th Biennial Workshop on Videography and Color Photography in Resource Assessment, Weslaco, Texas, April 29–May 1, 1997. Pp. 129–140.

Mertz, L. 1962. A stigmatic concave grating spectrograph, J. Opt. Soc. Am, Vol. 52, No. 10, October.

Mertz, L. 1977. Concentric spectrographs, Appl. Opt., Vol. 16, No. 12, pp. 3122–3124.

Mouroulis, P. and Thomas, D.A. 1998. Compact, low-distortion imaging spectrometer for remote sensing, Proc SPIE, Vol. 3438; pp. 31–37.

Mouroulis, P. 1998. Low-distortion Imaging Spectrometer Utilizing Convex Gratings, Proc SPIE, Vol. 3482; pp. 594–601.

Mouroulis, P. 1999. Spectral and spatial uniformity in pushbroom imaging spectrometers, Proc SPIE, Vol. 3753; pp. 133–141.

Mäkisara, K. and Tomppo, E. 1996. Airborne imaging spectrometry in national forest inventory, IEEE 1996 International Geoscience and Remote Sensing Symposium, Vol. II.

Mäkisara, K., Lohi, A. and Karna, J.P. 1994. A system for geometric and radiometric correction of airborne imaging spectrometer data, Geoscience and Remote Sensing Symposium, 1994. IGARSS '94. Surface and Atmospheric Remote Sensing: Technologies, Data Analysis and Interpretation., International Vol, 3, pp. 1503–1505.

Mäkisara, K., Meinander, M., Rantasuo, M., Okkonen, J., **Aikio, M.**, Sipola K., Pylkkö, P. and Braam, B. 1993. Airborne Imaging Spectrometer for Applications (AISA), in International Geoscience and Remote Sensing Symposium Digest. Pp. 479–481.

NASA, EOS AURA Project's Home Page, 2001. http://eos-aura.gsfc.nasa.gov/

NASA, Website of the Ozone Monitoring Instrument (OMI) of EOS AURA Project. 2001b. http://aura.gsfc.nasa.gov/omi/

Otten, L.J. III, Butler, E.W., Rafert, J.B. and Sellar, R.G. 1995. The design of an airborne Fourier transform visible hyperspectral imaging system for light aircraft environmental remote sensing, Proc SPIE, Vol. 2480, pp. 418–424.

Sandor-Leahy, S., Beiso, D., Figueroa, M., Folkman, M., Gleichauf, D., Hedman, T., Jarecke, P. and Thordarson, S. 1998. The TRWIS III hyperspectral imager: instrument performance and remote sensing applications, Proc. SPIE, Vol. 3438, pp. 13–21.

Schau, H.C., Descour, M.R., Dereniak, E.L., Spuhler, P.T. and Volin, C.E. 2000. System and Design Requirements in Computed Tomographic Imaging Spectroscopy, Proc SPIE, Vol. 4132, pp. 25–31.

Schlemmer, H.H. and Mächler, M. 1985. Diode array spectrometer: an optimised design, J. Phys. E.: Sci. Instrum., Vol. 18, pp. 914–919.

Schott Glaswerke. 1984. Optical Glass Filters, product catalogue.

Smith, W.J. 1992. Modern lens design: a resource manual, McGraw-Hill Inc.

Specim Ltd. 2001a. AISA Airborne Imaging Spectrometer, product brochure from Specim Ltd website: http://www.specim.fi/

Specim Ltd. 2001b. ImSpector Imaging Spectrometer, product brochure from Specim Ltd website: http://www.specim.fi/

Vaarala, T., Moring, I. and Herrala, E. 1995. Imaging spectroscopy for on-line wood quality inspections: an experimental study, Proceedings from the 2nd International Seminar/Workshop on Scanning Technology and Image Processing on Wood, Skellefteå, Sweden, 14–16 August 1995.

Vaarala, T., **Aikio, M**. and Keränen, H. 1997. An advanced prism-grating-prism imaging spectrograph in on-line industrial measurement, Proc SPIE, Vol. 3101, pp. 322–330.

Villemaire, A., Fortin, S., Lafond, C., Soucy, M.A., Legault, J.F., Giroux, J., Goodrich, S.M., Bauldree, R.S. and Rapp, R.J. 1998. High-resolution airborne imaging spectrometer, Proc SPIE, Vol. 3436, pp. 924–930.

Willoughby, C.T, Folkman, M.A. and Figueroa, M.A. 1996. Application of hyperspectral imaging spectrometer systems to industrial inspection, Proc SPIE, Vol. 2599; pp. 264–272.

Wilson, T. and Davis, C. 1999. Naval EarthMap Observer (NEMO) Satellite, Proc SPIE, Vol. 3753, pp. 2–11.

Wolfe, W.L. 1997. Introduction to Imaging Spectrometers, SPIE Optical Engineering Press.

Volin, C.E., Ford, B.K., Descour, M.R., Garcia, J.P., Wilson, D.W., Maker, P.D. and Bearman, G.H. 1998. High speed spectral imager for imaging transient fluorescence phenomena, *Applied Optics*, Vol. 37, No. 34, pp. 8112–8119.

Volin, C.E., Garcia, J.P., Dereniak, E.L. and Descour, M.R. 1999. MWIR Computed Tomography Imaging Spectrometer: Calibration and Imaging Experiments, Proc SPIE, Vol. 3753, pp. 192–-202.

Zemax Optical Design Program of Focus Software Inc. 2000. Users Guide for Version 9.0.

Åstrand, E. 1996. Automatic Inspection of Sawn Wood, *Doctoral Thesis*, Lindköping University, Sweden.

Appendix A

Line number of a grating as a function of a focal length of focusing optics in a grating spectrograph

The following derivation has been done by Janne Aikio, Research Scientist at VTT Electronics.

When designing a PGP spectrograph (see Fig 1) the wavelength range from λ_1 to λ_2 are given in the specifications. Then the detector is selected. Next a suitable pair of a focal length of the focusing optics and the line number of a grating should be chosen.

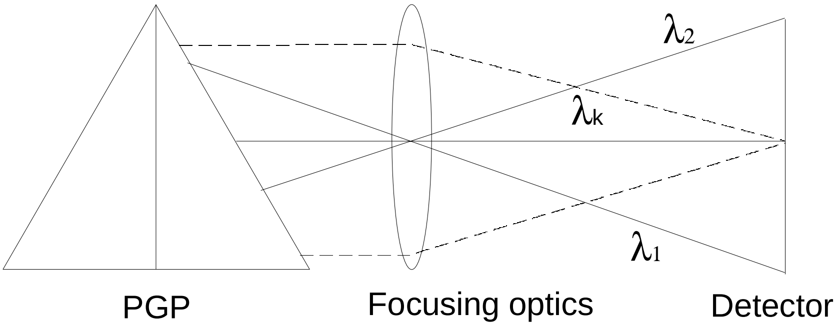

Fig 1. A part of a PGP spectrograph optics: a dispersing PGP component, a focusing optics and a detector. $\lambda_1 < \lambda_k < \lambda_2$.

A rough approximation of the line number of the grating as a function of the focal length can be calculated based on a simplified model consisting of a grating instead of a PGP, a focusing optics and a detector (see Fig 2). The central wavelength of the spectrum is denoted as λ_K. The grating equation is

(1) $$\sin\theta_2 = -\frac{k\lambda}{dn} - \sin\theta_1$$

.

When the angle of incidence into the grating is set as $\theta_1 = 0°$, θ_2 is denoted as θ and the diffraction order k = -1 is used, we get

$$(2)\ \theta(\lambda) = \arcsin\left(\frac{\lambda}{n_1 d}\right).$$

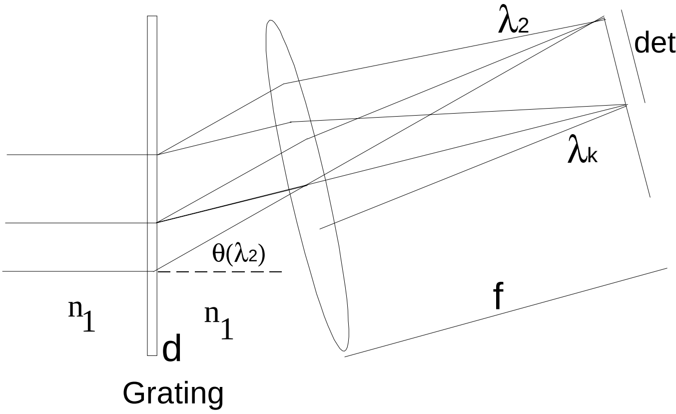

Fig 2. A simplified model consists of a grating with period of ***d****, a focusing optics and a detector, which length is denoted as* ***det****. The refractive index of medium is* n_1.

From Fig 2 we can see, that

$$(3)\ \begin{aligned} \frac{\det}{2} &= f\tan[\theta(\lambda_2) - \theta(\lambda_k)] = f\tan\left[\arcsin\left(\frac{\lambda_2}{n_1 d}\right) - \arcsin\left(\frac{\lambda_k}{n_1 d}\right)\right] \\ &\Rightarrow \arctan\left[\frac{\det}{2f}\right] = \arcsin\left(\frac{\lambda_2}{n_1 d}\right) - \arcsin\left(\frac{\lambda_k}{n_1 d}\right) \end{aligned}$$

Function *arcsin* can be expressed as follows.

$$e^{i\theta} = \cos\theta + i\sin\theta = \sqrt{1-\sin^2\theta} + i\sin\theta, \ (\cos\theta > 0)$$
$$\Rightarrow \theta = -i\ln\left(\sqrt{1-\sin^2\theta} + i\sin\theta\right) = \arcsin(\sin\theta).$$

When we denote $\sin\theta = \sin(x)$, *we get*

$$(4) \quad \theta = \arcsin(x) = -i\ln\left(\sqrt{1-x^2} + ix\right).$$

Similarly, we get for function *arctan* the following expression

$$(5) \quad \arctan(x) = -\frac{1}{2}i\ln\left(\frac{1+xi}{1-xi}\right) = -i\ln\left(\frac{1+xi}{\sqrt{1+x^2}}\right).$$

When (4) and (5) are inserted in equation (3), we get

$$\Rightarrow -i\ln\left[\frac{1+\left(\frac{\det}{2f}\right)i}{\sqrt{1+\left(\frac{\det}{2f}\right)^2}}\right] = -i\ln\left[\frac{i\frac{\lambda_2}{n_1 d} + \sqrt{1-\left(\frac{\lambda_2}{n_1 d}\right)^2}}{i\frac{\lambda_k}{n_1 d} + \sqrt{1-\left(\frac{\lambda_k}{n_1 d}\right)^2}}\right]$$

$$\Rightarrow ai+b=\frac{\left(\frac{\mathrm{det}}{2f}\right)i}{\sqrt{1+\left(\frac{\mathrm{det}}{2f}\right)^2}}+\frac{1}{\sqrt{1+\left(\frac{\mathrm{det}}{2f}\right)^2}}=\frac{\frac{\lambda_2}{n_1 d}i+\sqrt{1-\left(\frac{\lambda_2}{n_1 d}\right)^2}}{\frac{\lambda_k}{n_1 d}i+\sqrt{1-\left(\frac{\lambda_k}{n_1 d}\right)^2}}$$

$$\Rightarrow (ai+b)\left(\frac{\lambda_k}{n_1 d}i+\sqrt{1-\left(\frac{\lambda_k}{n_1 d}\right)^2}\right)=\left(-a\frac{\lambda_k}{n_1 d}+b\sqrt{1-\left(\frac{\lambda_k}{n_1 d}\right)^2}\right)+\left(b\frac{\lambda_k}{n_1 d}+a\sqrt{1-\left(\frac{\lambda_k}{n_1 d}\right)^2}\right)i$$

$$=\sqrt{1-\left(\frac{\lambda_2}{n_1 d}\right)^2}+\frac{\lambda_2}{n_1 d}i$$

$$\Rightarrow \begin{cases} -a\frac{\lambda_k}{n_1 d}+b\sqrt{1-\left(\frac{\lambda_k}{n_1 d}\right)^2}=\sqrt{1-\left(\frac{\lambda_2}{n_1 d}\right)^2} & \text{(real part)} \\ b\frac{\lambda_k}{n_1 d}+a\sqrt{1-\left(\frac{\lambda_k}{n_1 d}\right)^2}=\frac{\lambda_2}{n_1 d} & \text{(imaginary part)} \end{cases}$$

All square roots are real, when the wavelengths are smaller than the period of the grating in medium, $\lambda < n_1 d$. From the equation of the imaginary part, we get

$$\frac{\lambda_2}{n_1 d}-b\frac{\lambda_k}{n_1 d}=a\sqrt{1-\left(\frac{\lambda_k}{n_1 d}\right)^2}\ .$$

When both sides of the equation are raised to a power of 2, we get

$$\Rightarrow \left(\frac{\lambda_2}{n_1 d}-b\frac{\lambda_k}{n_1 d}\right)^2=\left(\frac{\lambda_2}{n_1 d}\right)^2-2b\frac{\lambda_2\lambda_k}{(n_1 d)^2}+\left(b\frac{\lambda_k}{n_1 d}\right)^2=a^2-a^2\left(\frac{\lambda_k}{n_1 d}\right)^2.$$

Thus the period of the grating can be calculated

$$(6)\ d = \sqrt{\left(\frac{\lambda_2}{n_1 a}\right)^2 - 2b\frac{\lambda_2\lambda_k}{(n_1 a)^2} + \left(b\frac{\lambda_k}{n_1 a}\right)^2 + \left(\frac{\lambda_k}{n_1}\right)^2}\ ,$$

where

$$a = \frac{\det}{2f}\frac{1}{\sqrt{1+\frac{\det}{2f}}} \text{ and } b = \frac{1}{\sqrt{1+\frac{\det}{2f}}}\ .$$

Equation (6) is valid for the wavelengths smaller than the period of the grating.

The line number of a grating is $v = 1/\mathrm{d}$. An assembly coefficient, p, is the ratio between the required length of the spectrum and the length of the detector in the direction of the spectrum. It has typically a value between 0.95 to 1.0. From equation (6) we get equation (7) to calculate the line number of a grating as a function of the focal length of focusing optics.

$$(7)\ v(f) = \frac{1}{\sqrt{\left(\frac{\lambda_2}{n_1 a}\right)^2 - 2b\frac{\lambda_2\lambda_k}{(n_1 a)^2} + \left(b\frac{\lambda_k}{n_1 a}\right)^2 + \left(\frac{\lambda_k}{n_1}\right)^2}}\ ,$$

where

$$a = \frac{p\cdot\det}{2f}\frac{1}{\sqrt{1+\frac{p\cdot\det}{2f}}} \quad \text{and} \quad b = \frac{1}{\sqrt{1+\frac{p\cdot\det}{2f}}}\ .$$

List of symbols

n_1 = refractive index of medium

λ = wavelength

λ_1 = shortest wavelength of the spectrum

λ_2 = the longest wavelength of the spectrum

λ_k = central wavelength

$\theta_1 = \theta_1(\lambda)$ = angle of incidence to the grating

$\theta_2 = \theta_2(\lambda)$ =angle of departure from the grating

d = period of the grating

$\nu = 1/d$ = line number of the grating

f = focal length of focusing optics

det = length of the detector in the direction of the spectrum

p = assembly coefficient, the ratio between the required length of the spectrum and the length of the detector in the direction of the spectrum

Example:

- Wavelength range: $\lambda_1 = 400$ nm
  $\lambda_K = 600$ nm
  $\lambda_2 = 800$ nm
- Length of the detector
  in the spectral direction : 4.83 mm
- Required length of the spectrum: 4.7 mm
- => assembly coefficient: $p = 0.97$
- Focal length range: f = 10 mm – 60 mm

The result is shown in the Fig 3: line number of a grating as a functioin of the focal length of focusing optics.

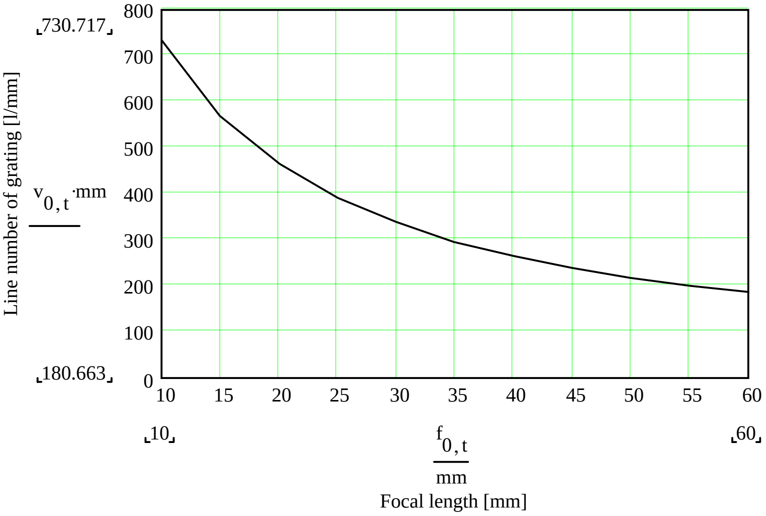

Fig 3. Line number of a grating as a function of the focal length of focusing optics.

Published by

Vuorimiehentie 5, P.O.Box 2000, FIN-02044 VTT, Finland
Phone internat. +358 9 4561
Fax +358 9 456 4374

Series title, number and report code of publication

VTT Publications 435
VTT-PUBS-435

Author(s)
Aikio, Mauri

Title

Hyperspectral prism-grating-prism imaging spectrograph

Abstract

A new type of a direct vision dispersing component, the prism-grating-prism (PGP), was invented by the author in 1991. This patented component allows small, low-cost hyperspectral imaging spectrographs suitable for industrial and research applications in the wavelength range from 320 nm to 2700 nm, limited by the transmission of the grating material.

The PGP spectrograph optics and the design procedure are described. The concept has been applied to many hyperspectral imaging spectrographs. The potential of the PGP construction is shown by introducing four designs in detail. 1) The prototype of a low-cost airborne hyperspectral imaging spectrograph, AISA, was the first application of the PGP concept. 2) A microscope imaging UV-VIS-NIR spectrometer system for spectral measurement of micrometer-sized objects such as wood fibers was developed. 3) A multiple-points PGP spectrograph connected to optical fibre probes was designed for industrial applications such as on-line colour and oil film thickness measurements. 4) The PGP spectrograph design for a high-speed interrogation system for large-scale fibre optic Bragg grating arrays is described.

The PGP concept and the results of the developement work were so promising, that a company was founded in 1995 to commercialize, further develope and manufacture PGP spectrograph technology. Today PGP spectrographs are used world-wide for industrial machine vision and spectral analysis, airborne remote sensing and scientific applications in the form of standard products and customized OEM components.

Keywords
imaging spectroscopy, prism-grating-prism components, PGP, optical design, fiber optics, hyperspectral, airborne

Activity unit
VTT Electronics, Optoelectronics, Kaitoväylä 1, P.O.Box 1100, FIN–90571 OULU, Finland

ISBN
951–38–5850–2 (soft back ed.)
951–38–5851–0 (URL: http://www.inf.vtt.fi/pdf/)

Project number

Date
May 2001

Language
English

Pages
114 p. + app. 7 p.

Price
C

Name of project

Commissioned by
National Technology Agency (Tekes), companies, Emil Aaltonen Foundation, Academy of Finland

Series title and ISSN
VTT Publications
1235–0621 (soft back ed.)
1455–0849 (URL: http://www.inf.vtt.fi/pdf/)

Sold by
VTT Information Service
P.O.Box 2000, FIN-02044 VTT, Finland
Phone internat. +358 9 456 4404
Fax +358 9 456 4374